

## **INFORMATION TO USERS**

**This manuscript has been reproduced from the microfilm master. UMI films the text directly from the original or copy submitted. Thus, some thesis and dissertation copies are in typewriter face, while others may be from any type of computer printer.**

**The quality of this reproduction is dependent upon the quality of the copy submitted. Broken or indistinct print, colored or poor quality illustrations and photographs, print bleedthrough, substandard margins, and improper alignment can adversely affect reproduction.**

**In the unlikely event that the author did not send UMI a complete manuscript and there are missing pages, these will be noted. Also, if unauthorized copyright material had to be removed, a note will indicate the deletion.**

**Oversize materials (e.g., maps, drawings, charts) are reproduced by sectioning the original, beginning at the upper left-hand corner and continuing from left to right in equal sections with small overlaps. Each original is also photographed in one exposure and is included in reduced form at the back of the book.**

**Photographs included in the original manuscript have been reproduced xerographically in this copy. Higher quality 6" x 9" black and white photographic prints are available for any photographs or illustrations appearing in this copy for an additional charge. Contact UMI directly to order.**

# **UMI**

**A Bell & Howell Information Company  
300 North Zeeb Road, Ann Arbor MI 48106-1346 USA  
313/761-4700 800/521-0600**



**UNIVERSITY OF CALIFORNIA**

**Santa Barbara**

**Design and Performance of  
Semiconductor Microstrip Lasers**

by

**Daniel A. Tauber**

**March 1998**

**A dissertation submitted in partial satisfaction  
of the requirements for the degree of**

**Doctor of Philosophy**

in

**Electrical and Computer Engineering**

**Committee in charge**

**Professor John E. Bowers, Chairperson**

**Professor Larry A. Coldren**

**Professor Evelyn Hu**

**Professor Robert A. York**

**UMI Number: 9924146**

**Copyright 1998 by  
Tauber, Daniel A.**

**All rights reserved.**

---

**UMI Microform 9924146  
Copyright 1999, by UMI Company. All rights reserved.**

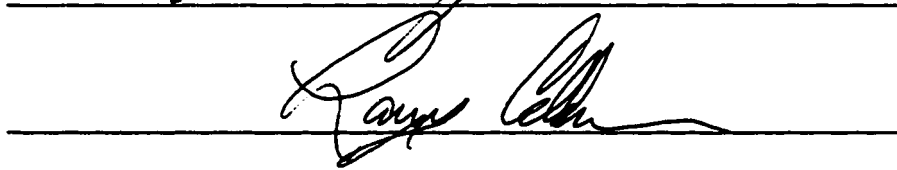
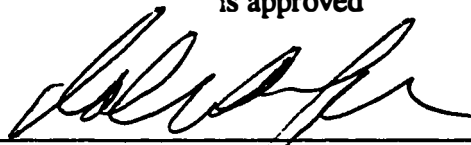
**This microform edition is protected against unauthorized  
copying under Title 17, United States Code.**

---

**UMI**  
**300 North Zeeb Road**  
**Ann Arbor, MI 48103**

The dissertation of Daniel A. Tauber

is approved



Committee Chairperson

March 1998

**March 1, 1998**

**Design and Performance of Semiconductor Microstrip Lasers**

**Copyright © 1998**

**by Daniel A. Tauber**

## VITA

- September 5, 1968      Born, Stamford, Connecticut, USA
- May 1990                S.B. Physics, Massachusetts Institute of Technology
- October 1990-August 1991    Lady Davis Fellow, Technion, Israel Institute of Technology, Haifa, Israel
- September 1991 -March 1998   Graduate Student Researcher, University of California, Santa Barbara
- June 1993                M. S. Electrical and Computer Engineering, University of California, Santa Barbara
- March 1998-                Staff Scientist, Raychem Corporation, Menlo Park, California

## Publications

1. "Development of a Tabletop XUV Laser at 194 Angstroms in Ni-like Mo", S. Basu, M. Muendel, J. P. Braud, S. Kaushik, D. Tauber and P. L. Hagelstein, paper QTUD2, Technical Digest of the International Quantum Electronics Conference, p. 54, Anaheim, CA, May 1990.
2. "Status Report on the MIT Short Wavelength Laser Project", P. L. Hagelstein, S. Basu, M.H. Muendel, J.P. Braud, D. Tauber, S. Kaushik, J. Goodberlet, T. - Y. Hung, and S. Maxon, Inst. Phys. Conf. Ser. No. 116. Int. Colloquium on X-Ray Lasers, York, England, September 1990.
3. "Alignment System for Solid Surface EUV Laser Targets", Daniel Tauber, Santanu Basu, and Peter L. Hagelstein, Appl. Opt. 30, 4337 (1991).
4. "A Low Noise Figure 1.5  $\mu\text{m}$  Multiple - Quantum Well Optical Amplifier", D. Tauber, R. Nagar, A. Livne, and G. Eisenstein, IEEE Photon. Technol. Lett., 4, 238 (1992).
5. "Low Noise Figure 1.5  $\mu\text{m}$  MQW Optical Amplifier", D. Tauber, R. Nagar, A. Livne, and G. Eisenstein, paper TuM2, Technical Digest of the Optical Fiber Communications Conference, p. 71, San Jose, CA, February, 1992.

6. "70 GHz Relaxation Oscillation in a Vertical Cavity Surface Emitting Laser", D. Tauber, G. Wang, R. S. Geels, J. E. Bowers, and L. A. Coldren, paper IIB-4, Proceedings of the Device Research Conference, Cambridge, MA, June 1992.
7. "Large and Small Signal Dynamics of Vertical Cavity Surface Emitting Lasers", D. Tauber, G. Wang, R. S. Geels, J. E. Bowers, and L. A. Coldren, *Appl. Phys. Lett.* **62**, 325 (1993).
8. "Vertical Cavity Laser High Speed Dynamics and Modeling", John E. Bowers, Dubravko I. Babić, Gary Wang, Daniel Tauber, Wenbin Jiang, and Radhakrishnan Nagarajan, paper IWB1, Integrated Photonic Research Conference (Invited), Palm Springs, CA, March, 1993.
9. "Reduction of Damping in High Speed Semiconductor Lasers", Gary Wang, Radhakrishnan Nagarajan, Dan Tauber, and John Bowers, *IEEE Photon. Technol. Lett.*, **5**, 642 (1993).
10. "Picosecond Gain Dynamics in Vertical Cavity Surface Emitting Laser: Transient Carrier Heating and Gain Enhancement", Gary Wang, Radhakrishnan Nagarajan, Dan Tauber, and John E. Bowers, *OSA Proceedings on Ultrafast Electronics and Optoelectronics*, Jagdeep Shah and Umesh Mishra, eds. (Optical Society of America, Washington, DC 1993), **14**, pp. 25-28.
11. "Inherent Bandwidth Limits in Semiconductor Lasers due to Distributed Microwave Effects", Daniel A. Tauber, Ralph Spickermann, Radhakrishnan Nagarajan, Thomas Reynolds, Archie L. Holmes, Jr., and John E. Bowers, *Appl. Phys. Lett.*, **64**, 1610 (1994).
12. "Inherent Bandwidth Limits in Semiconductor Lasers due to Distributed Microwave Effects", Daniel A. Tauber, Ralph Spickermann, Radhakrishnan Nagarajan, Thomas Reynolds, Archie L. Holmes, Jr., and John E. Bowers, paper CThB3, Technical Digest of the Conference on Lasers and Electro-Optics, p. 277, Anaheim, CA, May 1994.
13. "Distributed Microwave Effects in High Speed Semiconductor Lasers", D. Tauber, R. Spickermann, R. Nagarajan, T. Reynolds, A. L. Holmes, Jr., and J. E. Bowers, paper TUC1-1, Digest of IEEE MTT-S International Microwave Symposium, p. 47, San Diego, CA, May 1994.
14. "High Speed Optoelectronics", R. Nagarajan, K. Giboney, R. Yu, D. Tauber, and J. E. Bowers, 21st International Symposium on Compound Semiconductors (Invited), San Diego, CA, USA, September 1994. 15. "High Speed Semiconductor Lasers", Radhakrishnan Nagarajan, Daniel Tauber, and John E. Bowers, *International Journal of High Speed Electronics and Systems* (Invited), Fall 1994.

16. "Microwave Propagation Effects in Directly Modulated Semiconductor Lasers," D. Tauber, R. Spickermann, R. Nagarajan, T. E. Reynolds, A. L. Holmes, Jr. and J. E. Bowers, Government Microcircuit and Applications Conference (GOMAC) , San Diego, CA, November 1994.
17. "Direct Modulation of Widely Tunable Sampled Grating DBR Lasers", S. L. Lee, M. E. Heimbuch, D. A. Tauber, and L. A. Coldren, Photonics West (SPIE) Conference Proceedings, San Jose, CA, January 1996.
18. "Metal Fused Microstrip InGaAsP/InP MQW Lasers", M. Horita, D. Tauber, A. L. Holmes, Jr., B. I. Miller, and J. E. Bowers, Proceedings of the Japan Applied Physics Society, Spring Meeting, March 1996.
19. "The Microstrip Laser", D. Tauber, M. Horita, A. L. Holmes, Jr., B. I. Miller, and J. E. Bowers, Proceedings of the Integrated Photonics Research Conference, Boston, MA, April 1996.
20. "Metal Fused Microstrip InGaAsP/InP MQW Lasers", M. Horita, D. A. Tauber, A. L. Holmes, Jr., B. I. Miller, and J. E. Bowers, Technical Report of the Institute of Electronics, Information, and Communication Engineers (IEICE of Japan), ED96-70, OPE96-36, LQE96-38, p. 19, July 1996.
21. "InGaAsP Metal Fused Microstrip Laser", D. Tauber, M. Horita, A. L. Holmes, Jr., B. I. Miller, J. Piprek, and J. E. Bowers, Engineering Foundation High Speed Optoelectronics Conference, Devices and Systems, Snowbird, Utah, August 1996.
22. "Ultrahigh Speed Semiconductor Lasers", D. Tauber and John Bowers, presented at ILS XII, Optical Society of America annual meeting (Invited), Rochester, New York, October, 1996.
23. "Dynamic Responses of Widely Tunable Sampled Grating DBR tunable lasers", S. L. Lee, D. A. Tauber, V. Jayaraman, M. E. Heimbuch, L. A. Coldren, and J. E. Bowers, IEEE Photon. Technol. Lett., 8, 1597, (1996).
24. "Dynamics of Wide Bandwidth Semiconductor Lasers", D. Tauber and J. E. Bowers, International Journal of High Speed Electronics and Systems (Invited), 8, 377-416, (1997).
25. "The Microstrip Laser", D. Tauber, M. Horita, J. Piprek, P. Abraham, A. L. Holmes, Jr., and J. E. Bowers, IEEE Photon. Technol. Lett., 10, to be published, (April 1998).

## **ABSTRACT**

### **Design and Performance of Semiconductor Microstrip Lasers**

by Daniel A. Tauber

A novel semiconductor laser, the microstrip laser, in which the laser epi film sits on a thick gold ground plane rather than on a conventional semiconductor substrate was invented and demonstrated. The microstrip laser possesses advantages for high frequency and high power operation, because the microwave propagation properties of the microstrip laser are better than the conventional laser, and the thermal resistance is lower.

Microstrip lasers were fabricated in the InP/InGaAsP system by a gold bonding and substrate removal technique. The lasers emit light at 1.55  $\mu\text{m}$  wavelength. Narrow ridge microstrip lasers showed threshold and efficiency performance comparable to conventional lasers. Because of the fabrication technique which inverts the grown epi, the lasers were all n-ridge lasers, with ridges etched through the active region to prevent lateral leakage current and high thresholds.

Microstrip lasers appear to be more susceptible to the opening of parasitic leakage current paths than are conventional lasers. This limited the ultimate performance of the low threshold microstrip lasers discussed above.

Experimental results on devices in which the SCH and active region had not been etched away show that the thermal resistance of the microstrip laser can be more than 3 times smaller than a conventional laser at room temperature. However, because these devices had high thresholds and low efficiencies they did not demonstrate high power operation despite the excellent thermal resistance.

The microwave propagation properties of the microstrip laser are also much improved relative to a conventional laser on a doped substrate, with the microwave loss being a factor of two smaller, and the phase velocity being more than twice as high. These improved propagation properties ensure more uniform microwave current injection to the laser, and better optical response at high frequency.

The microwave propagation properties are important, because as is shown in this dissertation, at high frequency significant phase delays are present along the electrode length. Because of this, the laser behaves as a distributed electrical element rather than a lumped element as has been traditionally assumed, and the nature of high frequency current injection is modified. In conventional lasers on doped substrates, high frequency current is highly localized within the vicinity of the feed point, and the effect worsens as the frequency increases. This causes current rolloff that limits the bandwidth to about 30 GHz in doped substrate lasers. In the microstrip laser, the bandwidth limits do not become manifest until frequencies greater than 50 GHz are reached.

## **Contents**

<b>1</b>	<b>INTRODUCTION .....</b>	<b>1</b>
	1.1 High performance semiconductor lasers	1
	1.2 Organization of this thesis	3
	1.3 High power diode lasers	11
	1.4 High speed diode lasers	15
	1.5 Wafer bonded in plane lasers	29
	1.6 Overview	32
	References	34
<b>2</b>	<b>MICROWAVE PROPAGATION EFFECTS IN SEMICONDUCTOR LASERS .....</b>	<b>41</b>
	2.1 Background	41
	2.2 Transmission line model of a semiconductor laser	45
	2.3 Longitudinal current flow and series impedance	50
	2.4 Shunt capacitance and shunt conductance	56
	2.5 Calculation of propagation properties from distributed circuit model	58
	2.6 Comparison of microstrip laser and coplanar electrode laser	65
	2.7 Effect of microwave propagation on dynamics and modulation response	68
	2.8 Other dynamic effects related to microwave propagation	77
	2.9 Optical-microwave velocity mismatch effects	77
	2.10 Summary and conclusions	78

	<b>References</b>	<b>80</b>
<b>3</b>	<b>DC ANALYSIS OF THE MICROSTRIP LASER: CURRENT DISTRIBUTION AND HEAT DISTRIBUTION .....</b>	<b>83</b>
	3.1 Background	84
	3.2 Lateral current spreading	88
	3.3 Effect of current spreading on threshold	90
	3.4 Effect of current spreading on efficiency	92
	3.5 Experimental verification of currents spreading	94
	3.6 Etched active regions	96
	3.7 Electrical resistance	102
	3.8 Heat conduction and thermal resistance	105
	3.9 Summary and conclusions	108
	References	109
<b>4</b>	<b>MICROSTRIP LASER FABRICATION .....</b>	<b>113</b>
	4.1 Materials growth	113
	4.2 Surface preparation, metal evaporation, and bonding	114
	4.3 Optimization of bonding conditions. Summary of bonding techniques.	121
	4.4 Substrate removal	127
	4.5 Fabrication of ridge waveguide lasers	127
	4.6 Broad area laser fabrication	131
	4.7 Microstrip broad area laser	132

4.8	10 $\mu\text{m}$ ridge laser fabrication	136
<b>4</b>	<b>MICROSTRIP LASER FABRICATION (continued)</b>	
4.9	Narrow ridge fabrication	139
4.10	Polyimide planarization	144
4.11	Ridge metallization	149
4.12	Etch to metal layer	150
4.13	Final metallization	151
	References	153
<b>5</b>	<b>DEVICE RESULTS .....</b>	<b>155</b>
5.1	Broad area laser results	155
5.2	10 $\mu\text{m}$ ridge lasers	164
5.3	Narrow ridge devices	167
5.4	Thermal resistance	186
5.5	Microwave performance	190
5.6	Summary and conclusions	195
	References	197
<b>6</b>	<b>SUMMARY AND FUTURE PROSPECTS .....</b>	<b>199</b>
	References	203

# **Chapter 1**

## **Introduction**

### **1.1 High performance semiconductor lasers**

High performance in a semiconductor laser can be characterized in multiple ways. The characterization is application dependent, and high performance means different things for different systems. One system might specify extremely low power dissipation, while concurrently requiring only minimal optical output power. An example of this is short distant optical interconnects [1], with the laser performance criteria being low threshold current and low electrical resistance. A different application could require high optical output power, with looser restrictions on the power dissipation. A third application could require high speed and high power performance. These last two criteria are the performance issues addressed in this dissertation.

Applications for high power and high speed semiconductor lasers are diverse and abundant. A partial list includes instrumentation for laser surgery, printing and imaging, data storage, and communications. The applications for high power in communications are large, and will continue to grow as the number of fiber optic transmission systems grows. High power semiconductor lasers are absolutely essential to long distance links as pump lasers for erbium doped fiber amplifiers (EDFAs). Fiber optic links with periodically spaced EDFAs are the paradigm for long distance transmission, and there has been great commercial and research effort devoted towards developing efficient and compact high power pumps. The EDFA

can be pumped at 1.48  $\mu\text{m}$  using InGaAsP semiconductor lasers, or at 0.98  $\mu\text{m}$ , using InGaAs semiconductor lasers. EDFAs pumped at 0.98  $\mu\text{m}$  are less noisy than their 1.48  $\mu\text{m}$  counterparts [2] and are technologically more because of this: with lower noise, equivalent system performance is possible with larger EDFA spacing. Larger spacing means fewer EDFAs per system, which means lower cost.

The need for semiconductor lasers in communications systems extends well beyond pump lasers for EDFAs. Semiconductor lasers are also transmission sources. A wide range of performance criteria are needed to characterize a good source, and high speed and high power are among them. Other criteria include linewidth, wavelength drift, lifetime, and temperature stability.

High power is potentially as important for sources as it is for pumps, as a good high power laser is capable of driving several systems at once, or can compensate for coupling losses that might be inherent in discrete component transmission systems - for example, a system that uses an external modulator. A wavelength division multiplexed (WDM) system might require partitioning a single source into multiple wavelength channels, and a high power laser helps keep each channel at an acceptable power level. High speed is equally important: direct modulation of a laser by modulating the injection current remains the simplest and most straightforward technique for the generation of AC optical signals. Analog and digital modulation are both viable techniques, and are both in [3, 4]. While wavelength chirping and fiber dispersion limit the maximum transmission distance of directly modulated lasers, direct modulation is still often the best choice for short or medium distance links [4]. The fundamentals of laser and amplifier dynamics are also well studied by investigating direct modulation, as has been clearly

demonstrated in recent years [5-7]. The understanding of the fundamentals derived from understanding direct modulation can be critically important in designing any number of other optical-microwave sources.

## **1.2 Organization of this thesis**

The topics investigated in this dissertation are unified in a novel laser structure, the microstrip laser, that we have invented, fabricated and demonstrated during the course of this work, and that shows great promise for both high frequency and high power operation. A schematic of the microstrip laser is shown in Figure 1. The laser differs from a conventional ridge waveguide structure only in that the epitaxial layers sit above a 1  $\mu\text{m}$  thick gold ground plane instead of a semiconductor substrate. The work presented here has been done in the InP system, with InGaAsP active regions emitting light at 1.55  $\mu\text{m}$ . The microstrip laser is not restricted to this material system and can also be fabricated in GaAs/InGaAs, or in any other material system for which semiconductor lasers are currently made. The thick gold ground plane provides advantages for both high speed and high power performance: the microwave transmission line properties of the microstrip laser are vastly superior to the conventional ridge laser on a doped substrate, and the thick gold is a heat spreader that helps reduce the thermal resistance. The fabrication technique, which involves wafer fusion and substrate removal, inverts the epitaxial layer sequence - that is, a p-up wafer is transformed into an n-up wafer after fusion and substrate removal. This provides some distinct advantages for high speed and high power that often cannot be achieved through conventional growth methods.

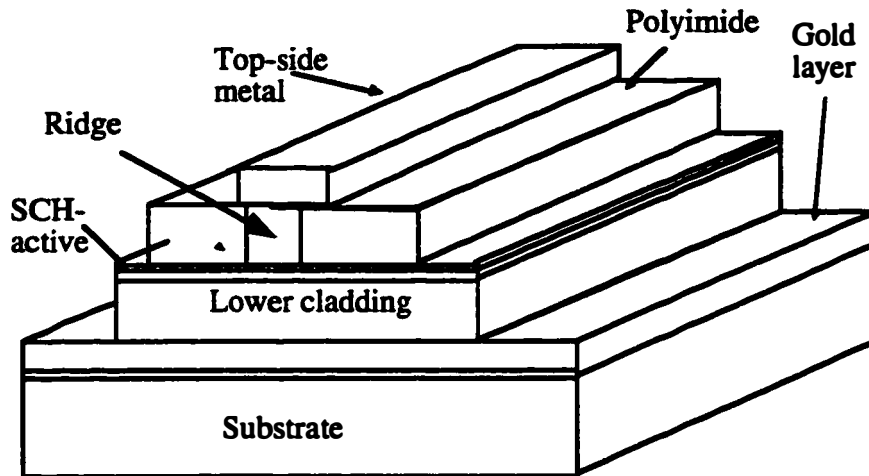


Figure 1. Schematic picture of microstrip laser.

Chapter 2 presents our work on microwave propagation effects in high frequency semiconductor lasers. It was this work which motivated the invention of the microstrip laser. The investigation of microwave propagation showed that microwave signals on a conventional semiconductor laser are subject to significant phase delays and high microwave attenuation. In other words, at high frequency a semiconductor laser is an extremely poor microwave transmission line and it behaves as a distributed electrical element. This analysis had never been done before, and it was always assumed that the diode laser responded to microwave signals as a lumped element with no phase delays between feed point and far end of the device. Chapter 2 shows that distributed effects are present and do significantly impact the dynamic optical response. Fabrication of high speed devices on doped substrates has been known for years to be a fundamentally bad design in the microwave circuit community [8], because of the poor conductivity of doped semiconductor, which is more than two orders of magnitude smaller than metals

such as gold, copper, and aluminum. The propagation of microwaves in doped semiconductor is accompanied by enormous microwave loss that causes rapid attenuation of modulation signals. In the semiconductor laser, this results in the phenomenon that regions far from the feed point are not modulated by the high frequency current. Experiments on lasers fabricated on doped substrates, where the doped substrate acts as a poor ground plane, show that signals can be attenuated as much as 6 dB every 100  $\mu\text{m}$  at 40 GHz. The effect is highly frequency dependent, worsening with increasing frequency, causing the high frequency optical response rolls off because the loss worsens with increasing frequency. The dynamic response is manifested in both the small signal [9-11] and the large signal regime [12, 13].

The microstrip laser minimizes currents flowing in the doped semiconductor, and is therefore an improvement over the conventional laser on a doped substrate. The losses are shown experimentally and theoretically to be lower by a factor of 2. Phase velocities are 2 to 3 times higher as well. The end result is that while -3 dB rolloff frequencies caused by distributed effects in doped substrate lasers occur around 30 GHz, in the microstrip laser they occur beyond 50 GHz (though these frequencies do depend on device length - this calculation is done for a laser 300  $\mu\text{m}$  long). A calculation comparing a high frequency laser fabricated in the two geometries shows the microstrip laser to have a bandwidth of 36 GHz and the conventional laser to have a bandwidth of 31 GHz. The coplanar electrode laser is also discussed, as it solves similar microwave problems by etching down from the top to the n-layer, and placing coplanar ground electrodes close to the signal line. The microstrip laser is shown to be the best of all the different designs, with the

conventional doped substrate the worst. All these microwave issues are discussed in depth in Chapter 2.

Chapter 3 moves from the high frequency domain to the DC domain, investigating subjects such as lateral current spreading and its effect on threshold and efficiency, electrical resistance, and thermal resistance. These issues are critical to microstrip laser performance, and are affected by its unique design.

The microstrip lasers studied in this thesis are all n-ridge lasers. The n-ridge design has some advantages and some problems - the same physics that allows for low electrical resistance contributes to problems with lateral current spreading in the laser. This causes high leakage currents, and unacceptably high thresholds and low efficiencies that negate the otherwise positive effects of the low thermal resistance. Chapter 3 studies this problem in depth and shows that the lateral spreading of the electron current in the SCH, rather than the ridge width, is the determining factor in threshold current. Since the diffusion length of electrons in InGaAsP is about 10  $\mu\text{m}$ , any ridge narrower than that suffers from an excessive threshold increase. Calculations show that for a 2  $\mu\text{m}$  ridge, the threshold can increase by a factor of 5. Efficiencies are also degraded, but not to the same extent as the thresholds. Degradations of about 30% are calculated. The efficiency degradation is smaller because above threshold, carrier clamping and a fast stimulated recombination lifetime that helps to reduce the lateral current spreading.

Etching through the SCH and active region solves this problem. The lateral spreading is eliminated, low thresholds and high efficiencies are calculated, and the dependence of threshold on ridge width is reestablished. In the InP system in particular, the low surface recombination velocity means that surface passivation of

the sidewalls is not that critical and there is negligible increase in threshold caused by sidewall recombination. In contrast, in the GaAs system, there is some non-negligible effect in the n-ridge lasers, with the thresholds about doubling for a 2  $\mu\text{m}$  ridge. Etching through the active region is still preferred, and necessary, however, unless an alternate method, such as ion implantation is used for current confinement.

Electrical resistance is also calculated for the different device structures. It is shown that the n-ridge microstrip laser has the lowest electrical resistance of all lasers studied. In general, the n-ridge lasers outperform the p-ridge lasers in all cases. Because the majority of resistance always occurs in the p-regions of the device, the n-ridge microstrip laser is the best, because the hole current flow occurs in the wide bottom p-cladding, that is also only about 1  $\mu\text{m}$  thick. In a normal n-ridge laser on a p-substrate, significant resistance occurs due to the current flow through the thick substrate. This is not the case in the microstrip laser, and the resistance of a 2  $\mu\text{m}$  wide microstrip ridge laser is more than 2 times smaller than the conventional p-ridge laser.

Thermal resistance is the final section of Chapter 3. Shortly after designing the microstrip laser with microwave performance in mind, we realized that the structure possessed significant thermal advantages as well. The 1  $\mu\text{m}$  thick gold layer located just several micrometers from the active region would help heat dissipation, as the thermal conductivity of gold is higher than that of InP by a factor of 5. Further, as mentioned earlier, the fabrication technique inverts the epi layers, turning a wafer grown p-up into an n-up microstrip wafer. Since n-up growth in the InP system is fraught with difficulties due to problems of zinc (Zn) diffusion [14], the microstrip laser introduced some new device properties and possibilities. N-

ridge lasers could be fabricated with very low electrical resistance, and with much reduced joule heating of the active region. This means a low thermal resistance, and a high power capability. Calculations show that the thermal resistance of the n-ridge laser is reduced by a factor of 3 compared to the p-ridge laser, and that the 1  $\mu\text{m}$  thick gold layer can introduce a reduction of about 10% in the thermal resistance, depending on the proximity of the gold to the copper heat sink.

Chapter 4 explains in detail the microstrip laser fabrication process. The gold bonding process and the ridge laser fabrication process are both discussed. It is shown that with effective surface preparation and metal evaporation, excellent, uniform gold bonding can be achieved across a 1  $\text{cm}^2$  wafer at the moderate temperature of 300  $^{\circ}\text{C}$ . A metal sequence consisting of chrome, platinum and gold is found to be most effective. The remainder of the fabrication involves conventional microprocessing techniques for making ridge waveguide lasers. Wet etching of InP ridges is shown to be preferable to dry etching, and a saturated bromine water etch is shown to work well for etching through the InGaAsP active region. A multilayer polyimide planarization process is discussed and shown to have high uniformity (>90%) for ridges 5  $\mu\text{m}$  wide and less.

Chapter 5 presents the microstrip laser results. Threshold performance of the microstrip lasers for wide ridges is shown to be almost as good as that of conventional lasers. An increase of about 20% is observed for 10  $\mu\text{m}$  ridges, which indicates that decent threshold behavior is obtainable in the microstrip design. Spectral measurements show no wavelength shift due to bonding, suggesting that

any thermally induced strain brought about by the bonding process is absorbed in the malleable gold layer.

Narrow ridges show good threshold behavior when the ridge is etched through the SCH and active region. Thresholds below 30 mA are routinely obtained for ridge widths less than 3  $\mu\text{m}$  and for cavity lengths below 300  $\mu\text{m}$ . Compared to the broad area lasers, the thresholds increase by less than a factor of 2 in some cases. Efficiencies comparable to conventional laser efficiencies are also achieved. The thresholds of lasers in which the SCH is not etched away are very high, indicative of the current spreading problem discussed in Chapter 3. The good threshold lasers however, suffer from high resistance and are not practical for cw operation. The high resistance may be related to a doping or oxide problem in those particular lasers and is not intrinsic to the microstrip laser design, as some of the lasers with higher thresholds (unetched SCH) show excellent resistance, on the order of 1 ohm, and the etched active regions cannot account for the large increase in the devices with good thresholds. Further annealing of the lasers reduced the resistance, but also increased the threshold. The threshold increase may be accounted for by an opening of leakage paths in the device; the microstrip laser may be more susceptible to this than is a conventional laser.

Thermal resistancance measurements show a factor of 3 improvement in the microstrip laser at room temperature. From the thermal resistance data for different temperatures and temperature dependent threshold data, an output power for the microstrip laser more than xx times greater was predicted.

The microwave propagation properties were also superior, with phase velocities 2-3 times greater than the conventional laser and microwave attenuation

about a factor of 2 smaller. Incorporating the microwave propagation models presented in Chapter 2 to predict bandwidth, it was shown that the rolloff frequency of the microstrip laser was beyond 50 GHz. A high frequency laser with a 37 GHz intrinsic bandwidth [15] is predicted to be limited to 31 GHz if fabricated in the conventional doped substrate mode and 36 GHz in the microstrip design.

The work presented in this dissertation indicate significant advantages for the microstrip laser compared to a conventional laser for both high power and high frequency operation. Further, the work in this dissertation identifies a new perspective from which a high frequency laser must be studied, that of a distributed electrical element, and shows how different laser structures (conventional on doped substrate, coplanar electrodes, microstrip) can show very different performance due to these effects. The microstrip laser also can be thought of as representing a new flexibility in laser fabrication, beyond that achievable by usual growth and fabrication techniques. This flexibility can be categorized under the heading of wafer bonded lasers, and it shows that significant device improvements in both the thermal and microwave properties are achieved with these new possibilities.

The remainder of the introduction will outline general designs for high power and high speed lasers that have been developed and can be found in the literature. The microstrip laser is a point of reference for the discussion, and its advantages and disadvantages are enunciated with respect to the other structures to illuminate fundamental design principles. A short discussion of in - plane lasers that have been fabricated with wafer bonding techniques is also included.

### 1.3 High power diode lasers

High power performance necessitates high differential efficiency and low thermal resistance. Low threshold currents also help, since the excess heating that causes rollover in the light-current (L-I) curve happens at a higher optical power when the threshold is low. Nonetheless, assuming the threshold current is a small fraction of the total operating current, moderate increases are not as critical as poor efficiency or poor thermal resistance. Other factors contribute also: carrier confinement should be maximized to prevent reduction of the differential efficiency at high current levels or at elevated temperatures [16].

High efficiency is attained by minimizing optical losses in the semiconductor laser waveguide and by reducing leakage currents. In one direction, the waveguide is defined by the epitaxial growth, with the high index active region material surrounded by lower index cladding and separate confinement regions. The structure must be appropriately designed and grown so that there is minimal loss from free carrier absorption in doped regions or poor growth interfaces. In the other direction, the waveguide is defined by material processing, and etched or buried ridges should have smooth sidewalls with low optical scattering. As far as the material is concerned, strained layer quantum well active regions are excellent, because the broken valence band degeneracy brings about low intervalence band absorption and low internal loss. In InP, narrow ridge lasers with strained InGaAs active regions have demonstrated output powers at or above 350 mW at both 1.3  $\mu\text{m}$  and 1.5  $\mu\text{m}$  [17]. At 0.98  $\mu\text{m}$ , similar cw powers for narrow ridges were obtained using InGaAs active regions with InGaAsP barriers [18]. The InGaAsP barriers

are higher than the GaAs barriers most often used at 0.98  $\mu\text{m}$ , and provide much improved carrier confinement, thus improving the differential efficiency at high current levels.

A new innovation reported in high power lasers is the broadened waveguide laser (BWG), in which a very wide SCH region is incorporated in the waveguide to minimize the free carrier loss in the cladding layers. SCH widths up to 1  $\mu\text{m}$  or more are used, and internal losses below 2  $\text{cm}^{-1}$  have been obtained [19]. The threshold also goes up because of a smaller optical confinement factor, but the increase in efficiency more than makes up for that. For 100  $\mu\text{m}$  wide broad area stripes, cw powers of 6.8 watts have been reported for operation at 0.98  $\mu\text{m}$  [19]. The broadened waveguide laser, however, is not a good structure for high speed, because the wide confinement regions introduce unacceptable transport delays that ruin the high speed performance [20].

The thermal resistance relates the temperature increase of the active region to the joule heating by  $\Delta T = R_{th} P_{joule}$ , where  $\Delta T$  is the temperature increase in the active region,  $R_{th}$  is the thermal resistance, and  $P_{joule}$  is the dissipated power that heats the active region [21]. High thermal conductivity materials such as gold and some semiconductors contribute to low thermal resistance, so long as they are near the active region. Structures with high thermal conductivity paths from the active region to the heat sink are desirable; the buried heterostructure laser is a good example since heat efficiently spreads into the wide, highly conducting regions surrounding the active layer. Dielectric buried ridges are not as good because of the inferior thermal conductivity of polyimides, silicon nitride, or silicon oxide. A third contribution to thermal resistance is heat source location. There are essentially two

heat sources in a semiconductor laser, the resistive heating in the ridge, and the heat generated in the active region. The heat generated in the active region is caused by non-radiative recombination and is equal to the non-radiative current contribution times the active region voltage. Most leakage currents are dissipative and also contribute to active layer heating.

The location of the heat sources is critical for thermal resistance [21]. For example, two structures could generate the same amount of joule heat, but because the heat sources are in different places, have drastically different thermal resistances. An example of this is shown in Figure 2. In Figure 2 (a), most of the heat is generated below the active layer and near the heat sink; in 2 (b), it is generated above the active layer, far from the heat sink. The thermal resistance of 2 (b) is much higher because the heat flows through the active layer before arriving at the heat sink, in contrast to the situation in 2 (a), where the heat flows directly from source to sink. Inverting the ridge doping from p to n, and the bottom cladding from n to p, as in a microstrip laser, can result in a lower thermal resistance because the primary heat source is almost always the high resistivity p-layer. Thus the n-ridge microstrip laser resembles Figure 2 (a), the conventional p-ridge laser resembles 2 (b), and the thermal resistance of the n-ridge microstrip is lower. As mentioned earlier, the thick gold layer in proximity to the active region also contributes to a reduced thermal resistance.

Some examples of good high power laser design include a buried heterostructure InGaAs/InGaAsP (buried with an n-InGaP blocking layers) laser operating at  $0.98 \mu\text{m}$  (350 mW) [18], a buried heterostructure InGaAs/InGaAsP

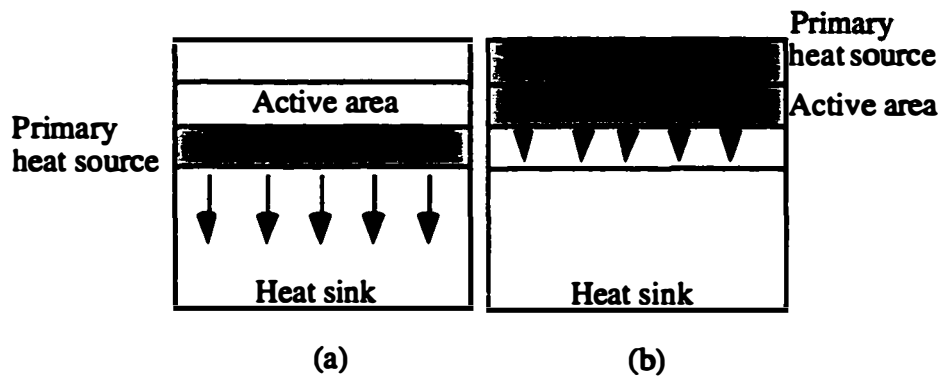


Figure 2. Schematic showing how thermal resistance can depend on the location of the heat source. The thermal resistance in (b) is much higher, although the same joule heat is dissipated as in (a).

(buried with semi-insulating (SI) InP) operating at  $1.5 \mu\text{m}$  (325 mW) [17], an n-ridge v-groove inner stripe (VIPS) laser with a bulk active region and SI InP blocking layers operating at  $1.3 \mu\text{m}$  (230 mW) [22], and a polyimide buried reverse mesa ridge with an InGaAs active layer surrounded by a graded InGaAsP SCH and InGaP cladding layers (350 mW) [23]. Note that all these lasers are mounted p-side down - that is, the high resistance p - layer is placed in proximity to the heat sink so that the heat generated there does not flow through the active region [24]. For all lasers except the n-ridge VIPS, the p-side down mounting involves additional post-processing. The n-ridge microstrip laser shares the same advantage of the n-ridge VIPS laser: no additional post-processing is needed because the best thermal resistance is achieved from a structure mounted junction side up. All the structures have AR/HR coated facets - one facet has a high reflectivity coating above 95%, and the other a low one around 5%. This maximizes the single facet output power while still maintaining good threshold performance.

Catastrophic optical damage (COD) has limited output powers in GaAs/AlGaAs lasers for years. InP/InGaAsP lasers have not suffered from this

because of the low surface recombination velocities in that system. Some advances have been made with respect to COD, including the use of Al-free materials for laser fabrication at 0.98  $\mu\text{m}$  [19] and novel injection techniques - for example, having a non-injection region near the facet [25]. Facet passivation remains an important area of research in short wavelength high power lasers.

The thermal properties of the microstrip laser would further benefit from a burying layer around the active region, as in the VIPS laser. However, with the fabrication technique used for this work, regrowth must be done before fusing because it is done at temperatures for which the bonded gold diffuses throughout the structure, destroying the bond integrity and shorting out the diode. A fabrication technique in which gold bonding was the final step, rather than the initial one, would permit the fabrication of a buried microstrip laser. The differential efficiency of a buried microstrip laser would also improve, as excess optical loss from the etched active region could be minimized.

**1.4 High speed diode lasers**

The bandwidths of high frequency directly modulated semiconductor lasers have surpassed the 40 GHz frequency range in recent years [26]. Several factors have contributed to the progress that led to this achievement. These factors include advances in the understanding of the fundamental carrier dynamics of quantum well lasers, improvements in materials growth and design capabilities, along with the improvements in electrode structure that minimize the harmful effects of microwave propagation, as has been briefly discussed and will be discussed in detail in Chapter 2. The 40 GHz bandwidth has been measured in strained InGaAs/GaAs quantum

well lasers. These lasers emit at a wavelength of  $0.98\ \mu\text{m}$  where the attenuation and dispersion of the fiber significantly limits the maximum transmission distance. The performance of InGaAsP/InP lasers emitting at  $1.55\ \mu\text{m}$ , critical for fiber optic systems, has lagged behind the GaAs lasers, and the highest measured bandwidth to date is 30 GHz [27].

Through the early 1990s, the maximum bandwidths of semiconductor lasers were still limited to below 25 GHz. This was true despite the fact that p-doped strained quantum well lasers had been predicted to have bandwidths as high as 60-90 GHz [28]. An 18 GHz single quantum well laser was reported in the InGaAs system in 1991 [29], and a 23.5 GHz [30] bandwidth in a device with 4 strained quantum wells was reported later that year. In the InGaAsP system, the maximum reported bandwidth was 24 GHz in a device emitting at  $1.3\ \mu\text{m}$  using a bulk active region [31]. By early 1992 Lester and others at Cornell demonstrated a laser with 28 GHz bandwidth [32], improving the previous 23.5 GHz result by implementing a constant index separate confinement heterostructure (SCH) region as opposed to a graded index (GRINSCH) structure that had been used in the earlier result. The current 40 GHz record bandwidth result from the group at the Fraunhofer Institute in Freiburg, Germany is in a device with 4 strained  $\text{In}_{0.35}\text{Ga}_{0.65}\text{As}$  quantum wells [26]. The active region in that structure is undoped; a similar structure with a p-doped active region has a bandwidth of 37 GHz limited by heating [26].

The bandwidths in the InP system have not progressed as much as the GaAs bandwidths, yet this system is technologically more important because of the lower dispersion and loss in optical fibers at  $1.55\ \mu\text{m}$  - critical issues in large bandwidth systems. The record bandwidth for a  $1.55\ \mu\text{m}$  InP strained quantum well laser is 30

GHz [27]. This is a DBR structure, with an active region buried in Fe-doped semi-insulating InP. The DBR allows the gain to be detuned off the peak to the long wavelength side, which increases the resonance frequency, and may circumvent the usual K-factor damping limit [27]. For a Fabry-Perot laser lasing at the gain peak, the record bandwidth has remained 25 GHz for several years in a structure also buried with SI InP, and with a strained, p-doped quantum well active region [33]. This bandwidth is limited by the mounting and device parasitics, and the intrinsic bandwidth is on the order of 40 GHz. Other work has indicated intrinsic bandwidths as high as 68 GHz for undoped strained layer distributed feedback (DFB) lasers, but the bandwidths here were also limited to only 16.5 GHz by the parasitics [34]. A strain compensated, p-doped structure with 16 wells had a bandwidth of 17 GHz [35]. The authors state that this bandwidth is limited by rolloff in the output power caused by leakage currents. Based on the values of resistance and capacitance quoted by them, and the fact that these lasers were mounted p-side down (which tends to increase the mounting capacitance), it is likely that the electrical parasitics limit the device performance also.

While the ultimate limits on bandwidth are set by the active region material properties, many other factors need to be considered in fabricating a structure that will allow those bandwidths to be realized. The non-active region factors can be categorized in 3 groups: (1) laser waveguide properties (2) microwave parasitics - lumped element and distributed effects (3) power consumption and device heating. The specific requirements for high bandwidth lasers are listed in Table 1 below.

<b>Waveguide properties</b>	<b>Microwave structure</b>	<b>Power consumption</b>
<b>Short photon lifetime</b> $\tau_p$	<b>Low capacitance</b>	<b>Low resistive heating</b>
<b>Large photon density in cavity</b>	<b>Low resistance</b>	<b>Low thermal resistance</b>
<b>Single spatial mode waveguide</b>	<b>Low distributed microwave loss</b>	<b>Good heat sinking technology</b>

Table 1. Critical factors, apart from active region properties, for high speed laser performance.

### *Waveguide properties*

The dynamic solution for the small signal modulation of the photon density is a second order transfer function, characterized by a resonance frequency and a damping factor. Maximizing the resonance frequency and minimizing the damping factor leads to high bandwidths. The waveguide design, through its contribution to the resonance frequency, has a large effect on bandwidth. This can be understood by looking at some equivalent expressions for the resonance frequency:

$$\omega_r^2 = 1/\tau_s\tau_p = v_g g_o S_0/\tau_p = v_g g_o \Gamma \eta_i (I - I_{th})/qV \quad (1)$$

$\omega_r$  is the resonance frequency,  $\tau_s$  is the stimulated carrier lifetime,  $\tau_p$  is the photon lifetime,  $v_g$  is the group velocity of the mode,  $g$  is the differential gain,  $S$  is the cavity photon density,  $\Gamma$  is the optical confinement factor,  $\eta_i$  is the internal quantum

efficiency,  $(I - I_{th})$  is the bias current above threshold,  $q$  is the basic electron charge and  $V$  is the active region volume. Intuitively, one necessity for modulation of the optical power is the fast removal of photons from the system (short photon lifetime). Absolute minimization of the photon lifetime, however, is not an independent benchmark for maximum bandwidth, because a short lifetime also reduces the photon density. As shown by the rightmost expression of equation 1, a small threshold current, brought about by a high reflectivity cavity, results in higher resonance frequencies. Mar, et al. [36] examines this issue in detail and concludes that the conditions for high frequency operation are a highly reflective, short cavity, small volume device. If the laser facets do not have a high reflection coating, longer devices may be necessary in order to minimize the thresholds and to maximize differential gain.

High photon density is intimately connected to high power, which requires large current levels and low thermal resistance. The discussion in the high power laser section has covered the design principles for this subject, and will not be discussed here further.

#### *Microwave parasitics*

Another very important issue is the microwave properties of the device from a circuit element perspective. The device parasitics (resistances, capacitances, and inductances) set bandwidth limits and must be minimized. These issues are related to the subject of Chapter 2, and represent the low frequency, lumped element approximation of that problem.

The simplest circuit model of a semiconductor laser is a series resistance in parallel with a capacitance. Figure 3 shows a schematic of a device and points out the sources of resistance and capacitance. In addition to the resistance and capacitance another significant parasitic component is an inductance from the bondwire used for electrically contacting the device, also shown in Figure 3. Short thick bondwires are generally used to minimize the inductance in packaged devices. Device geometries that can be directly probed at high frequencies are not uncommon and eliminate the bondwire inductance completely. Direct probing, however, is not realistic for packaged devices.

Fundamentally, high speed performance requires the minimization of the laser series resistance and capacitance, since the bandwidth will always be limited by the parasitic RC time constant. In general the laser impedance is quite low, on the order of several ohms, and the laser is driven at microwave frequencies by a  $50\ \Omega$  source impedance that acts as a near-ideal current source.

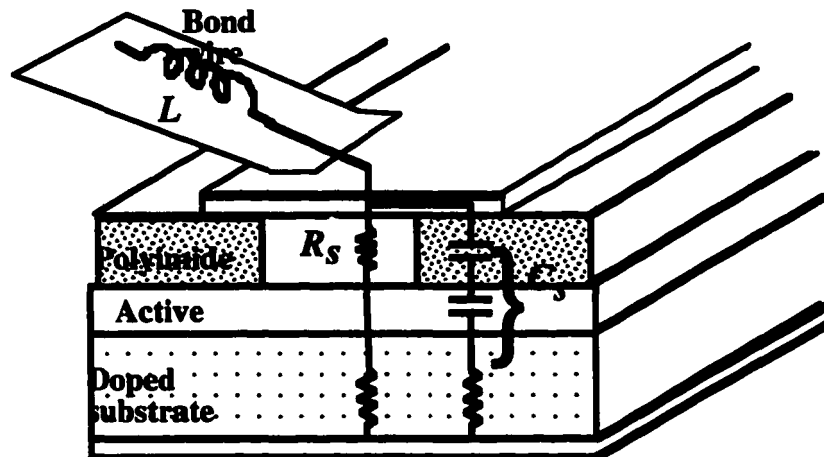


Figure 3. Schematic of a ridge laser structure showing the sources of the parasitic circuit contributions.

Series resistances can be made low by making metal contacts to highly doped semiconductor layers and by grading heterostructures to reduce potential barriers. Typical p-type metallizations are titanium (Ti)/platinum (Pt)/ gold (Au), or some sequence containing Au and zinc (Zn), or perhaps Au/Zn alloy [37]. A metallization sequence using Zn should be alloyed at temperatures in the vicinity of 400 °C in order to drive the Zn dopant into the contact layer.

Buried structures can have lower resistance than ridge structures because wide contact layers can be regrown above the ridge. For example, the structure in references [33] and [38] has a 15  $\mu\text{m}$  wide contact layer regrown over a ridge that is only several  $\mu\text{m}$  wide. The resistance contribution from the contact layer and the heterojunction step are therefore significantly smaller than those in which the contact layer is the same width as the ridge. This structure is shown in Figure 4 (a).

The second issue is low capacitance. The metallization over the dielectric or regrown region is a major source of capacitance. Since high speed lasers typically have ridge widths on the order of microns, a wider metal region is needed for bonding and probing the device. The overlayer metal is usually 10 to 20  $\mu\text{m}$  wide, with a large fraction of that on top of the dielectric or the regrown layer. For ridge structures surrounded by a dielectric, the key to minimizing the capacitance is to have a thick dielectric layer with low dielectric constant. Polyimide is commonly used for this purpose. The dielectric constant of polyimide is about 3 at microwave frequencies which is a small improvement over silicon oxides or silicon nitride, that have dielectric constants of 3.5 and 3.9 respectively.

Regrown structures are found generally only in the InP based system because of the difficulties of regrowth of Al containing compounds, and have the

advantage that a deeply buried ridge can be surrounded by thick semi-insulating layers of Fe-doped InP. Figures 4 (a), (d), and (e) are examples of such a device. In these devices the capacitance is small because of the thick Fe-doped layer. In contrast to ridge lasers where the ridge height fixes the thickness of the surrounding dielectric upon which the metal sits, the thickness of the Fe-doped InP is determined by growth issues, and is often significantly thicker than the dielectric layers in ridge structures. The Fe-doped layers can be as thick as 3-4  $\mu\text{m}$  [39], [40].

The bondpad capacitance is of the same nature as the overlayer metallization capacitance and adds an additional capacitance based on the area of the bondpad. Practical bondpads are about 50-100  $\mu\text{m}$  per side square pads. If the bondpad is fabricated above a semi-insulating substrate with an air-bridge contact to the ridge its capacitive contribution will be very small. In this case, the overlayer metal can be the same width as the ridge, and therefore will be low capacitance.

Figure 4 summarizes some of the best high frequency structures fabricated to date. Figure 4 (a) is the capped mesa buried heterostructure (CMBH) laser that has resulted in a 26 GHz bandwidth in the 1.55  $\mu\text{m}$  InP system. The defining features giving low parasitics are the wide contact pad which results in a low resistance of 2.1  $\Omega$  [33] and the thick Fe-doped InP burying layers which result in low capacitance, as mentioned earlier. In this structure a thin layer of n-InP is grown above the burying layers surrounding the active region, and below the p-InP cladding. The n-InP layer acts as a barrier for Zn diffusion into the Fe-doped layers during growth of the p-cladding; this therefore minimizes leakage current into the Fe-doped regions, and keeps the device thresholds low. However, there is some

lateral microwave current flow associated with the p-n junction at this interface that causes a low frequency dip in the modulation response.

Figure 4 (b) shows the coplanar ridge waveguide structure that has been used in the InGaAs/GaAs system to achieve the record 40 GHz bandwidth [26]. This is a simpler structure because no regrowths are necessary for fabrication. This is not the ideal low resistance structure, since it does not have the wide contact layer that the CMBH structure has and the lateral current flow from the p-contact to the n-contact is constricted to a narrow region, contributing additional resistance. Still, by keeping the doping levels high and the lateral path as short as possible the resistance can be comparable to that of a *pin* structure with vertical current flow. It can be directly probed at high frequency thus eliminating the bondwire inductance, but as mentioned earlier, this is not practical for packaged devices.

A simple structure with excellent high frequency characteristics is the polyimide buried ridge waveguide laser. This structure utilizes a simple ridge surrounded by low dielectric polyimide. This structure compromises some of the low resistance, low capacitance advantages found in the CMBH laser for fabrication simplicity, while still having parasitic bandwidths close to 30 GHz [29], [41]. The ridge structures demonstrated in Figures 4 (b) and (c) are among the best low parasitic structures available for GaAs based lasers. Figures 4 (d) and (e) show several excellent low parasitic structures that have been used in the InP system, for which bandwidths greater than 20 GHz have been demonstrated. The laser in (d) is a constricted mesa laser, with an undercut active surrounded by dielectric or regrown semiconductor. The undercut region allows for excellent current and optical confinement in the active region, whereas the thick polyimide layer provides

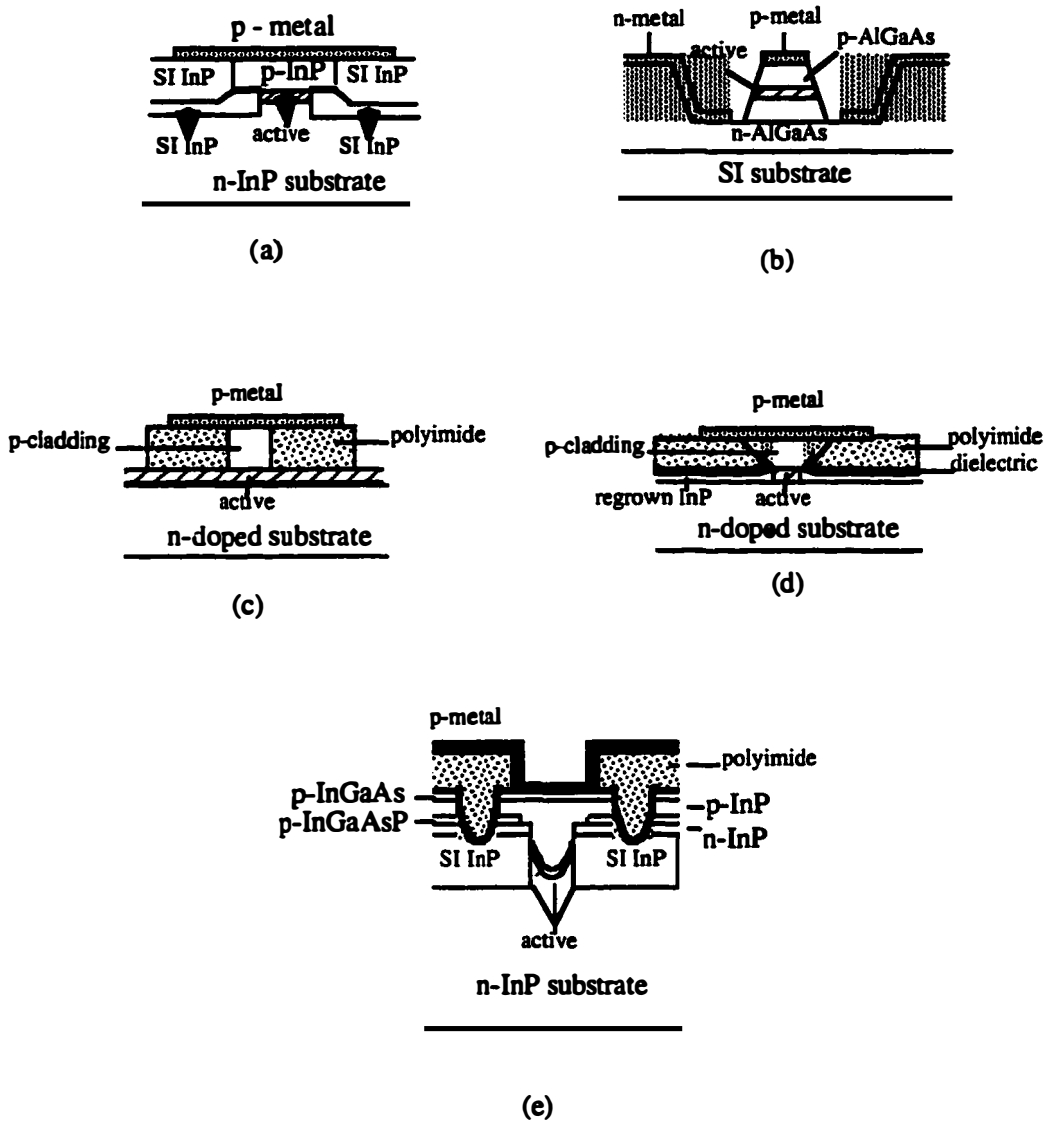


Figure 4. Several different high frequency laser structures. (a) Capped mesa buried heterostructure (CMBH). (b) Coplanar ground-signal-ground electrode laser. (c) Polyimide buried ridge waveguide laser. (d) Constricted mesa laser. (e) Semi-insulating buried crescent (SIBC) laser.

low capacitance, similar to the ridge structure shown in (c). The laser in (e) is the semi-insulating buried crescent (SIBC) laser. A bandwidth of 22 GHz has been reported for a bulk active region SIBC laser operating at 1.3  $\mu\text{m}$  wavelength [39]. A deeply buried crescent active region is grown in a channel that has been etched into previously grown Fe-doped InP. Additionally, a thick layer of polyimide is spun on prior to the final metallization. The combination of the thick polyimide layer and the thick semi-insulating InP layer results in a structure with a low capacitance of about 1 pF. The 22 GHz bandwidth in the structure was, nonetheless limited by the parasitics, and a further reduction in the resistance of the device (as compared to the value quoted in the paper) seems possible. This should permit higher bandwidth operation. The primary disadvantage of this structure is the nonplanar active region which does not allow for the fabrication of DFB structures.

All the structures discussed up to this point are p-ridge devices. As is the case for high power, n-ridge structures also have advantages for high speed, because n-ridges tend to have a lower electrical resistance. The contribution from the p-contact is greatly reduced because it is now a broad area bottom contact. If the laser is grown on a p-substrate, there can be significant resistance from the substrate, but still, as Chapter 3 will demonstrate, the resistance more often than not is lower than a comparable p-ridge structure. A p - substrate mass-transported diode laser with a buried constricted mesa [42] has shown low resistance and low capacitance and exhibited a bandwidth greater than 16 GHz. For the microstrip laser, the p-cladding is only 1 or 2  $\mu\text{m}$  thick, so the resistance is even lower, providing further advantages for high speed operation.

*Quantum well laser dynamics*

Quantum well lasers were predicted to have much improved high frequency properties compared to bulk lasers because the differential gain is higher in a 2-D quantum well laser than in a 3-D bulk device. An excellent conceptual and graphical explanation for the increased differential gain in quantum wells can be found in Coldren and Corzine [43]. While initial studies of quantum well lasers bore out the prediction of high differential gain and high resonance frequency [44], several years passed before a high frequency quantum well laser was actually reported in the literature, and through 1990, the reported bandwidths were below 10 GHz [45]. Over the next several years, the complicated carrier dynamics of quantum well lasers were studied and dynamic effects specific to quantum wells that influence the high speed properties were specified and analyzed. These understandings led to the improved results, and the bandwidths above 40 GHz that have been reported to date.

The additional dynamics essentially involve the process by which carriers are captured into the quantum well, and by which they escape from the wells. This process has been studied in detail in many publications [20, 46-50] and is visually represented in Figure 5. The picture in Figure 5 represents a classical description of the dynamics, with drift and diffusion governing the carrier flow from the SCH to the quantum wells. A local capture time into, and an escape time out of, the wells have been defined in a complete rate equation analysis. The capture and escape process is quantum mechanical in nature and so this description is approximate at best, but it seems to be satisfactory.

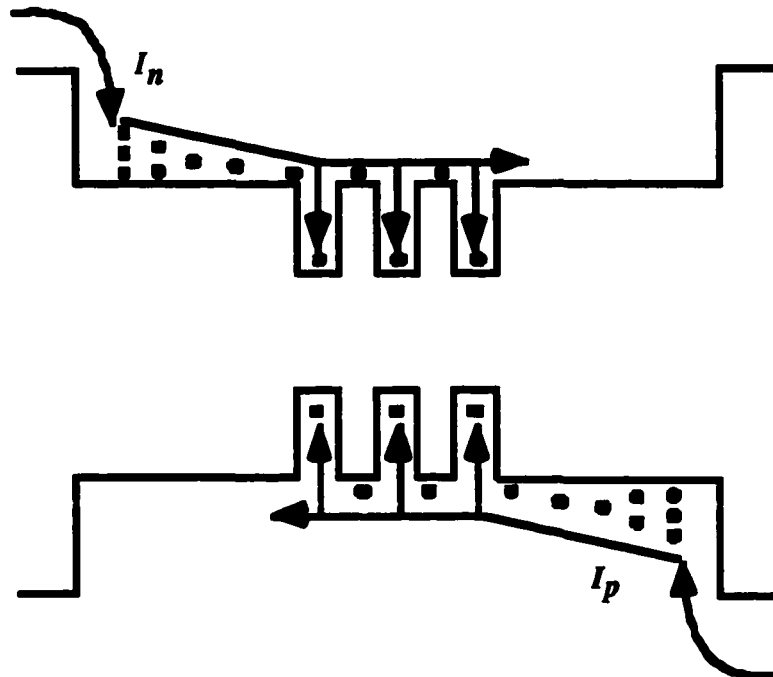


Figure 5. Important transport processes in quantum well lasers.  $I_n$  is the electron current and  $I_p$  is the hole current.

The carrier transport processes in quantum well lasers reduce the differential gain, increase the nonlinear damping, and introduce a single-pole rolloff in the modulation response. The rolloff is a direct manifestation of the transport delay time; since the transport delays are fairly low in most high speed laser structures, on the order of 5 ps, the rolloff occurs at high frequencies. If a device is made with an unusually long SCH region the rolloff will occur at lower frequencies. The reduction in differential gain is approximately related to the ratio of the total transport time (including the diffusive transport across the SCH and the quantum capture) to the escape time through the factor  $\chi = 1 + \tau_r/\tau_e$ , where  $\tau_r$  is the transport time and  $\tau_e$  is the escape time. The nonlinear damping results from an enhancement of  $\varepsilon$  that is related to carrier relaxation from the 3-D region into the lasing subband. Models that

identify 3 carrier levels have proven accurate for predicting responses above 30 GHz. Each carrier level is assigned its own time constant and rate equation [51]. The three levels are (1) the classical transport level, representing carriers moving by drift-diffusion in the confinement region. (2) The capture level, representing carriers moving in the barrier-confinement regions close to the wells. The barrier -well interaction is characterized by quantum capture and escape times. (3) The gain level, where stimulated recombination occurs and contributes to gain and light emission. Even more sophisticated models have been developed that study the spatial distribution of carriers in quantum wells both statically and dynamically. These models show that the carrier distribution and dynamic response is highly nonuniform across the quantum wells in the MQW structure [52, 53].

The best results from high speed quantum well lasers are obtained by making transport and capture times short, while making the escape time from the wells long. This means that the SCH width should be made as small as possible while still retaining acceptable optical confinement factor. Deep wells provide better performance than shallow wells since the carrier confinement is better, and there is relatively less population in the barrier and the confinement regions. Multiple quantum well structures are preferred to single quantum well structures for the same reason: single quantum wells experience severe gain saturation due to carrier overflow from the well, and will not reach the power levels needed for ultrahigh frequency operation. The carrier escape time  $\tau_e$  also decreases as the carrier density in the well increases, further degrading the high frequency properties. The optical confinement is also higher in MQW structures; this, along with the superior carrier confinement, leads to lower threshold gain and higher bandwidth.

### 1.5 Wafer bonded in plane lasers

Wafer bonding and wafer fusion have become important, and even indispensable techniques for optoelectronic device fabrication. Long wavelength vertical cavity lasers show excellent performance when fusion is incorporated in the process [54, 55], but, otherwise, work poorly and are plagued by severe growth difficulties due to the necessity of growing very thick mirror stacks. High efficiency, high multiplication avalanche photodetectors [56] can only be fabricated by fusing highly lattice mismatched, dissimilar materials together. Optoelectronic integration with silicon circuits is made feasible by fusing optical materials to silicon. A host of other devices impossible to make by epitaxial growth alone have become realistic with the implementation of wafer bonding and fusion technology [57, 58]. The microstrip laser, for example, is novel in that the transference of a thin laser epi film onto a thick gold layer has been made possible by metal bonding. Just as bonding to silicon lends practical credence to the idea of integrating optoelectronic devices with silicon circuits, bonding to gold could possibly permit layout of an entire optoelectronic-electronic circuit on a thick gold heat sink for excellent high speed and high power performance.

Several edge emitting laser structures have been fabricated with wafer bonding technology. Examples of these include InP lasers emitting at 1.3 and 1.55  $\mu\text{m}$  on silicon [59, 60], and 1  $\mu\text{m}$  InGaAs lasers on silicon [61]. Both 1.3 and 1.55  $\mu\text{m}$  structures show equivalent threshold and efficiency performance relative to the an active region fabricated on the InP growth substrate, and the 1  $\mu\text{m}$  laser shows just minor degradation. The 1.3  $\mu\text{m}$  lasers actually show higher power performance

and a lower thermal resistance when fabricated on silicon because of silicon's superior thermal conductivity [56, 59]. The bonding conditions for these lasers were very different: the 1.55  $\mu\text{m}$  lasers were fabricated by growing a buffer layer of InP on the silicon, and then bonding at 700 °C directly to the epi, with InP as the top layer [60]. The 1.3  $\mu\text{m}$  lasers, in contrast, were bonded directly to the silicon at a low temperature of 400 °C, and utilized a thin film bonding process - the bonding was done after substrate removal, rather than before. The process is slightly more complicated and involves initially mounting the wafer with wax on a glass slide to permit substrate removal, but eliminated thin film cracking caused by stress redistribution during the 400 °C bonding. The malleability of the thin film may also contribute to a greater bonding process latitude [59]. Schematics of the thick and thin film bonding process are shown in Figure 6. The bonding process used for the microstrip laser is outlined in Chapter 4, and is a thick film bonding process; very slow temperature ramping is required for successful bonding so the epi film can accommodate the thermal stress more easily. The gold layer is malleable and may serve the same function of stress relaxation without damaging the epi layer that the epi film serves in the thin film process.

1.55  $\mu\text{m}$  InP lasers have also been fabricated on GaAs [62-64]. These lasers show little or no degradation in threshold and efficiency compared to lasers from the same material fabricated on the InP growth substrate [63], and in certain cases, the threshold performance has even been better [64]. In the latter case, the improvement was brought about by patterned bonding. The patterned bonding creates a structure in which current is confined in the lower cladding as well as the upper cladding, lowering the threshold by about 10%. Finally, the wafer bonding technique permits

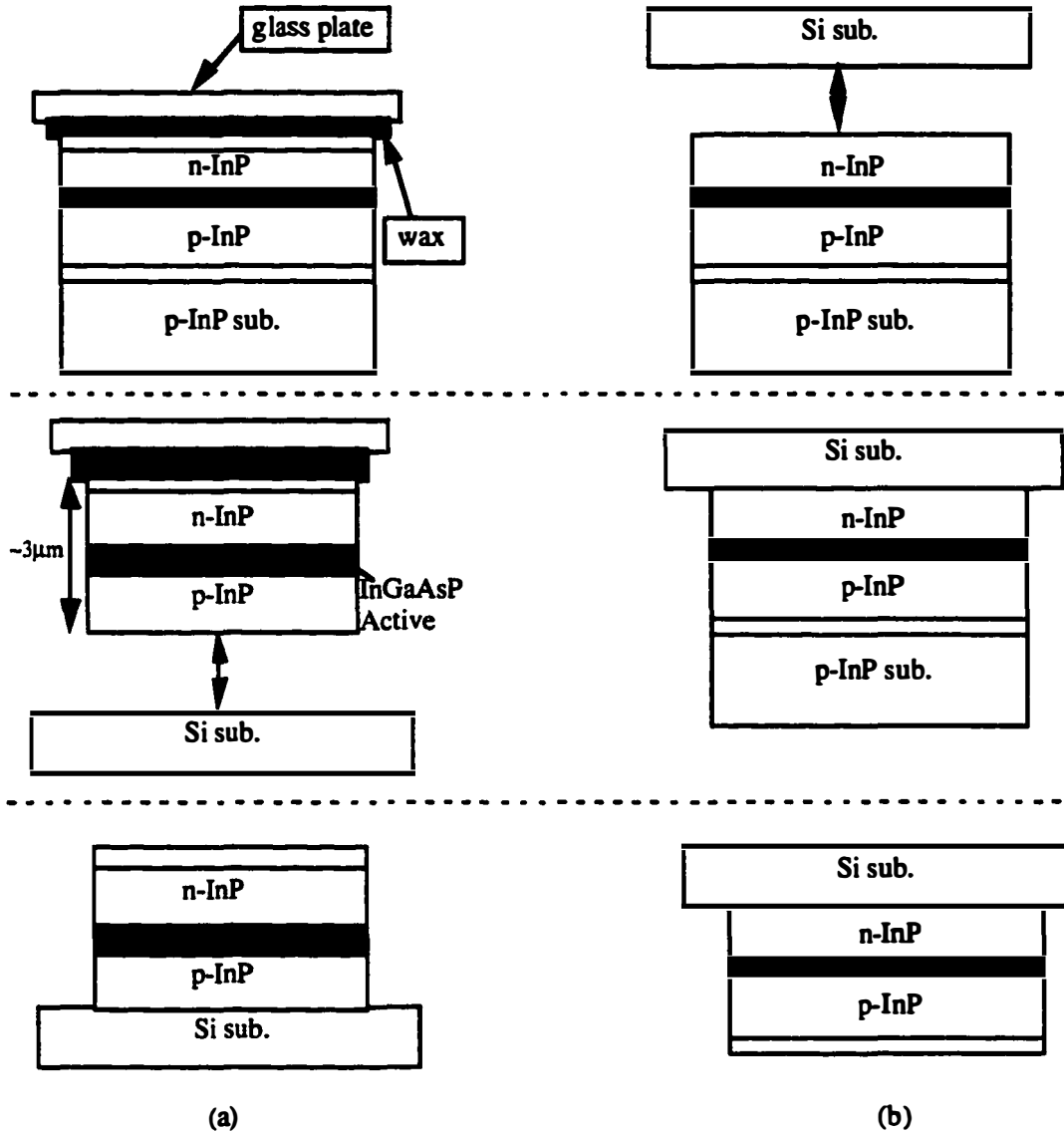


Figure 6. (a) Thin film bonding. Bonding to Si is performed after substrate removal. (b) Thick film bonding. Bonding to Si is performed before substrate removal.

relative lattice orientations of epi and substrate that cannot be successfully grown, but are useful in applications such as nonlinear optics [65].

In all these structures, SEM pictures and other techniques for identifying defects show that dislocations accommodating the lattice mismatch are edge dislocations localized at the bonding interface. They do not propagate through the structure as they do during growth. This is not really an issue for the microstrip laser, as the bonding method does not involve joining two different semiconductors together, but rather bonds epi and substrate through a metal medium.

Other than the microstrip laser, one bonded in-plane laser that does not use semiconductor - semiconductor bonding has been reported. In this particular structure, shown in Figure 7, InP is bonded to silicon dioxide ( $\text{SiO}_2$ ) at  $650^\circ\text{C}$ , after which a channel is etched in the InP, mass transport is used to coat the  $\text{SiO}_2$  with InP, and a laser structure is grown in the channel [66]. The mass transport of the InP in the structure occurs at temperatures around  $600^\circ\text{C}$  and is needed to ensure good regrowth. The  $\text{SiO}_2$  is a current blocking layer around the active region that significantly reduces leakage currents, and contributes to high power performance: the output power of this structure is more than 20% higher than a comparable device using SI InP for current blocking. The SI InP only insulates against electron current, and hole injection introduces excess leakage that is not present in the  $\text{SiO}_2$  structure [66, 67].

## 1.6 Overview

The microstrip laser represents a novel structure that incorporates many ideas used in the design of high frequency and high power lasers, as well as sharing a design perspective and flexibility, as well as fabrication similarities, with other wafer bonded lasers. It is clear that in order to fabricate an excellent high frequency laser,

a large number of difficult conditions must be first met. These include effects purely related to high frequency performance, such as those discussed in depth in Chapter 2, *Microwave propagation effects in semiconductor lasers*, as well as those related to DC performance, as are discussed in Chapter 3, *DC analysis of microstrip laser properties*. These chapters aim to present the physics of the microstrip laser and while doing so, illuminate all these ideas more clearly and show why the microstrip laser is an excellent structure, for both static and high frequency operation. Chapters 4 and 5, *Microstrip laser fabrication and Device results*, present the experimental realization of those ideas.

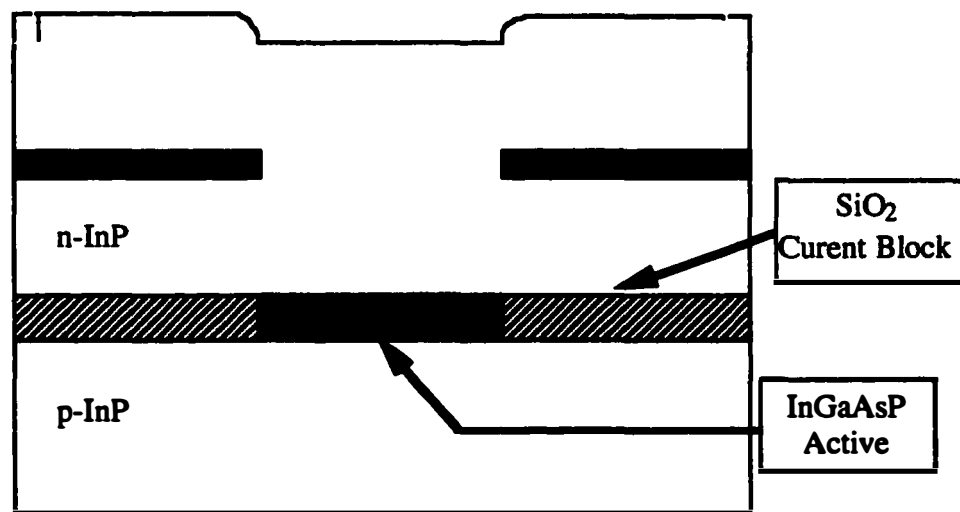


Figure 7. Cross section of in-plane laser structure in which InP is bonded to SiO<sub>2</sub>, which becomes a current block for the structure after processing and regrowth [66].

## References

- [1] J. Bristow, J. Lehman, Y. Liu, M. Hibbs-Brenner, L. Galarnau, and R. Morgan, "Recent progress in short distance optical interconnects," presented at Optoelectronic Interconnects and Packaging IV, San Jose, CA, USA, 1997.
- [2] H. Horikawa, H. Wada, Y. Matsui, T. Yamada, Y. Ogawa, and Y. Kawai, "High-power and high-speed semi-insulating blocked V-grooved inner-stripe lasers at 1.3  $\mu\text{m}$  wavelength fabricated on p-InP substrates," *Applied Physics Letters*, vol. 54, pp. 1077-9, 1989.
- [3] J. E. Bowers, "Modulation properties of semiconductor lasers," in *Optoelectronic Technology and Lightwave Communications Systems*, C. Lin, Ed. New York: Van Nostrand Reinhold, 1989, pp. 299 - 334.
- [4] E. Ackerman, C. Cox, III, G. Betts, H. Roussell. K. Ray, and F. O'Donnell, "Input impedance conditions for minimizing the noise figure of an analog optical link," presented at No.97CH36037) 1997 IEEE MTT-S International Microwave Symposium Digest, Denver, CO, USA, 1997.
- [5] J. E. Bowers, "High speed semiconductor laser design and performance," *Solid State Electron*, vol. 30, pp. 1-11, 1987.
- [6] R. Nagarajan, "Carrier transport effects in quantum well lasers: an overview," *Optical and Quantum Electron.*, vol. 26, pp. 647-666, 1994.
- [7] N. Tessler and G. Eisenstein, "On carrier injection and gain dynamics in quantum well lasers," *IEEE J. Quantum Electron*, vol. 29, pp. 1586-1595, 1993.
- [8] M. J. W. Rodwell, S. T. Allen, R. Y. Yu, M. G. Case, U. Bhattacharya, M. Reddy, E. Carman, M. Kamegawa, Y. Konishi, J. Pusi, R. Pallela, and J. Esch, "Active and nonlinear wave propagation devices in ultrafast electronics and optoelectronics (and prolog)," *Proceedings of the IEEE*, vol. 82, pp. 1035-59, 1994.
- [9] D. A. Tauber, R. Spickermann, R. Nagarajan, T. Reynolds, J. A. L. Holmes, and J. E. Bowers, "Inherent bandwidth limits in semiconductor lasers due to distributed microwave effects," *Appl. Phys. Lett*, vol. 64, pp. 1610-1612, 1994.
- [10] S. Tiwari, "Transmission-line delay limitations of laser bandwidths," *IEE Proc. - Optoelectron*, vol. 141, pp. 163-165, 1994.

- [11] B. Wu, J. B. Georges, D. M. Cutrer, and K. Y. Lau, "On distributed microwave effects in semiconductor lasers and their practical implications," *Appl. Phys. Lett.*, vol. 67, pp. 467-469, 1995.
- [12] D. M. Cutrer, J. B. Georges, T. C. Wu, B. Wu, and K. Y. Lau, "Resonant modulation of *single* contact monolithic semiconductor lasers at millimeter wave frequencies," *Appl. Phys. Lett.*, vol. 66, pp. 2153-2155, 1995.
- [13] K. C. Sum and N. J. Gomes, "Harmonic generation limitations in gain-switched semiconductor lasers due to distributed microwave effects," *Applied Physics Letters*, vol. 71, pp. 1154-5, 1997.
- [14] S. N. G. Chu, R. A. Logan, M. Geva, and N. T. Ha, "Concentration dependent Zn diffusion in InP during metalorganic vapor phase epitaxy," *Journal of Applied Physics*, vol. 78, pp. 3001-7, 1995.
- [15] J. D. Ralston, S. Weisser, I. Esquivias, E. C. Larkins, J. Rosenzweig, P. J. Tasker, and J. Fleissner, "Control of differential gain, nonlinear gain and damping factor for high-speed application of GaAs-based MQW lasers," *IEEE J. Quantum Electron.*, vol. 29, pp. 1648-1658, 1993.
- [16] A. Kasukawa, N. Iwai, N. Yamanaka, and N. Yokouchi, "Very high characteristic temperature and constant differential quantum efficiency 1.3- $\mu\text{m}$  GaInAsP-InP strained-layer quantum-well lasers by use of temperature dependent reflectivity (TDR) mirror," *IEEE Journal on Selected Topics in Quantum Electronics*, vol. 1, pp. 293-300, 1995.
- [17] P. J. A. Thijs, L. F. Tiemeijer, J. J. M. Binsma, and T. v. Dongen, "Progress in long wavelength strained-layer InGaAs(P) quantum-well semiconductor lasers and amplifiers," *IEEE Journal of Quantum Electronics*, vol. 30, pp. 477-499, 1994.
- [18] M. Sagawa, T. Toyonaka, K. Hiramoto, K. Shinoda, and K. Uomi, "High-power highly-reliable operation of 0.98- $\mu\text{m}$  InGaAs-InGaP strain-compensated single-quantum-well lasers with tensile-strained InGaAsP barriers," *IEEE Journal on Selected Topics in Quantum Electronics*, vol. 1, pp. 189-94, 1995.
- [19] M. R. Gokhale, J. C. Dries, P. V. Studenkov, S. R. Forrest, and D. Z. Garbuzov, "High-power high-efficiency 0.98- $\mu\text{m}$  wavelength InGaAs-(In)GaAs(P)-InGaP broadened waveguide lasers grown by gas-source molecular beam epitaxy," *IEEE Journal of Quantum Electronics*, vol. 33, pp. 2266-76, 1997.
- [20] R. Nagarajan, T. Fukushima, M. Ishikawa, J. E. Bowers, R. S. Geels, and L. A. Coldren, "Transport limits in high speed quantum well lasers: Experiment and theory," *IEEE Photon. Tech. Lett.*, vol. 4, pp. 121-123, 1992.

- [21] J. Piprek and W. Both, "Thermal resistance of InGaAs/InP laser diodes," *Journal of Thermal Analysis*, vol. 36, pp. 1441-1456, 1990.
- [22] H. Wada, H. Horikawa, Y. Matsui, Y. Ogawa, and Y. Kawai, "High-power and high-speed 1.3  $\mu\text{m}$  V-grooved inner-stripe lasers with new semi-insulating current confinement structures on p-InP substrates," *Applied Physics Letters*, vol. 55, pp. 723-5, 1989.
- [23] M. Ohkubo, T. Ijichi, A. Iketani, and T. Kikuta, "980-nm aluminum-free InGaAs/InGaAsP/InGaP GRIN-SCH SL-QW lasers," *IEEE Journal of Quantum Electronics*, vol. 30, pp. 408-14, 1994.
- [24] G. K. Reeves, S. L. Shi, and G. T. Ong, "Temperature distribution in GaAs lasers with diamond film heatsink," *Electronics Letters*, vol. 28, pp. 2317-18, 1992.
- [25] M. Sagawa, K. Hiramoto, T. Toyonaka, K. Shinoda, and K. Uomi, "High power COD-free operation of 0.98  $\mu\text{m}$  InGaAs/GaAs/InGaP lasers with noninjection regions near the facets," *Electronics Letters*, vol. 30, pp. 1410-11, 1994.
- [26] S. Weisser, E. C. Larkins, K. Czotscher, W. Benz, J. Daleiden, I. Esquivias, J. Fleissner, J. D. Ralston, B. Romero, R. E. Sah, A. Schönfelder, and J. Rosensweig, "Damping - limited modulation bandwidths up to 40 GHz in undoped short - cavity In<sub>0.35</sub>Ga<sub>0.65</sub>As - GaAs multiple quantum well lasers," *IEEE Photon. Tech. Lett.*, vol. 8, pp. 608-610, 1996.
- [27] O. Kjebon, R. Schatz, S. Lourdudoss, S. Nilsson, B. Stålnacke, and L. Backbom, "30 GHz direct modulation bandwidth in detuned loaded InGaAsP DBR lasers at 1.55  $\mu\text{m}$  wavelength," *Electronics Letters*, vol. 33, pp. 488-489, 1997.
- [28] I. Suemune, L. A. Coldren, M. Yamanishi, and Y. Kan, "Extremely wide modulation bandwidth in a low threshold current strained quantum well laser," *Appl. Phys. Lett.*, vol. 53, pp. 1378-1380, 1988.
- [29] R. Nagarajan, T. Fukushima, J. E. Bowers, R. S. Geels, and L. A. Coldren, "Single quantum well strained InGaAs/GaAs lasers with large modulation bandwidth and low damping," *Electron. Lett.*, vol. 27, pp. 1058-1060, 1991.
- [30] L. F. Lester, W. J. Schaff, X. Song, and L. F. Eastman, "Optical and RF characteristics of short - cavity - length multiquantum - well strained - layer lasers," *IEEE Photon. Tech. Lett.*, vol. 3, pp. 1049-1051, 1991.

- [31] E. Meland, R. Holmstrom, J. Schlafer, R. B. Lauer, and W. Powazinik, "Extremely high-frequency (24 GHz) InGaAsP diode lasers with excellent modulation efficiency," *Electron. Lett.*, vol. 26, pp. 1827-1829, 1990.
- [32] L. F. Lester, S. S. O'Keefe, W. J. Schaff, and L. F. Eastman, "Multiquantum well strained-layer lasers with improved low frequency response and very low damping," *Electron. Lett.*, vol. 28, 1992.
- [33] P. A. Morton, R. A. Logan, T. T. Ek, J. P. F. Sciortino, A. M. Sergent, R. K. Montgomery, and B. T. Lee, "25 GHz bandwidth 1.55  $\mu\text{m}$  GaInAsP p-doped strained multiquantum well lasers," *Electron. Lett.*, vol. 28, pp. 2156-2157, 1992.
- [34] Y. Hirayama, M. Morinaga, N. Suzuki, and M. Nakamura, "Extremely reduced nonlinear K-factor in high-speed strained layer multiquantum well DFB lasers," *Electron. Lett.*, vol. 27, pp. 875-876, 1991.
- [35] I. F. Lealman, M. Bagley, D. M. Cooper, N. Fletcher, M. Harlow, S. D. Perrin, R. H. Walling, and L. D. Westbrook, "Wide bandwidth multiple quantum well 1.55  $\mu\text{m}$  lasers," *Electron. Lett.*, vol. 27, pp. 1191-1193, 1991.
- [36] A. Mar, P. A. Morton, and J. E. Bowers, "Optimum facet reflectivity for high speed lasers," *Electron. Lett.*, vol. 26, pp. 1382-1384, 1990.
- [37] J. G. Wasserbauer, J. E. Bowers, M. J. Hafich, P. Silvestre, L. M. Woods, and G. Y. Robinson, "Specific contact resistivity of InGaAs/InP p-isotype heterojunctions," *Electron. Lett.*, vol. 28, pp. 1568-1570, 1992.
- [38] P. A. Morton, T. T. Ek, R. A. Logan, N. Chand, K. Wecht, A. M. Sergent, and J. P. F. Sciortino, "Packaged 1.55  $\mu\text{m}$  DFB laser with 25 GHz modulation bandwidth," *Electron. Lett.*, vol. 30, pp. 2044-2046, 1994.
- [39] R. T. Huang, D. Wolf, W. H. Cheng, C. L. Jiang, R. Agarwal, D. renner, A. Mar, and J. E. Bowers, "High-speed low-threshold InGaAsP semi-insulating buried crescent lasers with 22 GHz bandwidth," *IEEE Photon.Tech. Lett.*, vol. 4, pp. 1992, 1992.
- [40] W. H. Cheng, K. D. Buehring, A. Appelbaum, D. Renner, S. Chin, C. B. Su, A. Mar, and J. E. Bowers, "High-speed and low-relative intensity noise 1.3  $\mu\text{m}$  InGaAsP semi-insulating buried crescent lasers," *IEEE J. Quantum Electron.*, vol. 27, pp. 1642-1647, 1991.
- [41] R. Nagarajan, T. Fukushima, J. E. Bowers, R. S. Geels, and L. A. Coldren, "High Speed InGaAs/GaAs strained multiple quantum well lasers with low damping," *Appl. Phys. Lett.*, vol. 64, pp. 2326-2328, 1991.

- [42] D. Z. Tsang and Z. L. Liao, "Sinusoidal and digital high-speed modulation of p-substrate mass-transported diode lasers," *IEEE J. Lightwave Technol.*, vol. 5, pp. 300-304, 1987.
- [43] L. A. Coldren and S. W. Corzine, *Diode Lasers and Photonic Integrated Circuits*. New York: John Wiley and Sons, 1995.
- [44] K. Uomi, T. Mishima, and N. Chinone, "Ultrahigh relaxation oscillation frequency (up to 30 GHz) of highly p-doped GaAs/GaAlAs multiple quantum well lasers," *Appl. Phys. Lett.*, vol. 53, pp. 78-80, 1987.
- [45] W. F. Sharfin, J. Schlafer, W. Rideout, B. Elman, R. B. Lauer, J. LaCourse, and F. D. Crawford, "Anomalously high damping in strained InGaAs-GaAs single quantum well lasers," *IEEE Photon. Tech. Lett.*, vol. 3, pp. 193-195, 1991.
- [46] N. Tessler and G. Eisenstein, "Transient carrier dynamics and photon-assisted transport in multiple-quantum-well lasers," *IEEE Photon. Tech. Lett.*, vol. 5, pp. 291-293, 1993.
- [47] R. Nagarajan, T. Fukushima, S. W. Corzine, and J. E. Bowers, "Effects of carrier transport on high speed quantum well lasers," *Appl. Phys. Lett.*, vol. 59, pp. 1835-1837, 1991.
- [48] S. C. Kan and K. Y. Lau, "Intrinsic equivalent circuit of quantum-well lasers," *IEEE Photon. Tech. Lett.*, vol. 4, pp. 528-530, 1992.
- [49] S. C. Kan, D. Vassilovski, T. C. Wu, and K. Y. Lau, "Quantum capture and escape in quantum-well lasers - implications on direct modulation bandwidth limitations," *IEEE Photon. Tech. Lett.*, vol. 4, pp. 428-431, 1992.
- [50] B. Zhao, T. R. Chen, J. Iannelli, Y. H. Zhuang, Y. Yamada, and A. Yariv, "State filling effect on spectral linewidth of quantum well lasers," *Applied Physics Letters*, vol. 62, pp. 1200-2, 1993.
- [51] N. Tessler, R. Nagar, and G. Eisenstein, "Structure dependent modulation responses in quantum well lasers," *IEEE J. Quantum Electron.*, vol. 28, pp. 2242-2250, 1992.
- [52] N. Tessler and G. Eisenstein, "Distributed nature of quantum well lasers," *Appl. Phys. Lett.*, vol. 62, pp. 10-12, 1993.
- [53] N. Suzuki and M. Ishikawa, "A small-signal frequency response model with electron and hole transports in multiquantum-well lasers," *IEEE Photonics Technology Letters*, vol. 5, pp. 767-70, 1993.

- [54] N. M. Margalit, D. I. Babic, K. Streubel, R. P. Mirin, R. L. Naone, J. E. Bowers, and E. L. Hu, "Submilliamp long wavelength vertical cavity lasers," *Electronics Letters*, vol. 32, pp. 1675-7, 1996.
- [55] N. M. Margalit, S. Z. Zhang, and J. E. Bowers, "Vertical cavity lasers for telecom applications," *IEEE Communications Magazine*, vol. 35, pp. 164-70, 1997.
- [56] A. R. Hawkins, W. Weishu, P. Abraham, K. Streubel, and J. E. Bowers, "High gain-bandwidth-product silicon heterointerface photodetector," *Applied Physics Letters*, vol. 70, pp. 303-5, 1997.
- [57] A. Black, A. R. Hawkins, N. M. Margalit, D. I. Babic, A. L. Holmes, Jr., Y. L. Chang, P. Abraham, J. E. Bowers, and E. L. Hu, "Wafer fusion: materials issues and device results," *IEEE Journal of Selected Topics in Quantum Electronics*, vol. 3, pp. 943-51, 1997.
- [58] Z. H. Zhu, F. E. Ejeckam, Y. Qian, Z. Jizhi, Z. Zhenjun, G. L. Christenson, and Y. H. Lo, "Wafer bonding technology and its applications in optoelectronic devices and materials," *IEEE Journal of Selected Topics in Quantum Electronics*, vol. 3, pp. 927-36, 1997.
- [59] H. Wada and T. Kamijoh, "1.3-  $\mu\text{m}$  InP-InGaAsP lasers fabricated on Si substrates by wafer bonding," *IEEE Journal of Selected Topics in Quantum Electronics*, vol. 3, pp. 937-42, 1997.
- [60] K. Mori, K. Tokutome, and S. Sugou, "Low-threshold pulsed operation of long-wavelength lasers on Si fabricated by direct bonding," *Electronics Letters*, vol. 31, pp. 284-5, 1995.
- [61] Y. H. Lo, R. Bhat, D. M. Hwang, C. Chua, and C. H. Lin, "Semiconductor lasers on Si substrates using the technology of bonding by atomic rearrangement," *Applied Physics Letters*, vol. 62, pp. 1038-40, 1993.
- [62] Y. Okuno, M. Aoki, T. Tsuchiya, and K. Uomi, "Fabrication of (001) InP-based 1.55-  $\mu\text{m}$  wavelength lasers on a (110) GaAs substrate by direct bonding (a prospect for free-orientation integration)," *Applied Physics Letters*, vol. 67, pp. 810-12, 1995.
- [63] Y. H. Lo, R. Bhat, D. M. Hwang, M. A. Koza, and T. P. Lee, "Bonding by atomic rearrangement of InP/InGaAsP 1.5  $\mu\text{m}$  wavelength lasers on GaAs substrates," *Applied Physics Letters*, vol. 58, pp. 1961-3, 1991.
- [64] A. V. Syrbu, J. Fernandez, J. Behrend, C. A. Berseth, J. F. Carlin, A. Rudra, and E. Kapon, "InGaAs/InGaAsP/InP edge emitting laser diodes on p-GaAs

substrates obtained by localised wafer fusion," *Electronics Letters*, vol. 33, pp. 866-8, 1997.

[65] Y. Okuno, K. Uomi, M. Aoki, and T. Tsuchiya, "Direct wafer bonding technique aiming for free-material and free-orientation integration of semiconductor materials," *IEICE Transactions on Electronics*, vol. E80-C, pp. 682-8, 1997.

[66] H. Wada, Y. Ogawa, and T. Kamijoh, "Novel current-blocking structures in semiconductor lasers using directly bonded InP-SiO<sub>2</sub>/InP," *IEEE Photonics Technology Letters*, vol. 6, pp. 1403-5, 1994.

[67] P. J. Corvini and J. E. Bowers, "Model for trap filling and avalanche breakdown in semi-insulating Fe:InP," *Journal of Applied Physics*, vol. 82, pp. 259-69, 1997.

## **Chapter 2**

### **Microwave propagation effects in semiconductor lasers**

As was discussed in the introduction, the high frequency properties of semiconductor lasers are set by both material and structural factors. Structural is used in this context to describe a fabricated laser - for example, a ridge laser structure or a buried laser structure - and is distinct from material factors associated with an unprocessed laser wafer. The ways by which the material and the structural factors link to dynamic performance can be conveniently separated into three categories: (1) The device physics, which determine relevant carrier diffusion times, carrier capture times, and carrier recombination times. (2) The optical waveguide, which determines the photon lifetime, thus strongly affecting the stimulated emission lifetime. (3) The electrical structure, which affects the dynamics through the RC time constant and through frequency dependent microwave propagation effects. This last topic, the physics of microwave propagation in semiconductor lasers, and how dynamics and modulation response are affected by it, is the subject of this chapter.

#### **2.1 Background**

Microwave propagation effects in semiconductor lasers show up at the high end of the laser bandwidth spectrum. If the laser bandwidth is very high, the microwave propagation can be the factor limiting the modulation response. More specifically, the frequency dependence of the complex propagation constant affects the spatial distribution of the injected current, thus causing the semiconductor laser

to be a distributed rather than a lumped electrical element [1]. The traditional treatment of the semiconductor laser assumes the laser is a lumped element in which the high frequency current is uniformly distributed along the device length. The small signal rate equation analysis which is used to calculate optical modulation response uses this assumption, and while it is valid at low and moderate frequencies, it is not valid at the very high frequencies characteristic of the best current high speed devices [1-3]. Invoking a lumped analysis will result in incorrect calculations of the dynamic response as well as misinterpretation of dynamic measurements.

Distributed effects occur because electromagnetic waves travel at a finite speed, so the modulation signal applied at a feed point on the device takes time to travel to the far end of the device. When this time delay is comparable to the modulation period, the voltages and currents along the device length are out of phase with each other and the laser must be treated as a microwave waveguide (distributed element) rather than as a lumped element. This transition from lumped to distributed element is diagrammed in Figure 1.

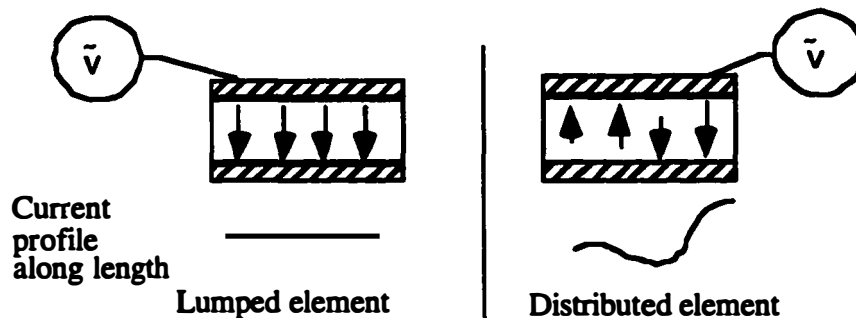


Figure 1. Distinction between a lumped electrical element and a distributed electrical element semiconductor laser. The current profile along the length of the distributed element is nonuniform.

Time delays mean phase shifted signals. Typically, a 90 degree phase shift of the microwave signal across the device is a good figure of merit for determining the frequencies and device lengths for which distributed effects are important. This is equivalent to specifying a device length equal to a quarter wavelength at the frequency of interest. When this criterion is met, the microwave propagation will influence the input-output transfer function, and any dynamic response of the laser at frequencies for which a quarter wave or more exists in the device should be analyzed including the effects of microwave propagation. This is true of the small signal modulation response, the large signal modulation response, the gain switched response, and the mode locked response [1, 4, 5]. Figure 2 shows the microwave quarter wavelength versus frequency for three different microwave phase velocities,  $0.3c$ ,  $0.2c$ , and  $0.1c$ , where  $c$  is the vacuum speed of light. As can be seen in the plot, at  $0.1c$ , the quarter wavelength is below  $200 \mu m$  at a frequency of 40 GHz. Since  $200 \mu m$  is a typical length for a high frequency laser, the plot demonstrates that the highest speed semiconductor lasers reported to date should be treated as distributed element structures. As will be discussed and calculated later in this chapter, and shown experimentally, the  $0.1c$  value for the phase velocity is quite realistic; the semiconductor laser is a slow wave microwave structure, as are most semiconductor diode devices [6], meaning that microwaves propagate at velocities slower than would be expected from a simplistic calculation based on the material dielectric constant.

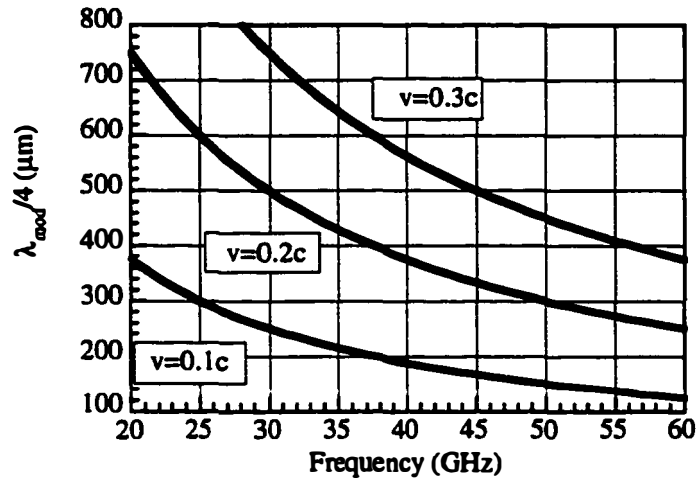


Figure 2. Quarter wavelength of microwave signal versus modulation frequency for several different phase velocities. For a signal traveling at  $0.1c$ , the quarter wavelength is less than  $200 \mu\text{m}$  at  $40 \text{ GHz}$  - a typical length for high speed lasers.

This chapter will analyze this problem in the following order. First, the semiconductor laser structure will be analyzed as a microwave waveguide, and a modal structure will be proposed and justified. An equivalent circuit model for the propagation will be derived from this analysis. Second, the defining characteristics of the propagation, the phase velocity and the attenuation will be determined. These parameters are mathematically contained in the complex propagation constant  $\gamma$ . Third, the propagation properties of conventional and microstrip high speed laser structures will be calculated from the models and compared. The microstrip laser will be shown to be a much improved design. Finally, the way in which distributed effects influence dynamic performance will be discussed and calculated.

## 2.2 Transmission line model of a semiconductor laser

The analysis begins by investigating the microwave transmission line structure of a ridge laser on a doped substrate, shown in Figure 3 (a), and by assuming that the simplest microwave mode this laser transmission line supports is a quasi-TEM (transverse electromagnetic) mode. The justification for the quasi-TEM assumption derives from the fact that the laser is basically a two conductor structure - there are two contacts, each of which is electrically connected to a p or n region. Figure 3 (b) shows a schematic of the microwave currents present in the structure under high frequency modulation. The longitudinal currents in the conductors are always present in any transmission line, as they are needed to satisfy the boundary conditions dictated by Maxwell's equations for confining the microwave. The transverse currents are complex, representing the conduction and displacement currents that both exist in a waveguide structure. The transverse conduction current is associated with a lossy shunt path between the two conductors, as by necessity exists in a forward biased laser diode.

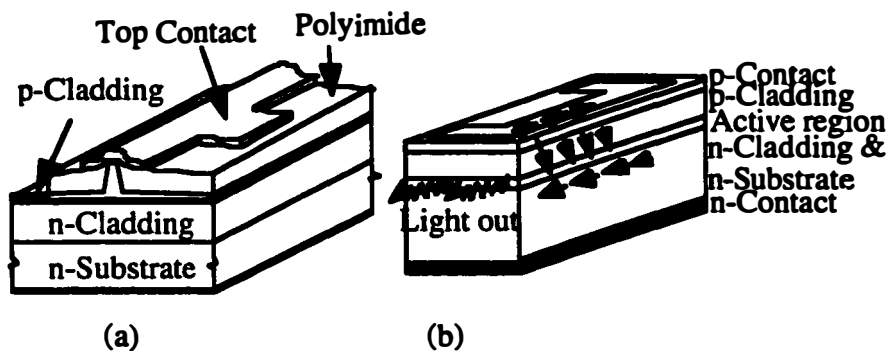
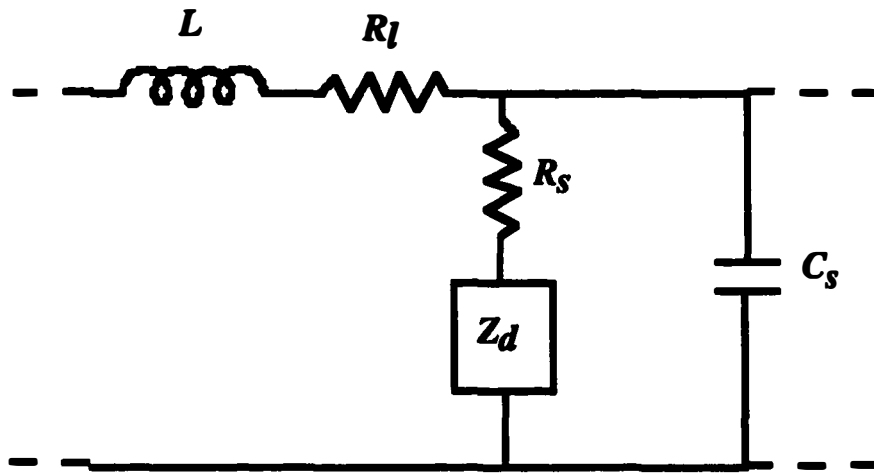


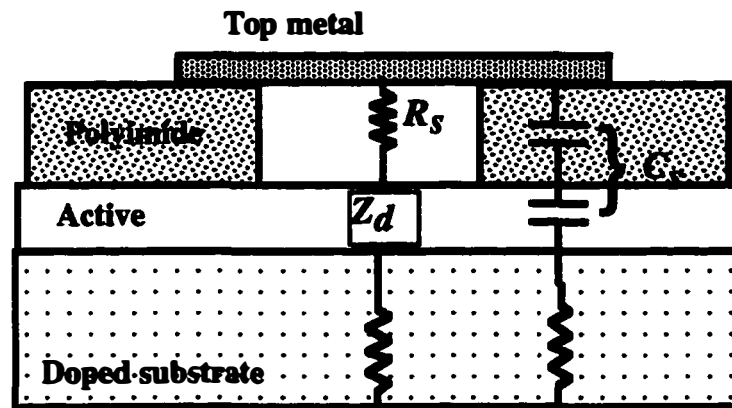
Figure 3. (a) Doped substrate laser. (b) Microwave currents flowing in doped substrate laser under high frequency modulation.

The structure is not a true TEM waveguide, because the longitudinal currents exist in regions of finite conductivity and are thus driven by a longitudinal electric field. However, the analysis will show that the *quasi*-TEM approach is justified because the magnitude of the longitudinal electric field driving the longitudinal currents is much smaller than the magnitude of the field normal to the conductors. The relevant propagation parameters are determined by constructing a distributed equivalent circuit, a section of which is shown in Figure 4 (a), for the transmission line. The equivalent circuit is similar to the one constructed in analyzing the standard lossy transmission line that is commonly found in intermediate electromagnetic texts [7]. Figure 4 (b) shows the cross section of the laser diode, pointing out its contributions to the equivalent circuit, and 4 (c) shows the longitudinal structure of the laser, pointing out its contributions to the circuit.

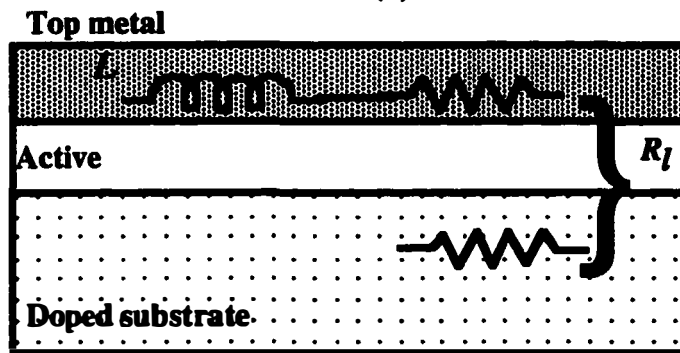


(a)

Figure 4. (a) Distributed electrical equivalent circuit of a high frequency laser diode.



(b)



(c)

Figure 4. (b) Cross sectional circuit representation of the laser. (c) Longitudinal circuit representation of the laser.

The resistance  $R_l$ , of Figure 4, represents resistance to the longitudinal flow of microwave current, and can be calculated from the conductivities of the metallization and the doped substrate. The ohmic losses due to this resistance are referred to as skin losses, since their total value depends on the skin depths to which the fields penetrate in the conducting regions. The spatial distribution of the

longitudinal electric fields is needed to properly calculate  $R_l$ , since the fields are present in differing amounts in regions of different conductivity, and are not uniformly distributed throughout the entire metal and doped regions. The skin depths are frequency dependent, and  $R_l$  is thus a frequency dependent resistance that will be shown to have a large effect on the high frequency current injection in a semiconductor laser.

The inductance  $L$  represents the magnetic field of the propagating wave. The total inductance in the structure is composed of two parts, an external inductance and an internal inductance. The external inductance is the inductance associated with the geometric conductor structure, and is analogous to the inductance calculated for a parallel plate transmission line with no loss. In the case of the parallel plate transmission line, this inductance (per unit length) is equal to  $\mu D/w$ , where  $\mu$  is the magnetic permeability of the medium,  $D$  is the separation of the conductors, and  $w$  is the width of the plates; the calculation is similar in the laser structure, but more complicated, since the fields distribute themselves in a more complicated way than in the lossless parallel plate structure. The additional internal inductance exists because the time varying electric field driving the longitudinal currents generates a magnetic field, according to Maxwell's equations; alternatively, this can be understood by realizing that the magnetic field penetrates into the doped regions, and contributes to inductance there. The internal inductance is therefore closely related to the skin loss, and can be understood as the imaginary component of the skin effect impedance. In a very lossy structure like a semiconductor laser, this inductance turns out to be comparable in magnitude to the external inductance and should not be ignored.

The series resistance,  $R_s$ , represents conduction current in the doped layers of the semiconductor between the p and n contacts. Most of this series resistance comes from the narrow ridge, particularly in the case of p-ridge devices. In p-substrate lasers, the substrate resistance can dominate.

The active region impedance,  $Z_a$ , represents the impedance contribution from the active region. This can be modeled as a parallel RC network, with the differential diode resistance representing the real part of the active region impedance and the diode capacitance representing the imaginary part. The impedance is strongly bias dependent - for unbiased operation, the large diode resistance strongly limits the conduction current between the p and n contacts (for typical device lengths the unbiased diode resistance is about 100 ohms). Under forward biased conditions, the differential diode resistance drops to about 1 ohm or less and the conduction current is set by the resistance of the doped layers. The capacitance is also bias dependent, and is dominated by the depletion capacitance for unbiased operation, and by the diffusion capacitance for forward biased operation. The diffusion capacitance is also frequency dependent and decreases as the frequency increases. The frequency dependence of the diffusion capacitance is caused by the finite carrier lifetime, which limits the rate of charge removal and replenishment at frequencies greater than the reciprocal lifetime.

The shunt capacitance,  $C_s$ , results from metallizations above dielectric material, such as the metal above the polyimide illustrated in Figure 4 (b) and is constant with bias and with frequency.

In calculating the circuit elements, one should be careful not to make a direct analogy between the two metal contacts of the laser structure and a parallel plate

transmission line. Correct analysis requires an understanding of the spatial distributions of the high frequency electric and magnetic fields in the device, which, for the most part, are more strongly determined by the doped semiconductor layers and the diode depletion layer than the metal contacts.

Since the electronic properties of the laser diode are highly nonlinear, particularly the active region impedance that is represented in the circuit model by  $Z_d$ , the circuit model in Figure 4 (a) is only valid for calculating the linearized small signal propagation properties. A full treatment of the large signal response would require replacing the linear elements with non-linear elements representing the full dynamic range of the diode, and calculating the response accordingly.

### 2.3 Longitudinal current flow and series impedance

The series impedance in the circuit model is calculated from the relationship  $Z_s = \frac{E_o}{J_x}$ , where  $E_o$  is the longitudinal electric field incident at the interface between the doped and undoped regions and  $J_x = \int_0^{\infty} J_z(x) dx$  is the integrated current density which can be thought of physically as a surface current density. Since the impedance given in the formula above is a surface impedance in units of ohms/square, the impedance per unit length is determined by dividing  $Z_s$  by the width of the conducting region. The calculation of  $Z_s$  therefore basically involves solving for the current density in the conducting regions. To do this, we assume the normal electric field of a TEM mode is zero inside the doped region (the electric field exists primarily in the depletion region of the diode) but the tangential magnetic field markedly penetrates into the doped region. This is always the case at a conducting

boundary; the termination of the normal fields is set by the charge density and occurs over a much shorter range than does the termination of the tangential fields which is set by the surface current density. The characteristic length scale over which the surface current distributes is, of course, the skin depth. To qualitatively understand the distribution of surface current, Figure 5 qualitatively shows the spatial distribution of the longitudinal fields in the laser structure. Two key points to understand are: (1) Because the upper cladding is thin - less than the microwave skin depths in the semiconductor, most of the upper surface current is carried in the top high conductivity metal contact. (2) Because the substrate is thick, it carries virtually all of the lower surface current, and because of the much smaller conductivity of the doped substrate, that current decays over a much greater distance than does the top surface current.

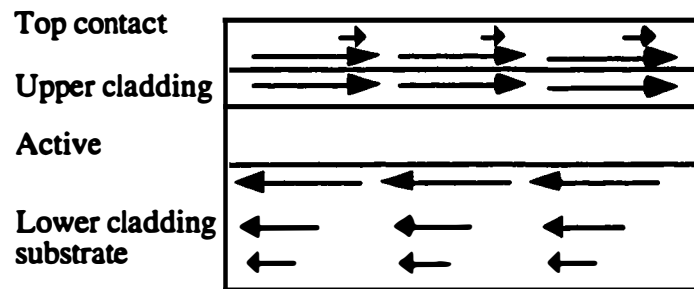


Figure 5. Schematic of the longitudinal electric field vectors in the laser diode. Most of the upper surface current is carried in the top metal contact, whereas almost all of the lower surface current flows in the doped substrate.

Once we know the functional form of the magnetic field in the conducting regions, we can calculate the longitudinal electric field from Maxwell's equations. The current is then calculated from Ohm's law. The method used here is similar to Jackson's (Chap. 8, 2nd ed.) but slightly more involved since it involves several regions of varying conductivity. The relevant equations are

$$\nabla \times \mathbf{H} = \mathbf{J} = \sigma \mathbf{E}$$

$$\nabla \times \mathbf{E} = -j\omega\mu\mathbf{H}$$

where  $H$  is the tangential magnetic field,  $J$  is the conduction current,  $\sigma$  is the conductivity,  $E$  is the longitudinal electrical field,  $\omega$  is the angular frequency and  $\mu$  is the magnetic permeability. We have ignored the displacement current term in the first equation since it is negligible compared to the conduction current in the doped regions and in the metal. The equations can be combined to give a wave equation for the magnetic field in the conductor:  $\frac{\partial^2 H_c}{\partial x^2} + \frac{\sigma\omega\mu}{j} H_c = 0$ . The general solution of this equation in the doped region is  $H_c = C_1 e^{-(l+j)x/\delta_1} + C_2 e^{(l+j)x/\delta_1}$ , where  $C_1$  and  $C_2$  are constants and  $\delta_1 = \sqrt{\frac{1}{\pi f \mu \sigma_1}}$  is the skin depth. Because we have multiple

conducting layers in this problem, we need to retain the positive exponential since it accounts for a reflection at the interface of the doped and metal regions. In the metal, the field solution is simply  $H_m = C_3 e^{-(l+j)x/\delta_2}$  where we assume that the current decays completely in the metal and there is no reflection. We can solve for the three constants from continuity of the electric and magnetic fields at the interface between the two conducting regions, and by knowing the amplitude of the magnetic field  $H_o$  incident upon the doped region. We end up with the following equations:

$$H_o = C_1 + C_2$$

$$C_1 e^{-(l+j)x_1/\delta_1} + C_2 e^{(l+j)x_1/\delta_1} = C_3 e^{-(l+j)x_2/\delta_2}$$

$$\frac{l+j}{\sigma_1 \delta_1} C_1 e^{-(l+j)x_1/\delta_1} - \frac{l+j}{\sigma_1 \delta_1} C_2 e^{(l+j)x_1/\delta_1} = \frac{l+j}{\sigma_2 \delta_2} C_3 e^{-(l+j)x_2/\delta_2}$$

where the third equation is derived from the equation above relating the electric field to the curl of the magnetic field.  $x_1$  is the coordinate of the interface. The solutions for the electric field, magnetic field, and current density in the p-doped region and the metal are shown in Figures 6-8. The interface  $x_1$  is marked by the vertical line in the figures. The parameters used in the calculation are  $\sigma_1 = 2 \times 10^5 \text{ S/m}$ ,  $\sigma_2 = 5 \times 10^7 \text{ S/m}$ ,  $x_1 = 1 \text{ }\mu\text{m}$ , and  $f = 40 \text{ GHz}$ . The important physics made clear from the graphs is that, as expected, more than 99% of the current is carried in the metal contact, and therefore the series resistance contribution from the p-side is quite small since the conductivity of the top contact is high. Note also that the peak magnitude of the longitudinal field is only about 7% of the transverse field (equal to the magnitude of the transverse magnetic field in the SI system), justifying the quasi TEM approximation.

The longitudinal resistance contribution clearly depends on the conductivity of the contact metal. A more subtle point is that unnecessary excess resistance will be generated if the contact is thinner than several skin depths. A good rule of thumb for laser design is to make the contact at least twice as thick as the skin depth at the frequency in which the distributed effects start to manifest themselves. In the case of most lasers, this will be around 20 GHz and the metal layer should be about 1  $\mu\text{m}$  thick.

The calculation of the series loss and internal inductance is now straightforward. The series impedance  $Z_s = \frac{E_z}{J_x}$  gives a series resistance loss per unit length of  $R_s = \text{Re} \left[ \frac{Z_s}{w} \right]$ , where  $w$  is the contact width. The internal inductance  $L_i = \frac{R_s}{\omega}$  accounts for the fact that the magnetic field penetrates the interior of the

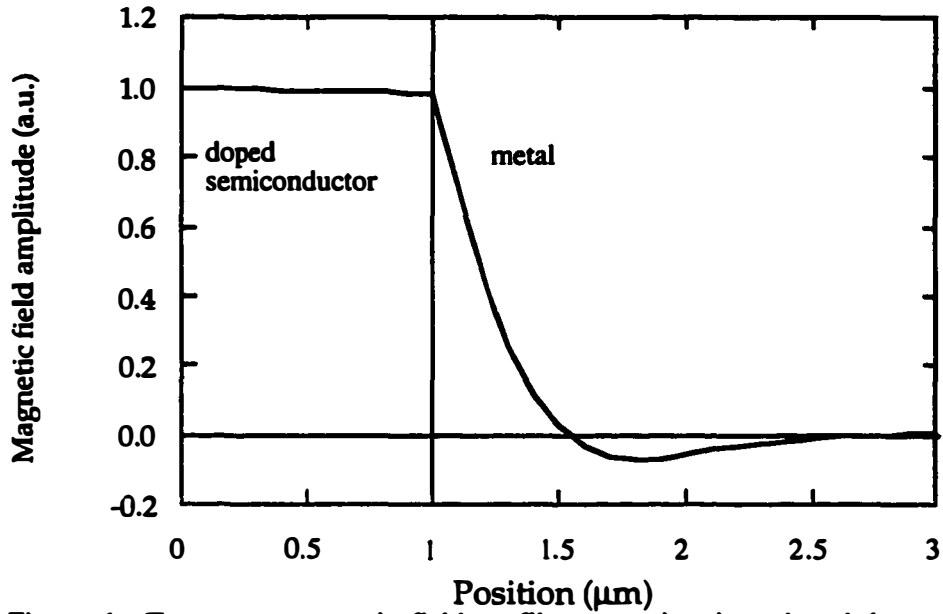


Figure 6. Transverse magnetic field profile vs position in p-doped layer and metal. The interface between semiconductor and metal occurs at  $1 \mu\text{m}$ ; the figure shows that the field decays primarily in the high conductivity conduct. The kink in the curve occurs at the semiconductor metal interface.

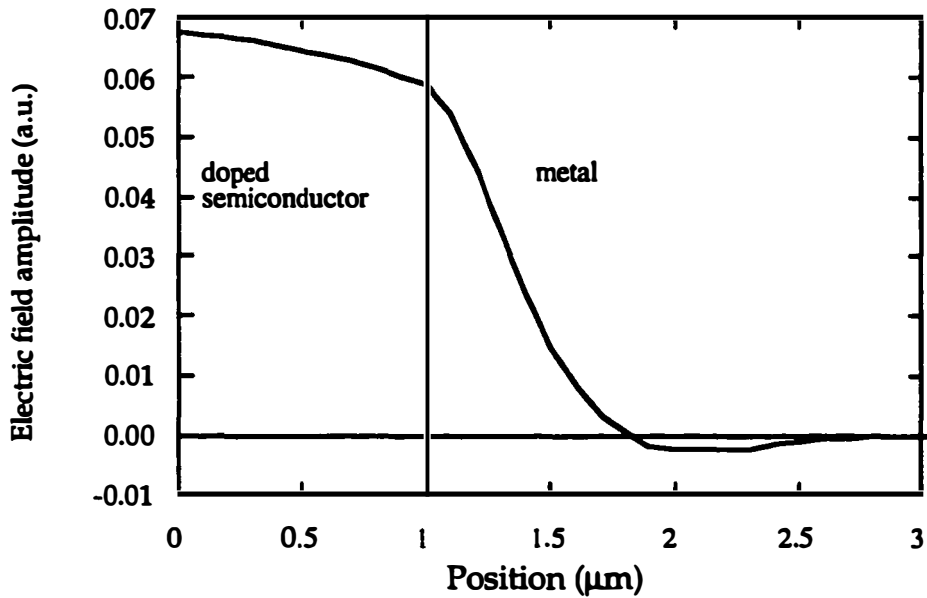


Figure 7. Longitudinal electric field profile vs position in p-doped layer and metal. The figure shows that the field decays primarily in the high conductivity conduct. The kink in the curve occurs at the semiconductor metal interface.

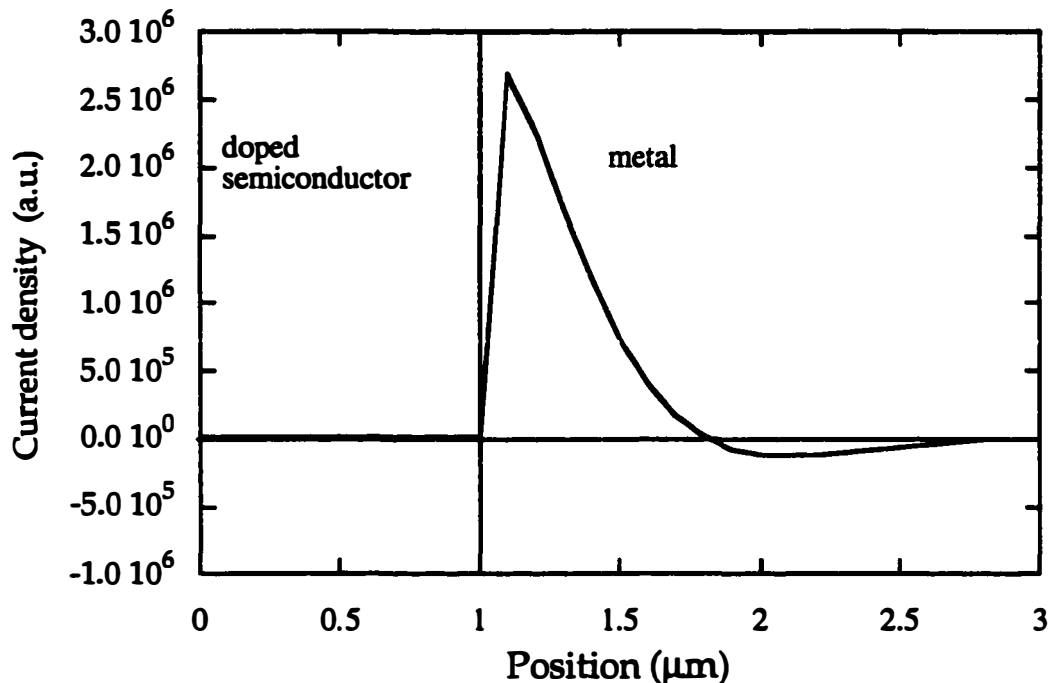


Figure 8. Current density vs position in p-doped layer and metal. The figure shows that virtually all the current is carried in the high conductivity conduct.

conductor (thus the name). At these frequencies this inductance can be comparable to the external inductance, which for simplicity is estimated from the simple parallel plate inductance formula  $L = \mu D / w$ , where  $D$  is the distance between the two plates.

The series impedance calculated above represents contributions to the series impedance from the top conducting layer only, and to find the total series impedance we need to determine the contribution from the lower layer. This is determined in a similar manner, except the calculation is simpler because the n-layer is very thick and virtually all of the longitudinal current is carried in that layer and not in the contact.

This resistivity is  $\frac{1}{\sigma_n \delta_n w_{\text{box}}}$ , where  $\sigma_n$  is the conductivity of the n-doped semiconductor,  $\delta_n$  is the skin depth into the semiconductor, and  $w_{\text{box}}$  is the lateral width over which the current spreads in the semiconductor. This can differ from the top contact width if the top contact is narrow, and needs to be considered in calculating the propagation parameters.

The longitudinal resistance and inductance at 40 GHz for the microstrip laser and the conventional laser are very different. Calculations give resistances of 16 ohms/mm and 135 ohms/mm respectively, and inductances of 112 pH/mm and 262 pH/mm respectively. While the microstrip laser has the same field structure as the conventional doped substrate laser, the numerical values of the circuit elements differ greatly because by placing the ground plane within a skin depth of the active region, the nature of the longitudinal current flow and the spatial extent of the magnetic field change dramatically. The majority of the current flows in the high conductivity gold ground plane instead of the low conductivity doped semiconductor, and the magnetic field terminates several thousand angstroms into the gold layer, rather than several microns into the semiconductor. This has a big effect on both loss and on propagation velocity, the two critical parameters characterizing the microwave propagation.

#### 2.4 Shunt capacitance and shunt conductance

The capacitances in the circuit model comes from a combination of the capacitance above the dielectric and the diode capacitance (incorporated into  $Z_d$ ). These numbers can be estimated from the parallel plate formula for capacitance,  $C =$

$\epsilon w/D$ , for the capacitance per unit length of the laser. The two capacitances in the circuit, of course, require two different values of  $D$ , as the dielectric layer thickness is the value used for  $D$  in calculating the dielectric capacitance, whereas the depletion width (for unbiased lasers) is the value used in calculating the depletion capacitance. Also, the width  $w$  can be different, with the  $w$  of the dielectric capacitance being determined by the metal width, and the  $w$  of the diode capacitance being determined by the width over which the diode built-in voltage exists. For above threshold operation the laser is always strongly forward biased and the diffusion capacitance, rather than the depletion capacitance dominates the active region contribution, particularly at the lower frequencies, below the reciprocal of the carrier lifetime.

The shunt conductance is calculated from several factors, including the series resistance of the p and n layers, the contact resistance, and the diode differential resistance. Under unbiased or reverse biased conditions, the shunt conductance is very low because of the high diode resistance. Above the diode turn on voltage, the conductance increases, with the contact and cladding resistance limiting the conductance rather than the diode resistance which is typically less than an ohm for normal laser dimensions. For the devices used for our calculations and measurements, the dielectric capacitance per unit length was about 2.5 pF/mm. For unbiased operation, the diode contribution to the capacitance was about 2 pF/mm. The unbiased conductance was about 0.01 siemens/mm. The forward biased conductance, dominated by the series resistance, was about 0.1 siemen/mm, with the series resistance of the structure measured being slightly high, about 10 ohms. The forward biased diffusion capacitance varies as is shown in Figure 9, decreasing

as the frequency increased. This particular behavior was determined by fitting the model to measured microwave propagation parameters. At higher frequencies the capacitance shows an inverse square root dependence on frequency, as is expected from theory [8].

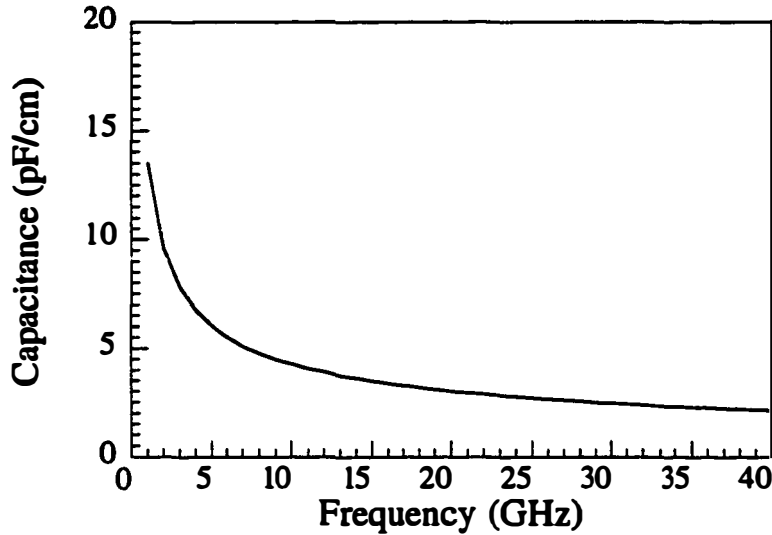


Figure 9. Frequency dependent diffusion capacitance used to model the high frequency semiconductor laser transmission line.

## 2.5 Calculation of propagation properties from distributed circuit model

The complex propagation constant  $\gamma$  is equal to  $\sqrt{ZY}$ , where  $Z = R_s + j\omega L$  is the series impedance associated with the circuit model and  $Y = j\omega C_s + (R_d + Z_d)^{-1}$  is the shunt admittance.  $Z_d$  is the impedance of the active region and is represented as discussed above depending on the bias condition. The characteristic impedance  $\sqrt{Z/Y}$  can also be derived from the model. The spatial dependence of the propagating wave is described by the complex exponential  $\exp(-\gamma z)$ ,  $\gamma = \alpha + j\beta$ ,

with the real part describing the attenuation and the imaginary part describing the phase.

Microwave attenuation and phase velocity for the doped substrate laser are shown in Figures 10 (a) and (b). Microwave experiments were also done on devices matching the parameters specified in the calculations; the experimental results are shown on the plot as the data points. The particular laser measured was a GaAs/InGaAs device emitting at  $0.98 \mu\text{m}$ . The plots show both unbiased and forward biased operation. The striking features apparent in the graphs are (1) the enormous, highly frequency dependent value of loss, as high as 500 dB/cm at 40 GHz for the forward biased case and (2) the slow dispersive phase velocity, which can be less than 10% the vacuum speed of light. These properties are characteristic of a very poor microwave transmission line, in which high frequency signals are localized in the vicinity of the feed point and the regions far away from the feed point are not modulated at all. Because of the frequency dependence observed in the plots, the signal localization is more pronounced as the frequency increases.

The strong frequency dependence of the loss is due to skin effects in the conducting regions. The rise in shunt conductivity associated with the diode turn on accounts for the higher forward biased loss; the wave power is dissipated in ohmic loss caused by current flow through the diode. As discussed earlier, because the skin depths in the semiconductor for the calculated frequency range are significantly less than the thickness of the substrate, the longitudinal currents on the substrate side do not penetrate to the back side metal contact, and are highly attenuated in the doped semiconductor. The room temperature conductivity of  $2 \cdot 10^{18} \text{ cm}^{-3}$  n-doped GaAs is more than 100 times smaller than gold. For the calculation of Figure 10, a gold

conductivity of  $10^5$  S/cm was used [9], and a GaAs conductivity of 640 S/cm was used [9].

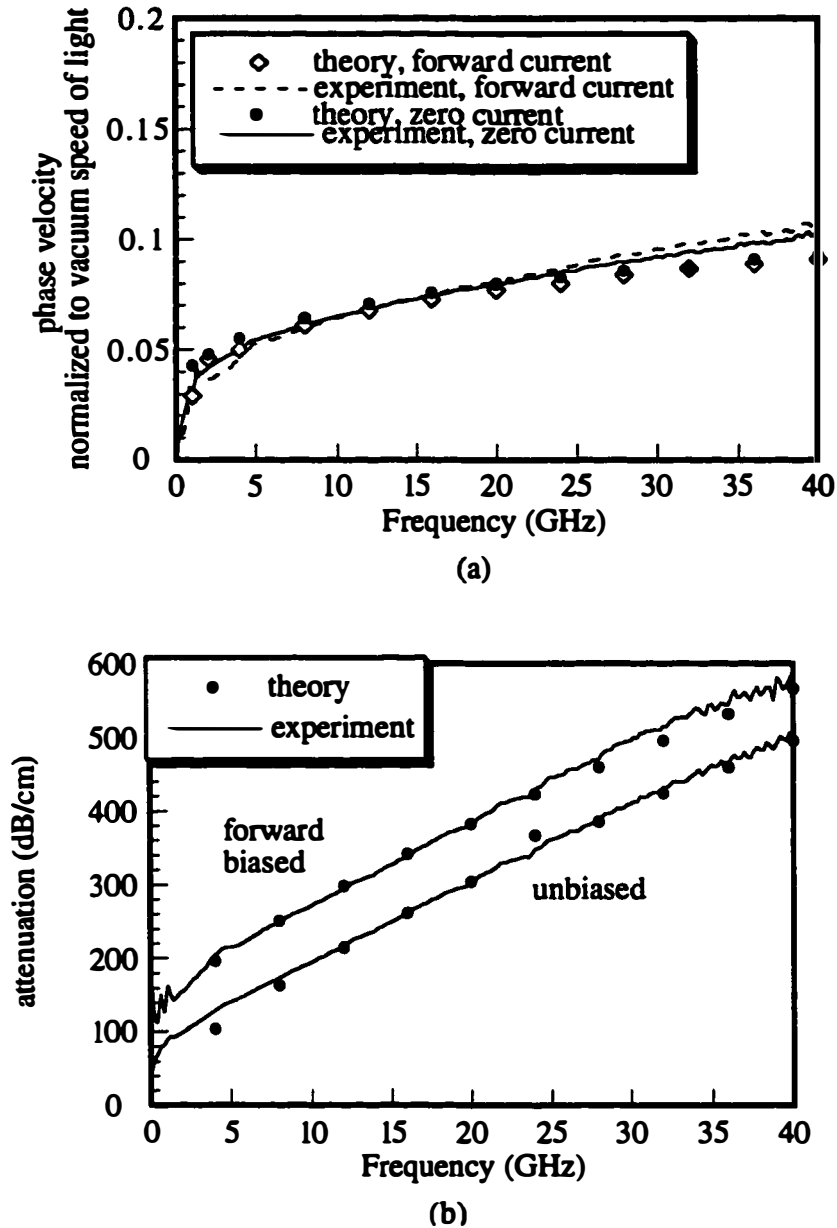


Figure 10. (a) Phase velocity, normalized to the vacuum speed of light, versus frequency, for the conventional GaAs laser. (b) Microwave attenuation versus frequency.

Compared to the substrate, the top p-cladding layer is thin, on the order of  $1\ \mu\text{m}$ , so the longitudinal p-side current penetrates to the gold contact layer where 99% of the current is carried, as is clear from Figure 8. Because the gold conductivity is excellent, the loss from the top contact should be low. However, the skin depth in gold at the frequencies we are interested in is greater than  $5000\ \text{Å}$ , while the p-side contact metal thickness used in the calculation is only  $3500\ \text{Å}$ , which is the thickness of the top contact used in the measured device. The variation of surface resistivity with conductor thickness was included in calculating the loss in Figure 9. Calculations show that as the metal thickness is decreased from  $1\ \mu\text{m}$  to  $0.1\ \mu\text{m}$ , the conductor loss increases by about 50 dB/cm. This loss is significant, but the doped substrate ground plane remains the predominant loss mechanism in the laser.

The structure used in this calculation represents a laser designed to work at moderate frequencies where distributed effects are not important. For very high frequency operation, an improved electrode design is necessary.

The slow wave propagation seen in Figure 10 is as significant as the large attenuation. The propagation velocity determines the device length and the frequency at which distributed effects become important; if the device length is only a negligible fraction of a wavelength, large microwave attenuation is an irrelevant issue because the device is not a distributed structure. Two factors contribute to the slow wave velocity in these structures. First, slow wave propagation is characteristic of any waveguide in which the electric and magnetic fields do not spatially occupy the same region [6, 10, 11]. This is best understood by examining the case of an unbiased or reverse biased p-n junction, where it is clear that the electric field is confined to the depletion region of the structure, whereas the

magnetic field penetrates further into the doped regions. As the wave propagates, energy oscillates back and forth between the electric and magnetic fields. Because the fields do not exist in the same spatial domain, the rate of energy transport is necessarily slowed down, thus slowing down the forward propagation of the wave.

The wave slowing can also be well understood in transmission line terminology as an enhanced capacitance per unit length, because capacitance inversely scales with the spatial extent of the electric field. The electric field occupies a smaller space than the magnetic field, the capacitance is enhanced, and the wave velocity  $v = \frac{1}{\sqrt{LC}}$  is smaller. The wave slowing factor is  $\sqrt{d/D}$ , which can be easily seen by recognizing that the depletion capacitance scales with  $1/d$ , where  $d$  is the depletion width, and the inductance scales with the larger  $D$ , where  $D$  is the spatial extent of the magnetic field. The forward biased phase velocity is also slow because the diffusion capacitance is an excess capacitance greater than that which would be observed in a non-diode transmission line.

The highly lossy nature of the laser transmission line also contributes to wave slowing [7]. As discussed earlier, lossy structures have excess inductance due to the skin effects that adds to the normal transmission line inductance. The functional form of the internal inductance is  $L_i = \frac{l}{2\pi f \sigma \delta} = \sqrt{\frac{\mu}{4\pi f \sigma}}$  where  $\mu$  is the magnetic permeability. The frequency dependence of this inductance also explains the dispersion demonstrated in the phase velocity calculations and measurements. Because the contribution of the internal inductance in the doped substrate laser can increase the total inductance by several times, the wave velocity is further reduced. The reduction factor is roughly equal to the square root of the increase in inductance.

The model predicts the measured loss and phase velocity accurately and reveals the correct dispersion trend (a phase velocity that increases monotonically with frequency). Slight differences between model and experiment can be explained by the fact that the circuit model is only an approximate treatment of the wave propagation. Also, evanescent and higher order modes excited at the feed point that normally decay over a negligible length of standard transmission line may be significant for short structures such as diode lasers. These modes are neglected in the distributed circuit model.

The microstrip design is superior for ultra-high frequency lasers. Figures 11 (a) - (b) show the attenuation and phase velocities for a structure equivalent in all respects to the conventional laser, with the exception that the doped substrate has been replaced by a thick gold ground plane, and that the top contact metallization has been made a thick  $1\mu\text{m}$  to avoid excess skin loss. The performance of the microstrip laser is much improved over the doped substrate laser, and while the propagation properties are still poor, the attenuation is a factor of 5 smaller and the phase velocity is more than a factor of 2 higher. The phase velocity is higher because lower skin losses mean lower inductance. The improved propagation properties imply that the deleterious effects of microwave propagation manifest themselves at significantly higher frequencies in the microstrip laser. As will be pointed out in the next section, those frequencies (for typical laser lengths) are greater than 50 GHz, frequencies where the bandwidth is limited by other, non-related factors having to do with carrier dynamics in quantum wells, or even thermally induced gain reduction.

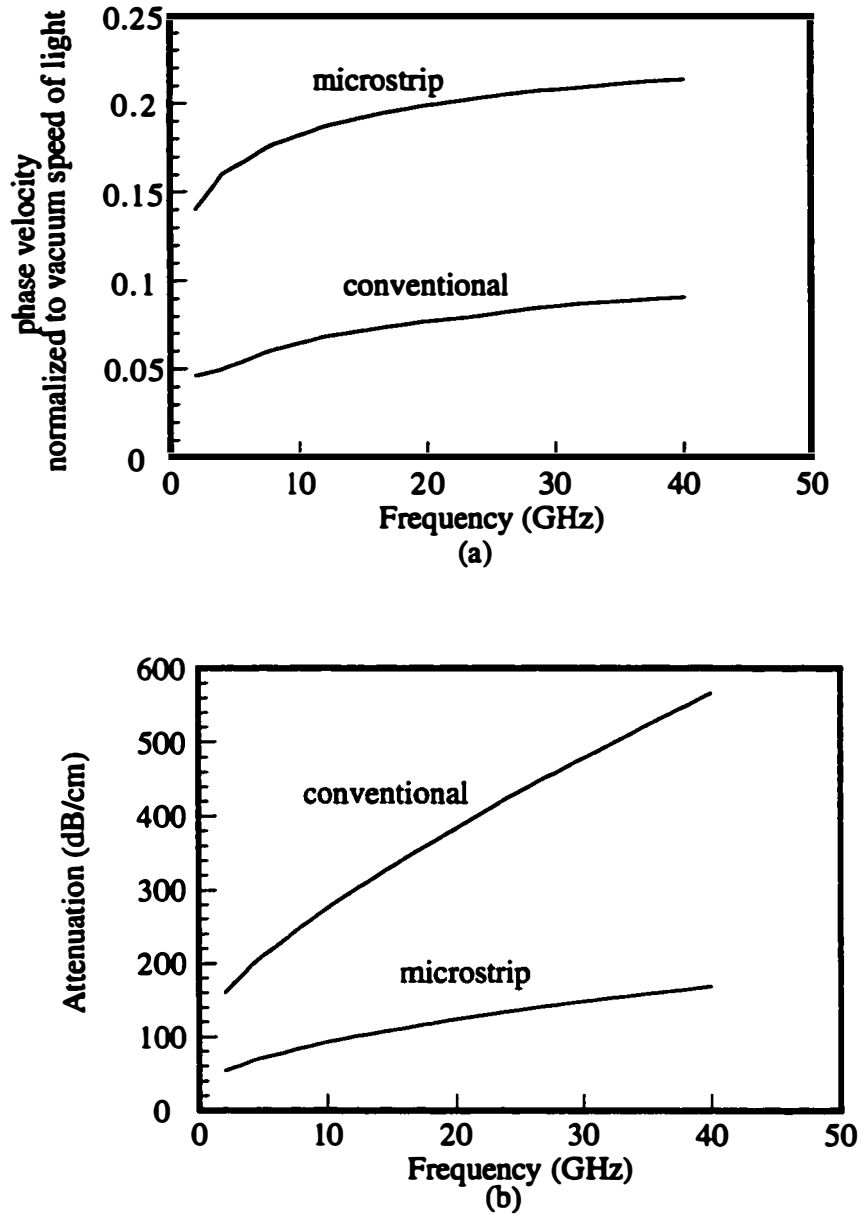


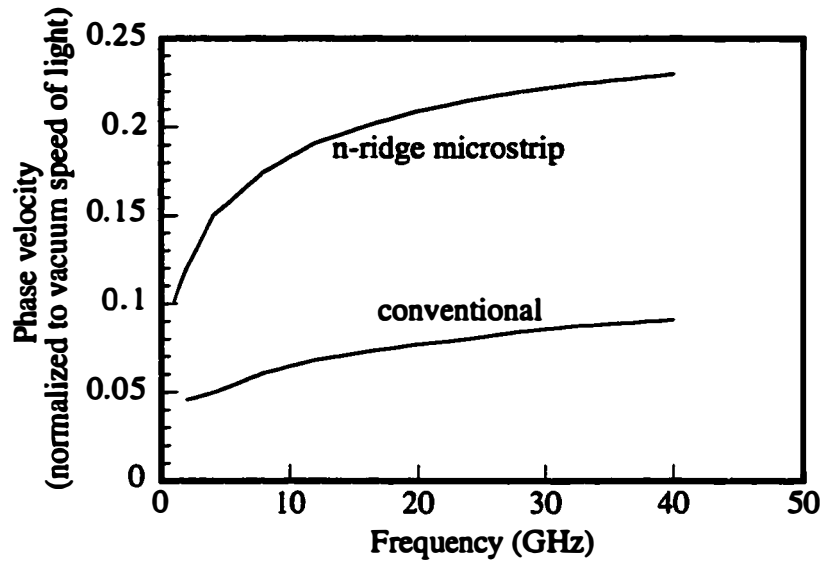
Figure 11. (a) Calculated comparison of microstrip laser and conventional laser phase velocity. (b) Calculated comparison of attenuation.

Figure 12 repeats the calculations of the previous section but for an n-ridge InP microstrip laser rather than a p-ridge microstrip laser. This particular calculation was done to correlate to a real device used for experiments (presented in Chapter 5),

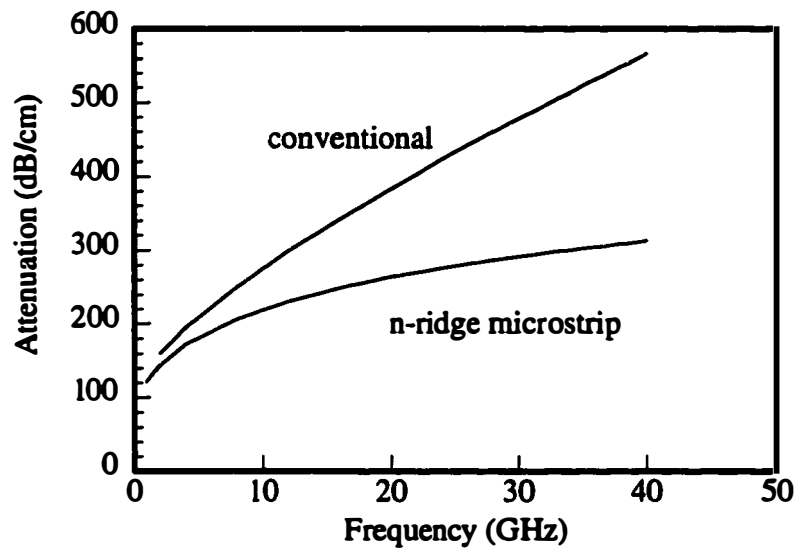
and because as far as microstrip lasers are concerned, the n-ridge microstrip laser has been the focus of this dissertation. Because of the n-ridge, the shunt path conductivity is higher than that of the p-ridge microstrip laser of Figure 11, and the microwave loss is 2-3 times higher. Also the capacitance is slightly different in the InP device, because the ridge height of the InP 1.55  $\mu\text{m}$  lasers is higher, to accommodate for the larger optical mode. Interestingly, this suggests one possible solution to the problem of loss: introduce a sufficiently high ridge resistance so the current uniformly distributes along the length. This is not a good idea however because a high resistance will cause RC rolloff at lower frequencies, and will also cause heating of the active layer and poor DC performance.

## **2.6 Comparison of microstrip laser and coplanar electrode laser**

Figure 13 shows schematic diagrams of two high frequency lasers with coplanar or quasi - coplanar electrodes. Figure 13 (a) has been used for fabricating ultrahigh frequency lasers, and bandwidths 40 GHz and greater have been reported for this structure. The ground contacts are made by evaporating metal on top of dummy ridges adjacent to the active ridge and shorting the metal on the dummy ridges to the n-contact (the ridges are p-doped), as can be seen in the figure. The device is probed with coplanar high frequency probes. A similar structure, shown in Figure 13 (b), is one in which the ground metallization directly contacts the n-region and dummy ridges are not used. Although the contacts are not perfectly coplanar in this case, the availability of excellent high frequency probes that permit some degree of non-coplanarity makes the structure practical for high speed testing.



(a)



(b)

Figure 12. (a) Calculated comparison of n-ridge InP microstrip laser and conventional InP laser phase velocity. (b) Calculated comparison of attenuation.

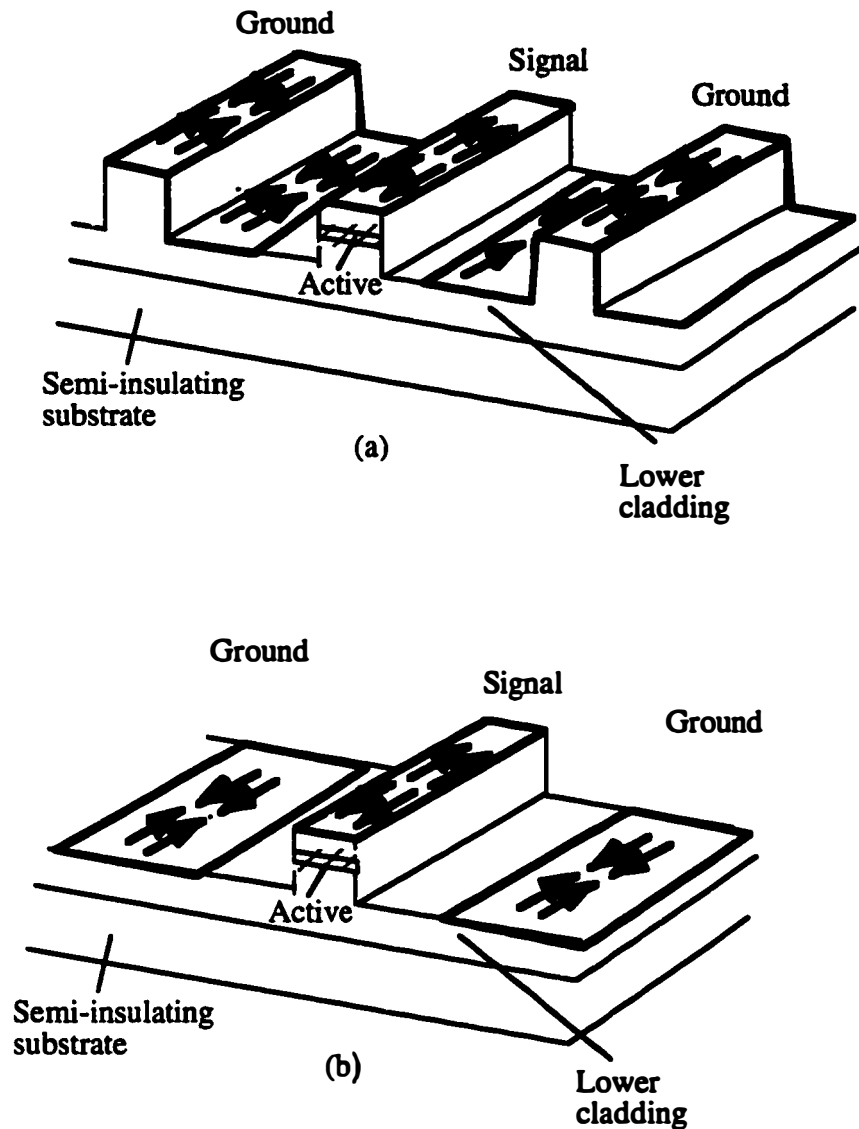


Figure 13. (a) True coplanar ground - signal - ground high frequency laser. (b) Quasi coplanar ground - signal ground high frequency laser.

The coplanar structures in Figure 13 address the same microwave problems that the microstrip laser addresses. The high frequency longitudinal currents flow in thick metal rather than in doped semiconductor, and one would expect the propagation properties to be superior to that of the conventional doped substrate

laser. The measured frequency and bias dependence of the elements making up the equivalent circuit of Figure 4 have been published for lasers like that of Figure 13 (a) [2, 12]. Plugging this data into the propagation model, the phase velocity and attenuation properties of the coplanar laser can be calculated and compared with the microstrip laser. Figure 14 shows this comparison. The calculations show that this coplanar electrode laser is a better structure than the doped substrate laser with respect to both phase velocity and attenuation, but is not as good as the microstrip laser. The loss is about 30% higher in the coplanar laser, and the phase velocity is about 50% lower. The higher loss may be due to lateral spreading resistance between the signal and ground lines that is present in the coplanar, but not the microstrip geometry. Microwave currents flow in the spreading region and contribute to excess loss. The higher loss also accounts in part for the reduced phase velocity of the coplanar laser.

### **2.7 Effect of microwave propagation on dynamics and modulation response**

The interesting and critical performance criterion for a semiconductor laser is always optical response. In understanding this for the case of microwave propagation effects, the first step is analysis of the high frequency current injection. This is what is done in the lumped element case also. In the simple RC parasitic model of the laser, current partitions between the resistive and capacitive paths; current through the resistive path modulates the active region and the photon density, and current through the capacitor is useless. At higher frequencies, more current is capacitive, less is resistive, and the optical modulation rolls off.

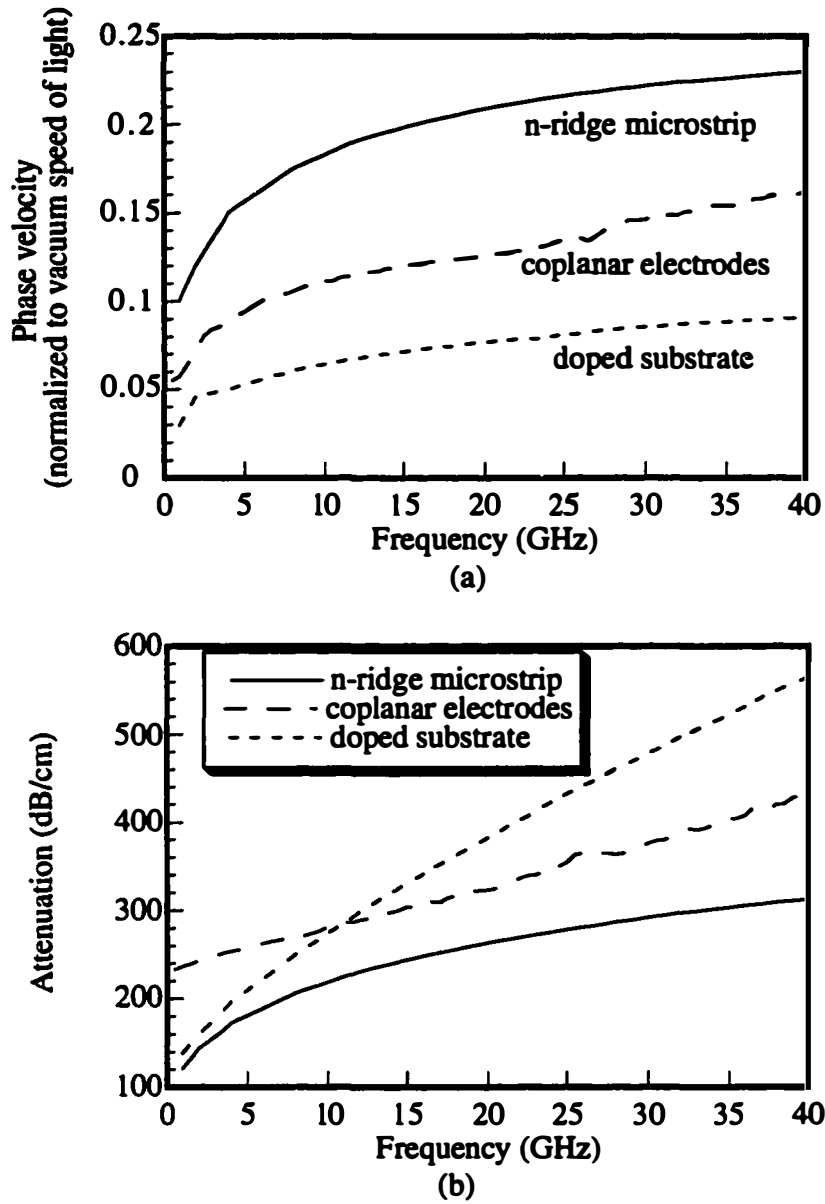


Figure 14. (a) Phase velocity comparison for coplanar, microstrip, and conventional doped substrate lasers. (b) Microwave attenuation comparison for the three lasers.

## 2.7 Effect of microwave propagation on dynamics and modulation response 70

Similarly, for distributed microwave effects, the current injection changes as the frequency changes, due to the frequency dependence of the loss and the microwave wavelength. The large loss has the most profound effect. The changing current injection clearly also influences the optical response.

The large loss causes a large nonuniformity in the high frequency current injection to the active region. Further, because the loss is frequency dependent, the nonuniformity becomes more severe as the frequency rises, and a smaller fraction of the total laser length is pumped. This is illustrated in Figure 15, where the spatial distribution of the current, extracted from measured propagation for the doped substrate laser, is shown for frequencies of 20 and 40 GHz. The curves assume the feed point of the laser is at the center of the laser stripe, and waves propagate symmetrically outward from the center towards the edges. The high attenuation coefficient gives a sharp downward slope to the outward propagating waves and produces the kink at  $l=0$  seen in the curves. Using standard transmission line theory, the magnitude and phase of the launched current wave at the input of the laser can be expressed as  $i(f) = \frac{2\bar{v}_i}{Z_0} \frac{1}{1 + Z_1(f)/Z_0}$  where  $\bar{v}_i$  is an ac voltage drive source,  $Z_0$  is the source impedance, and  $Z_l$  is the input impedance of the laser.  $Z_0$  is  $50 \Omega$  for the situation of practical interest. The launched current wave is of the form  $i(f)e^{-\gamma l}$  where  $i(f)$  is defined as above and  $\gamma$  is the complex propagation constant; the launched voltage wave is represented as  $v(f)$ , where  $v(f) = i(f)Z_1(f)$ . The injected current per unit length is calculated by multiplying the voltage wave propagating along the transmission line by the shunt conductance per unit length (representing current into the active region)  $1/R_s$ . This analysis reveals a significant rolloff in the injected current with frequency. Figure 16 shows the square

magnitude of the total integrated current, normalized to DC, versus frequency, for 3 different device lengths. The 3 dB rolloff frequency occurs at approximately 25 GHz for the 300  $\mu\text{m}$  long device. In these plots, the device is fed at the center of the laser stripe. This is the optimal feeding condition since waves can propagate out in both directions from the center and maximally pump the device. An end fed device has a lower rolloff frequency because only a single forward wave can propagate and therefore the fraction of the device that is pumped is smaller. The distributed effects cause severe problems at high frequency and laser structures that minimize the microwave attenuation and phase velocity slowing must be used for high frequency operation.

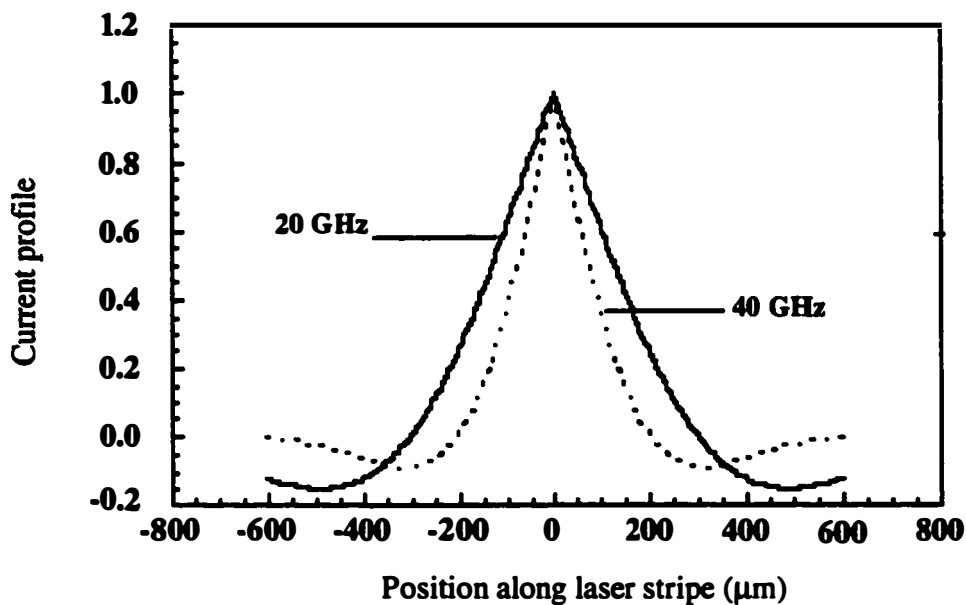


Figure 15. Injected current profile for a center fed conventional laser on a doped substrate for frequencies of 20 and 40 GHz.

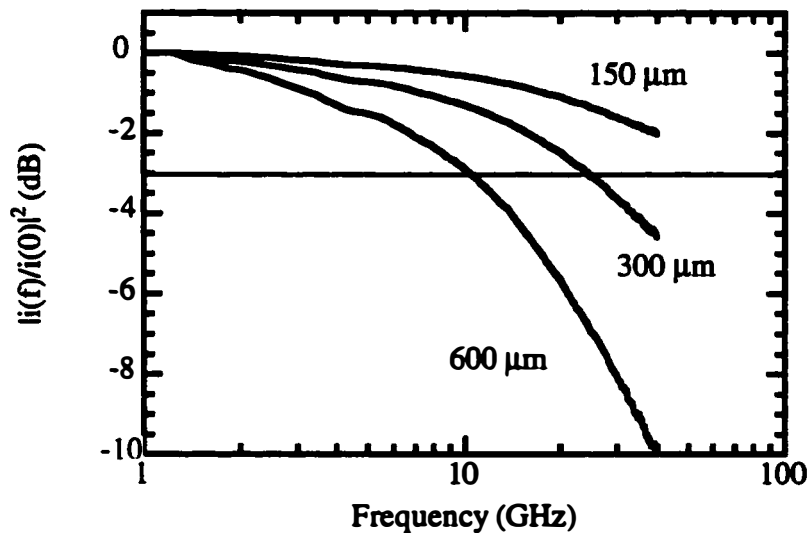


Figure 16. Current rolloff in conventional doped substrate laser due to distributed microwave effects for several different laser lengths.

In contrast to the doped substrate laser, Figure 17 shows the profile of the high frequency current injection for the n-ridge microstrip laser calculated in Figure 12. The qualitative behavior remains the same, but for the same length device, a much greater fraction of the laser length is modulated; because of this, the difference in the area under the curve, representing the total current, between the 20 and the 40 GHz result is significantly smaller in the case of the InP microstrip laser than it is in the doped substrate device. Converting this to a frequency rolloff, the equivalent 3 dB rolloff does not occur until frequencies above 50 GHz are reached.

The rolloffs of the microstrip laser, the conventional doped substrate laser, and the coplanar electrode laser are compared in Figure 18, for a 300  $\mu\text{m}$  long cavity length, center-fed device. As expected the doped substrate laser shows the lowest rolloff frequency. The -3 dB rolloff frequencies of the microstrip laser and the coplanar electrode laser are above 50 GHz, with the microstrip laser showing the

best performance. With regard to the design of high speed lasers, it should be pointed out that coplanar electrode structures fabricated on doped substrates (as opposed to semiinsulating) will still show better performance than the conventional laser on a doped substrate, as long as the primary microwave mode remains coplanar, so that the majority of the high frequency ground current flows in metal. Keeping the ground electrodes as close to the signal line as possible helps to ensure this.

To further show the effect on bandwidth, frequency response curves for the three different high frequency lasers are compared in Figure 19 to a case where distributed microwave effects are not present. The intrinsic -3 dB bandwidth is about 37 GHz; the parameters used in the calculation were taken from high frequency devices reported in the literature [13]. The -3 dB bandwidths of the doped substrate laser, the coplanar electrode laser, and the microstrip laser are about 31 GHz, 35 GHz, and 36 GHz respectively.

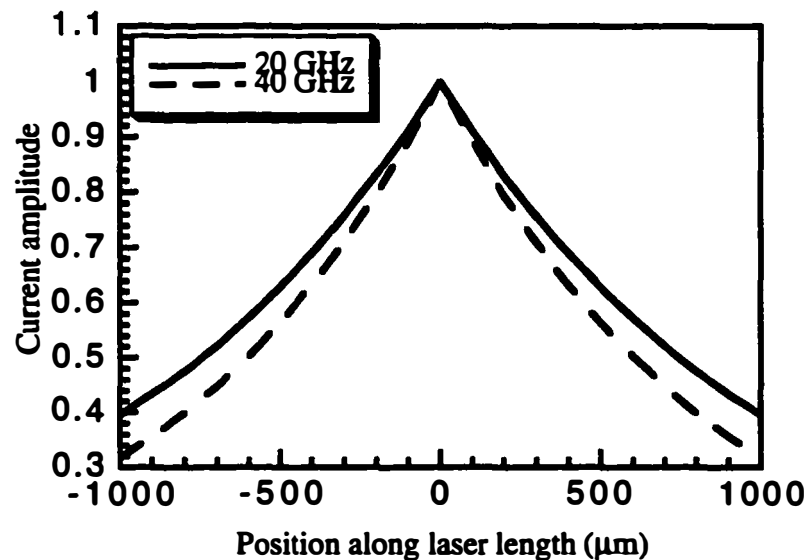


Figure 17. Current profile along the laser length for a center fed microstrip laser. The current profiles at 20 and 40 GHz are shown.

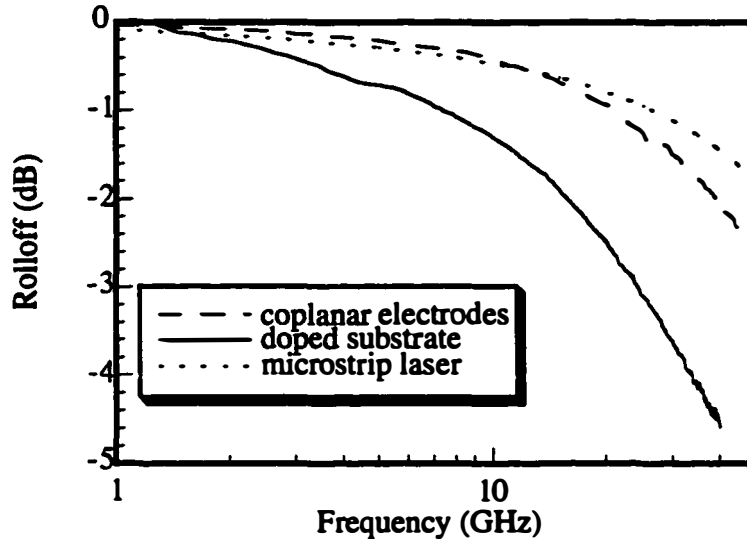


Figure 18. Comparison of the distributed microwave rolloff for three different high frequency lasers.

The question of reflections at the open circuited end of the laser comes up. For highly lossy devices such as the doped substrate laser, this issue is not important, because the large loss attenuates the signal so much, no appreciable wave exists at the laser ends. For the low loss, higher phase velocity structures such as the microstrip laser and the coplanar electrode laser, the likelihood of reflections from the ends is higher. Essentially a reflection would cause a phase effect, and some resonant peaks and dips in the optical response at the very high frequencies where the effects exist. Still, it must be kept in mind that even the better structures are high loss and the signals do not bounce back and forth in the cavity multiple times. In other words, the microwave loss remains the dominant effect.

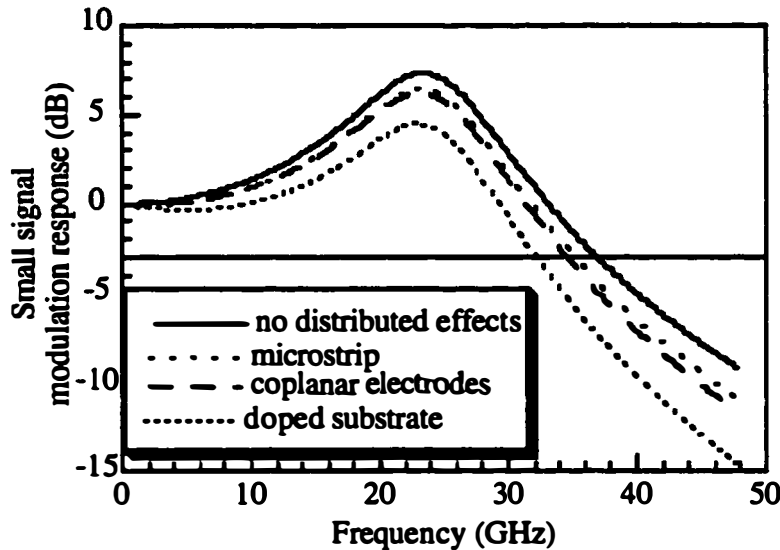


Figure 19. Calculated small signal frequency response curves for three different laser structures. The microstrip laser and the coplanar electrode laser show much superior performance to the conventional doped substrate laser.

There has been some discussion in the literature regarding the effect of the nonuniform current injection on the small signal modulation response. An argument has been made that the distributed effects only manifest themselves significantly in the small signal modulation response for lasers that are driven by a low impedance voltage source. The effects are claimed to be minimal when driven by  $50 \Omega$  transmission line source, as is generally the case in practice [14]. The logic of the argument is that the laser impedance is small (on the order of several ohms) relative to the source impedance, and that the  $50 \Omega$  drive therefore acts as a current source which uniquely determines the current injection to the laser through the equation  $i(f) = \frac{2\tilde{v}_i}{Z_0} \frac{1}{1 + Z_l(f)/Z_0}$  [14]. Wu argues that since  $Z_l$  is low compared to  $50 \Omega$  over the entire frequency range, the total injected current changes only slightly as a

## 2.7 Effect of microwave propagation on dynamics and modulation response 76

function of frequency. The spatial distribution of the current, however, is still highly nonuniform; in this analysis, the peak current at  $l=0$  in Figure 12 is higher for the 40 GHz case than it is for 20 GHz, and thus the total current in each case is nearly identical. Some rolloff is calculated in this model, which is attributed to the frequency dependent rise in the longitudinal resistance  $R_l$ , and the effect this has on  $Z_l$ . but a larger rolloff in the frequency response is calculated when the device is driven with a voltage source (where  $Z_0$  is small compared to  $Z_l$ ) because the frequency dependence of  $Z_l$  has a much more significant effect in this case. This analysis is not incorrect but oversimplifies the complexity of the problem by reducing it to a lumped element analysis, albeit one that incorporates a longitudinal resistance in the calculation. At high enough frequencies this breaks down and the full distributed treatment presented in this chapter must be used [1, 15]. In this treatment the magnitude and the phase of the current wave injected at the input is calculated from impedance arguments, and the total current is determined by integrating along the device length. Other limits also exist that are directly related to the distributed effects and the spatial confinement of the current. For example, frequency dependent variations in the feed point to facet optical path length of the *modulated* photons could affect the bandwidth through the optical loss. The highly lossy laser transmission line is not truly a linear system, and coupling between different elements of the line could introduce other frequency dependent effects that translate into bandwidth limits as well [3].

**2.8 Other dynamic effects related to microwave propagation**

Several other interesting device properties and possibilities related to the microwave propagation effects have been reported in the literature. These include a monolithic mode locked semiconductor laser using a single contact. Mode locking occurs in a laser when a small portion of the laser cavity is modulated in phase with the round trip time of the photons. The additional in-phase kick the photons get on each round trip enhances the modulation response at the round trip frequency. Typically, this has required a two contact multi-segment monolithic device, in which one long section is DC biased, and a shorter section is modulated, or an external cavity device in which one facet of the semiconductor laser is anti-reflection coated and a long cavity is made with an external mirror. The inherent localization of the current caused by the distributed effects allows for mode locking with a simple single contact, and resonant enhancement as high as 30 dB at 40 GHz has been reported [4]. Another report studying gain switched pulses showed that the RF spectrum of the generated pulses strongly depended on feed point location, with the high frequency components found to be severely attenuated for a feed placed far from the facet. A center feed, providing the most uniform current injection, gave the best results [5].

**2.9 Optical - microwave velocity mismatch effects**

The effects of phase walkoff between the optical wave and the microwave is another interesting subject. The walkoff effects only become important when the

modulation frequency approaches the cavity round trip frequency. This can best be understood by Figure 20. For a typical laser, the cavity round trip time is several picoseconds, corresponding to frequencies greater than 100 GHz. Although the microwave current is highly nonuniform, its spatial profile does not significantly change in time until the optical wave has made several round trips around the cavity. Therefore an average optical power density, or photon density inside the cavity can be assumed, and the distributed microwave effects can be treated as an independent problem. One report claims this is reasonable as long as the modulation frequency is less than half the round trip frequency [14].

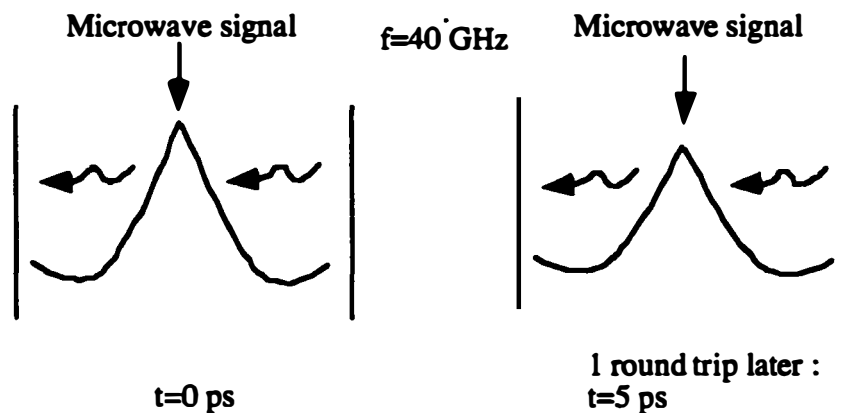


Figure 20. Microwave signal at 40 GHz inside a laser cavity at the beginning and end of one round trip. At 40 GHz the phase of the microwave signal does not change that much over one round trip.

## 2.10 Summary and conclusions

This chapter has demonstrated that state of the art high speed semiconductor lasers behave as distributed electrical elements at high frequency, and that the distributed effects impact dynamic performance in both the small and large signal domain. The

laser is a lossy, slow wave transmission line and can be accurately modeled with a distributed equivalent circuit that takes into account frequency dependent skin losses and phase effects, as well as including the usual resistances and capacitances of the lumped element model. The high loss and slow wave velocity result in a localization of the high frequency current. While the device is efficiently modulated near the feed point, points far from the feed are not modulated at all.

The equivalent circuit incorporates a longitudinal resistance to model skin losses, and a longitudinal inductance to account for the magnetic field of the propagating wave. These elements, along with the parasitic capacitance, the series resistance, and the active region impedance accurately model the data for different bias conditions and different frequencies.

Conventional lasers on doped substrates are the poorest of all semiconductor laser transmission lines, since the doped substrate behaves as a highly lossy and frequency dependent ground plane, causing large attenuation of the microwave signals. The attenuation is as high as 600 dB/cm at high frequency. In the microstrip laser the ground plane is a thick metal layer, and the propagation properties are much improved. The loss is lower by at least a factor of 2, and the phase velocity is higher. The significance of this is that the frequencies at which the distributed effects degrade the dynamic performance are much higher in the microstrip laser. Coplanar electrode lasers show superior propagation properties relative to the doped substrate lasers, although the microstrip laser shows the best performance. For typical device lengths, the -3 dB rolloff frequencies of the doped substrate lasers are in the vicinity of 30 GHz, whereas the coplanar structure rolls

off around 50 GHz. The microstrip laser limits calculated here are beyond even that, around 60 GHz.

Excellent high frequency lasers first must be excellent DC lasers. The next chapter examines the DC performance of the microstrip laser in terms of threshold currents, efficiencies, and thermal properties, and presents design guidelines for making an excellent DC microstrip laser.

## References

- [1] D. A. Tauber, R. Spickermann, R. Nagarajan, T. Reynolds, J. A. L. Holmes, and J. E. Bowers, "Inherent bandwidth limits in semiconductor lasers due to distributed microwave effects," *Appl. Phys. Lett.*, vol. 64, pp. 1610-1612, 1994.
- [2] S. Weisser, I. Esquivias, P. J. Tasker, J. D. Ralston, and J. Rosenzweig, "Impedance, modulation response, and equivalent circuit of ultra-high-speed In<sub>0.35</sub>Ga<sub>0.65</sub>As/GaAs MQW lasers with p-doping," *IEEE Photon. Tech. Lett.*, vol. 6, pp. 782-784, 1994.
- [3] L. F. Eastman, School of Engineering, Cornell University, Ithaca, New York, personal communications, 1996.
- [4] D. M. Cutrer, J. B. Georges, T. C. Wu, B. Wu, and K. Y. Lau, "Resonant modulation of *single* contact monolithic semiconductor lasers at millimeter wave frequencies," *Appl. Phys. Lett.*, vol. 66, pp. 2153-2155, 1995.
- [5] K. C. Sum and N. J. Gomes, "Harmonic generation limitations in gain-switched semiconductor lasers due to distributed microwave effects," *Applied Physics Letters*, vol. 71, pp. 1154-5, 1997.
- [6] D. Jäger, "Slow-wave propagation along variable Schottky-contact microstrip line (SCML)," *IEEE Trans. Microwave Theory Tech.*, vol. 24, pp. 566-573, 1976.
- [7] S. Ramo, J. Whinnery, and T. V. Duzer, *Fields and Waves in Communication Electronics*, 2 ed. New York: John Wiley, 1984.
- [8] S. M. Sze, *Physics of Semiconductor Devices*, 2 ed. New York: John Wiley & Sons, 1981.

- [9] G. L. E. Turner, "CRC Handbook Of Chemistry and Physics - a Ready-Reference Book Of Chemical and Physical Data, 70th Edition - Weast,Rc, Lide,Dr," *Annals Of Science*, vol. 48, pp. 496-497, 1991.
- [10] D. Jäger, R. Kremer, and A. Stohr, "Travelling-wave optoelectronic devices for microwave applications," presented at *IEEE Int. Microwave Symposium*, Orlando, Fl., 1995.
- [11] H. Hasegawa, M. Furukawa, and H. Yanai, "Properties of microstrip line on Si-SiO<sub>2</sub> system," *IEEE Trans. Microwave Theory Tech*, vol. 19, pp. 869-881, 1971.
- [12] S. Weisser, P. J. Tasker, I. Esquivias, J. D. Ralston, and J. Rosenzweig, "Impedance modulation response and equivalent circuit of ultra-high-speed InGaAs/GaAs MQW lasers," presented at *Int. Electron Devices Meeting*, Washington D.C., 1993.
- [13] J. D. Ralston, S. Weisser, I. Esquivias, E. C. Larkins, J. Rosenzweig, P. J. Tasker, and J. Fleissner, "Control of differential gain, nonlinear gain and damping factor for high-speed application of GaAs-based MQW lasers," *IEEE J. Quantum Electron*, vol. 29, pp. 1648-1658, 1993.
- [14] B. Wu, J. B. Georges, D. M. Cutrer, and K. Y. Lau, " On distributed microwave effects in semiconductor lasers and their practical implications," *Appl. Phys. Lett*, vol. 67, pp. 467-469, 1995.
- [15] S. Weisser, I. Esquivias, P. J. Tasker, J. D. Ralston, B. Romero, and J. Rosenzweig, "Impedance characteristics of quantum well lasers," *IEEE Photon. Tech. Lett.*, vol. 6, pp. 782-784, 1994.



## Chapter 3

### **DC analysis of the microstrip laser: Current distribution and heat distribution**

The microstrip laser is a novel semiconductor laser. As with any semiconductor laser, it is critical to define and understand the key properties that characterize its performance. Good DC performance is the first thing that needs to be addressed in making a good laser, be it a high power laser, a high speed laser or both. The important properties include threshold current, efficiency, leakage currents, spatial current distribution and voltage distribution, electrical resistance, and thermal resistance. This chapter investigates and explains these properties in the context of the microstrip laser and clarifies the ways in which the microstrip laser is a better structure than a conventional laser. Problematic aspects of the microstrip laser are also addressed, and their solutions are presented. Significant differences are found to exist in the microstrip laser for *all* the DC performance criteria listed above. For example, the microstrip laser usually has larger lateral leakage current than a conventional laser, and this leads to design modifications intended to ensure good threshold and efficiency performance. Second, the electrical resistance of the microstrip laser is lower than a conventional laser. This is advantageous for better thermal performance as well as improved high speed performance. Third, the high thermal conductivity of the gold bonded layer close to the active area contributes to a reduced thermal resistance that is advantageous for high power operation.

### 3.1 Background

As discussed in the introduction, the microstrip laser fabrication process results in a flipping of the epitaxial layers on the substrate - a wafer grown p-up becomes p-down. In the InGaAsP/InP system, the epitaxial inversion is significant because of the inherent difficulties in growing an n-up epi layer. The epi inversion introduces several new device properties, some of which are desirable and some of which are not, that must be understood to fabricate good lasers. Further, devices normally difficult to make by conventional growth and fabrication procedures can be more simply made with the gold-bonding process used for the microstrip laser.

To demonstrate the problems inherent in growing a p-down structure, a SIMS profile of a p-down InGaAsP/InP laser wafer intended to have an undoped active region is shown in Figure 1. The plot shows that the p-dopant zinc (Zn) has diffused into the active region and doped it to about  $3 \times 10^{19} \text{ cm}^{-3}$ . Broad area lasers fabricated from this wafer had threshold current densities above  $3 \text{ kA/cm}^2$ , most of it from the optical loss caused by the high doping concentration. The problem is that Zn is a very mobile element, and at growth temperatures of 650 - 700 °C, it easily diffuses into the active region from the bottom p-layer. While some groups have successfully fabricated p-down InP lasers [1], reports of these devices are minimal, and it is not certain that the active regions can be grown to specification, or reliably and reproducibly.

Conventional InP lasers are therefore constrained, for most practical purposes, to be p-ridge devices. There is a disadvantage associated with this: a p-ridge has a higher electrical resistance than an n-ridge [2], that limits the high speed performance through the RC time constant, and limits the high power performance

through an increased thermal resistance caused by higher joule heating in the ridge [3]. Since the epi-layer flipping is inherent in the microstrip laser fabrication, the microstrip laser eliminates all these p-ridge related performance constraints.

N-ridge lasers have a different set of problems. Because the electron mobility is high, electrons injected from the n-ridge into the SCH and active region spread laterally to a much greater extent than do holes from a p-ridge. This lateral leakage causes very high thresholds for narrow ridge devices, rendering the lasers useless. The SCH and active region can be etched away to minimize this problem, and a low surface recombination velocity in InGaAsP (about  $10^4$  cm/s, an order of magnitude smaller than in GaAs) means that the exposed sidewalls do not significantly negate the improvements due to etching. Some disadvantages still exist. The lifetime may be reduced because of defect generation at the exposed sidewalls, the laser tends to multimode operation at lower biases because of the highly index guided mode, and there is excess optical loss at the sidewalls. Heat removal from the active region is slightly less efficient, because the active region is surrounded by air or dielectric rather than semiconductor. This last problem is not that severe, however, because the thermal conductivity of InGaAsP is quite low to begin with and air or dielectric is not vastly worse [4].

Regrowth around the active region would eliminate these problems. A microstrip laser process in which regrowth is performed first, and bonding and inversion follows would allow for this. A thin film bonding process has been reported in the literature and indicates that such a design is feasible [5]. In the process we developed, the wafer bonding is the initial step and

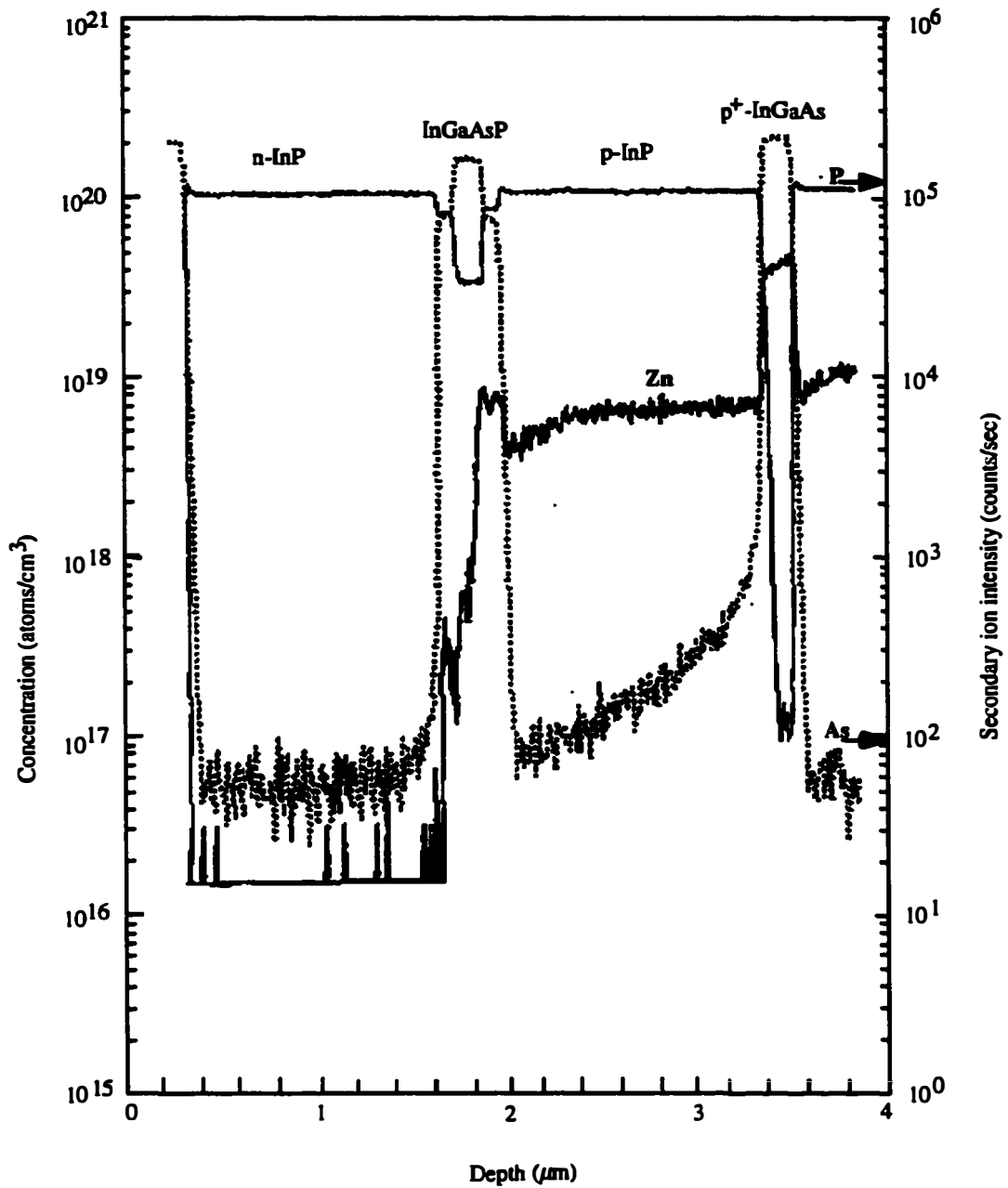


Figure 1. SIMS profile of a p-down grown laser structure. The p-dopant, zinc, diffuses into the InGaAsP active region at a concentration near  $10^{19} \text{ cm}^{-3}$ .

regrowth because the gold bonded layer diffuses significantly at temperatures above 400 °C and regrowth is performed at around 600 °C; the diffused gold can penetrate deep into the lower cladding and cause very high optical loss, or even worse, can short out the diode completely. Also, the thin epi film (~3 μm thick) above the gold bubbles and bows due to the movement of gold beneath it, damaging the smoothness and integrity of the film. Since a continuous smooth layer is required for good lasers, deviation from an excellent surface morphology is a serious obstacle. In the worst case the bond is destroyed because so much gold diffuses out, leaving behind large voids.

Schematics of four different laser structures are shown in Figure 2: the conventional p-ridge laser, the conventional n-ridge laser, the microstrip n-ridge laser and the microstrip p-ridge laser. In the analysis that follows, the electrical and optical properties of these lasers are calculated. The calculations graphically show the spatial distribution of current in the lasers and also generate L-I and I-V curves. The current distribution plots help explain the high thresholds measured in n-ridge devices (with unetched SCH/active region) by showing the extent of lateral leakage current. The I-V calculations quantify some of the differences in resistance among the structures. The calculations were done with that ATLAS laser simulation program [6]. Two drawbacks of the ATLAS simulator are that it does not incorporate a quantum well gain model and it calculates only the fundamental laser mode. Because of this, the calculations are restricted to ridges 5 μm wide and smaller. The laser bar length used in the simulation is 50 μm; the short length is used to minimize computation time.

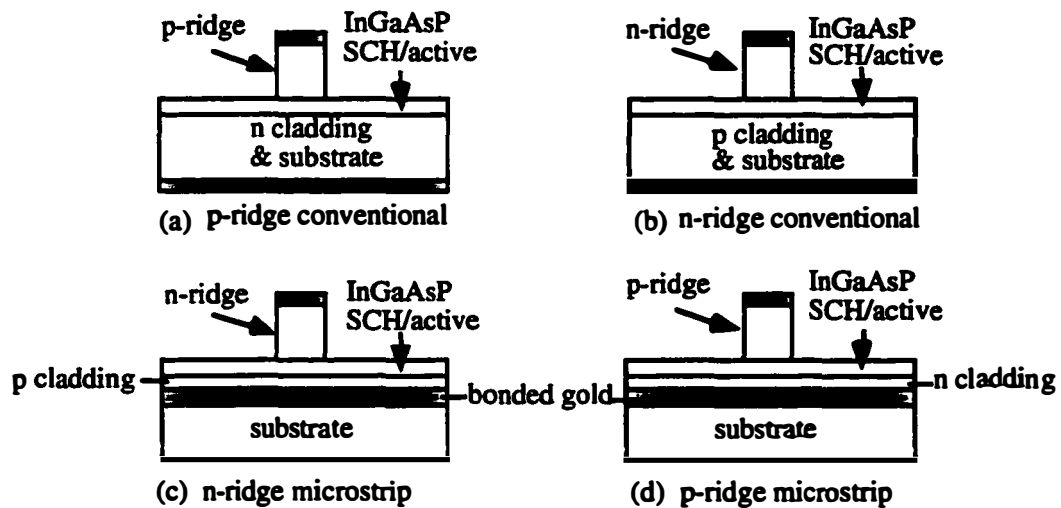


Figure 2. Four different laser structures used in simulations of electrical and optical performance.

While the calculations are not exact models of the fabricated lasers because they do not incorporate a quantum well gain model (the ATLAS program does not have this feature) nor do they account for all the optical loss in the structure, they are sufficient for explaining the key properties in which we are interested, and for quantifying and understanding experimentally observed trends in threshold and resistance. They are not intended to be used as an exact tool for predicting laser performance.

### 3.2 Lateral current spreading

A very significant way the mobility difference between electrons and holes manifests itself in laser operation is in the spatial distribution of the current [7-9]. More specifically, the lateral leakage current in an n-ridge and a p-ridge laser is different. This causes significant differences in the threshold currents of otherwise identically processed devices. The ridge is typically fabricated by etching through

the InGaAs cap and the InP cladding layers, and stopping at the InGaAsP SCH. As mentioned earlier, advantages to stopping the etch at the SCH include longer device lifetime, better single mode operation, and less optical loss. A disadvantage is poor current confinement, since carriers injected into a wide SCH region diffuse laterally in the SCH and also in the active region. The recombination region is solely determined by this lateral diffusion since movement of carriers in the bottom cladding is not laterally restricted - lower cladding carriers are present and available everywhere for recombination. Implantation is a possible way of addressing the current spreading problem without etching through the active region, and has been reported in several publications [10].

The ridge also defines the spatial extent of the optical mode; any recombination outside the boundary of the optical mode does not contribute to modal gain. This recombination current is a significant fraction of the total threshold current if the leakage path is wide. In p-ridge lasers, the effect is not that large, since the hole mobility is small, less than  $100 \text{ cm}^2/\text{volt-sec}$  [11], and the hole diffusion length is only about  $0.3 \mu\text{m}$  in InGaAsP. In n-ridge lasers, however, the effect is very large, and the leakage current makes up the majority of the threshold current for narrow ridge devices. The electron mobility is on the order of  $5000 \text{ cm}^2/\text{volt-sec}$  [12] and the diffusion length is about  $10 \mu\text{m}$ .

Figure 3 shows the quantum well band diagram used in the simulations. The epi design shown in the figure is representative of the laser material that was used for device fabrication in this work. Figure 4 compares the current spreading in the SCH and active region for injection from a  $2 \mu\text{m}$  p-ridge and a  $2 \mu\text{m}$  n-ridge. Microstrip lasers were not simulated because with respect to current spreading, an n

(p) -ridge microstrip laser is no different from a conventional n (p) ridge laser. Each bounded contour in the plot represents 1/8 of the total injection current. A close look at the figure shows that 50% of the total current in the p-ridge is confined to a width of about  $2.5 \mu\text{m}$  at the bottom of the active region; 75% of the total is confined to a width of  $4.75 \mu\text{m}$ . In the n-ridge device, the same fractions of current spans widths of  $3.7 \mu\text{m}$  and  $12 \mu\text{m}$  respectively.

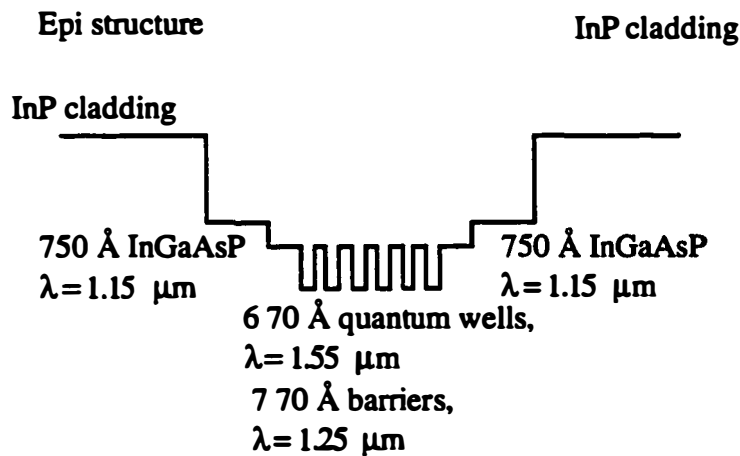
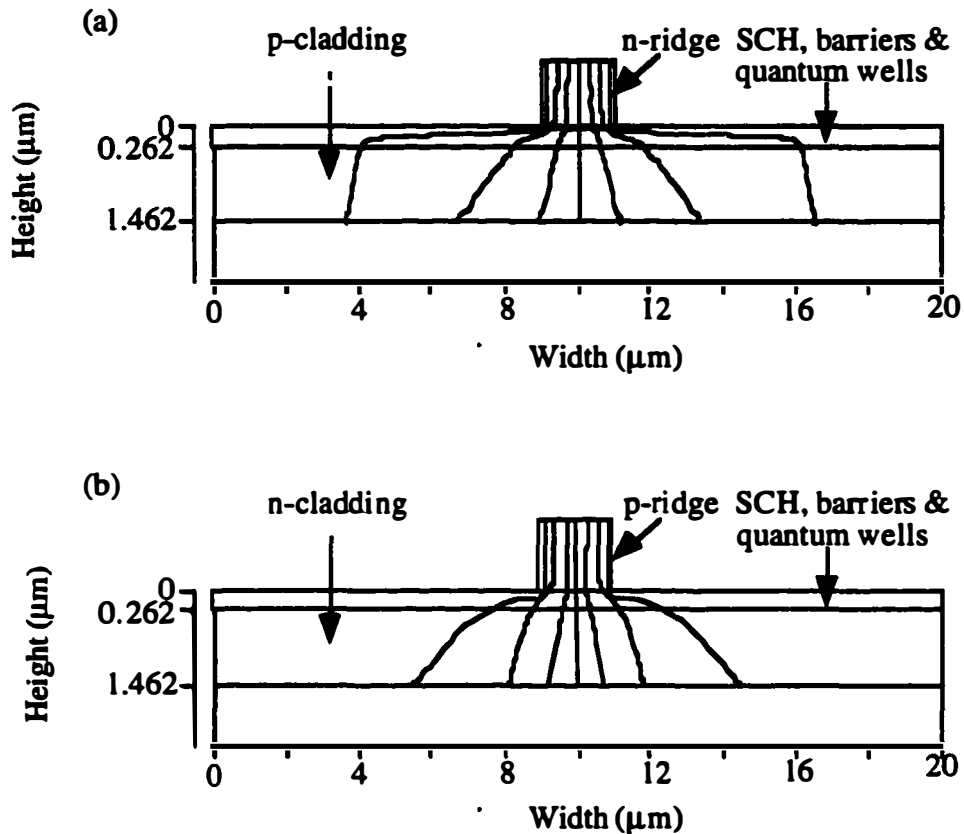


Figure 3. Quantum well band diagram used for simulations. The structure shown here models the MOCVD epi wafers used for device fabrication.

### 3.3 Effect of current spreading on threshold

The variation of threshold current with ridge width is shown in Figure 5 (a) for both cases. The thresholds of the p-up devices increase linearly with increasing ridge width, thus proving the ridge width to be a critical parameter for determining the threshold current. In contrast, a very weak linear trend (changes small compared

to the absolute value of the threshold) is observed in the n-ridge lasers and the lateral leakage current - not the ridge width - is the dominant contribution to the threshold



Figures 4. Simulated current distribution in 2  $\mu\text{m}$  wide ridge lasers. Each bounded region represents 1/8 of the total injection current. Figure (a) is an n-ridge laser; the lateral leakage is much greater than in the p-ridge laser of Figure (b).

current. In these particular simulations, the p-ridge leakage current still is a significant contribution to the current, and the threshold does not pass through the origin, as would occur if there were no leakage at all. Nonetheless, the superiority of the p-ridge in terms of threshold is clear: the p-ridge y-intercept is 3.5 mA, and the slope is 0.7 mA/ $\mu\text{m}$ , whereas the n-ridge y-intercept is 16 mA, and the slope is 0.2 mA/ $\mu\text{m}$ . By comparing these intercepts with threshold currents from devices

where the active region is completely etched away (i.e. minimal leakage current - to be presented in the next section), an equivalent current width can be determined for injection from an infinitesimal source. For the p-ridge laser, the equivalent width is close to  $4 \mu\text{m}$ ; for the n-ridge laser, the equivalent width is  $14 \mu\text{m}$ . An etched active region laser is not a perfect reference, since the mode changes when the active region is etched away and the confinement factor is affected. The close agreement between these equivalent widths and the current span widths (75% of p-ridge current in  $4.75 \mu\text{m}$ , 75% of n-ridge current in  $12 \mu\text{m}$ ) discussed above suggest the analysis is reasonable, and that confinement factor effects are minimal as long as the device is single mode.

#### **3.4 Effect of current spreading on efficiency**

The lateral diffusion current can be separated into two components: (1) electrons that first diffuse laterally in the upper SCH, and then are captured by the quantum wells, and (2) electrons that diffuse vertically from the ridge through the SCH into the quantum wells, where they diffuse laterally. Identifying these two components is useful because a marked change occurs in the the lateral diffusion current above threshold. Above threshold, the radiative recombination lifetime drops rapidly, and any active area electrons within the region of the optical mode rapidly recombine due to stimulated emission. Since the recombination time drops by about two orders of magnitude above threshold, the lateral diffusion of active region electrons is significantly reduced. The electrons that first diffuse laterally in

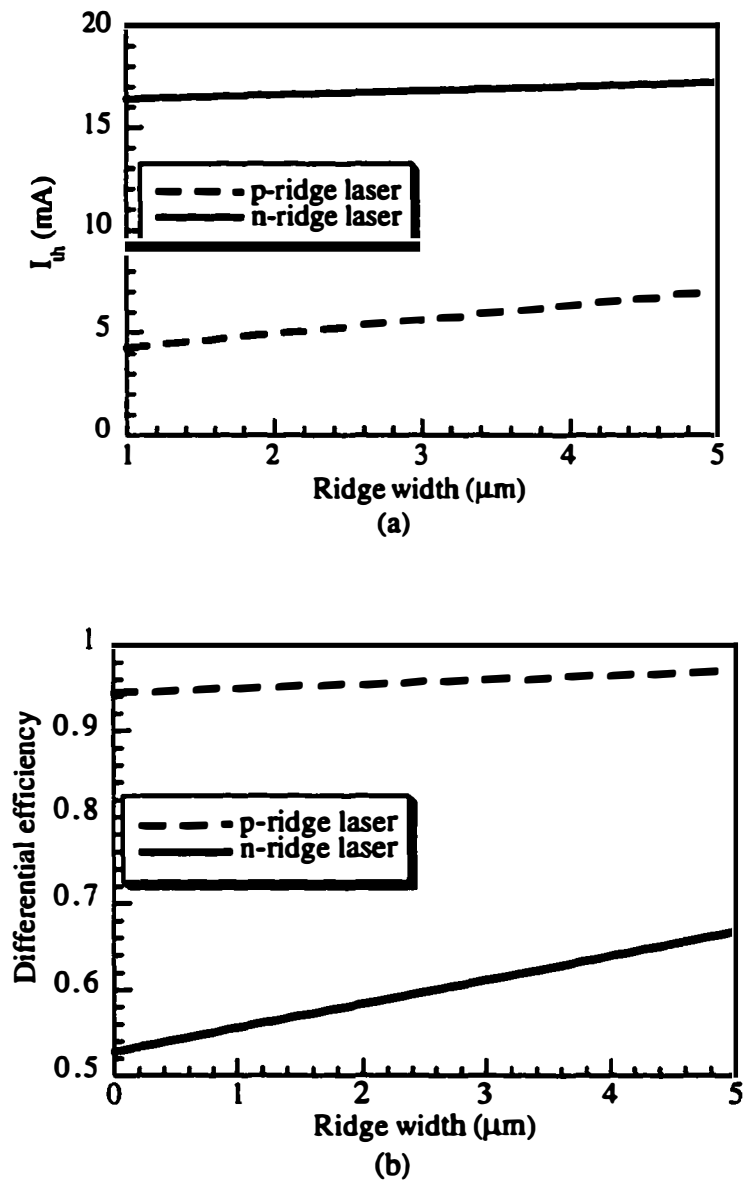


Figure 5. (a) Simulated threshold current versus ridge width for n-ridge and p-ridge lasers, where the ridge etch is stopped at the upper SCH, as in Figure 3. The lateral leakage of the n-ridge lasers is significantly larger than that of the p-ridge lasers; the consequent threshold currents are much higher, and the dependence of threshold on ridge width is weaker. (b) Simulated efficiencies versus ridge width.

the upper SCH, and occupy a space external to the laser mode, will still be captured by the quantum wells and spontaneously recombine. In an ideal laser there would not be any lateral spreading in the upper SCH, because the carrier density in the active region should perfectly clamp, resulting in a zero impedance current path; the fact that there is lateral leakage above threshold points to the reality that carrier density in the confinement region, as well as the active region, does not perfectly clamp, and that the lateral impedance to electron flow is comparatively low. The magnitude of the above threshold current spreading can be understood by examining the variation of differential efficiency with ridge type (p or n), and ridge width. This is shown in Figure 5 (b). The efficiencies of the p-ridge lasers, with less leakage current, range from 45% (for 5  $\mu\text{m}$  wide ridges) to 70% (for 1  $\mu\text{m}$  wide ridges) bigger than the n-ridge lasers. The variation is indicative of the fact that the lateral leakage current is significant above threshold, but the fractional effect is smaller than its effect on the threshold current, which for the 1  $\mu\text{m}$  ridge increases by almost a factor of 4. The absolute values of the calculated differential efficiencies are actually quite high, the reason for this being that in the simulation, no excess internal optical loss was factored in to the simulation. One final point is that very little radiative recombination occurs in the upper SCH in any spatial region - no matter the bias condition. This is because holes diffusing up from the lower SCH are easily captured by the quantum wells [13, 14], and as a result, very few are available for recombination with electrons in the upper SCH.

### **3.5 Experimental verification of current spreading**

The lateral leakage can be verified experimentally by measuring the near field spontaneous emission pattern of an n-ridge laser [7, 15]. There are both electrons

and holes in the same region of the device (that region defined by the lateral spreading of the electrons as discussed above) and radiative recombination shows up as spontaneous emission in the near field. In Figure 6, a near field of a 5  $\mu\text{m}$  wide ridge microstrip laser is shown. An outline of the ridge laser structure is superimposed on the plot to give an idea of the lateral dimensions of the spontaneous emission. An exact number for the extent of the measured spontaneous emission is difficult to determine from the picture, since the camera with which the data were taken was not calibrated for spatial measurements. A rough calibration can be made by assuming that the diameter of the laser mode is about the same as the ridge width - 6  $\mu\text{m}$ . Since the measurement is of the near field, this should be reasonably accurate. The near field pattern shows that the majority of the spontaneous emission exists within a 20  $\mu\text{m}$  region centered on the laser mode. This is consistent with the calculated electron diffusion length of 10  $\mu\text{m}$  - electrons diffuse 10  $\mu\text{m}$  to either side. The fact that the spontaneous emission appears brighter on the right side of the picture is likely caused by some flaws in the imaging optics or a partial blocking of left side facet of the laser.

Table 1 lists some experimental data for thresholds and efficiencies for narrow p-ridge and n-ridge lasers. Broad area results for 50  $\mu\text{m}$  wide ridge lasers are also listed as a reference, since different base material was used for the two narrow ridge lasers. The variation in bar length may account for some of the measured differences, but the lengths are similar enough that they cannot account for the gross differences between narrow ridge lasers recorded in the table. The data in the table supports the calculations in Figure 5; a more detailed presentation of the

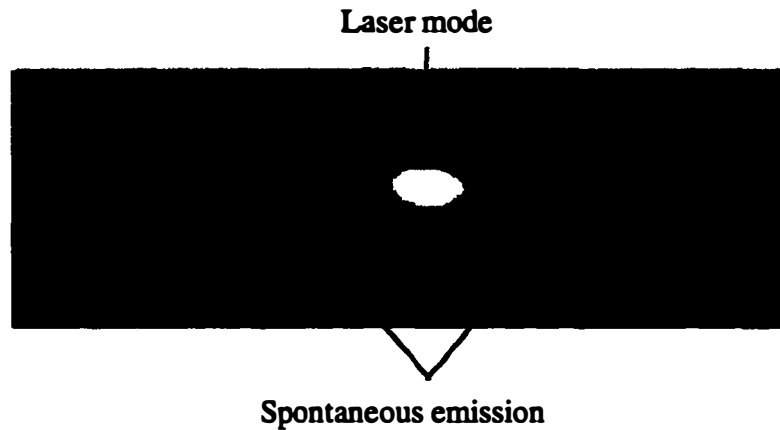


Figure 6. Near field pattern from a 6  $\mu\text{m}$  wide n-ridge microstrip laser, showing the laser mode and lateral spontaneous emission from current spreading.

Sample and material	Bar length	Threshold current density	Differential efficiency
Broad area laser, mat. A	680 $\mu\text{m}$	0.8 kA/cm <sup>2</sup>	0.4
3 $\mu\text{m}$ p-ridge laser, mat. A	605 $\mu\text{m}$	1.16 kA/cm <sup>2</sup>	0.18
Broad area laser, mat. B	540 $\mu\text{m}$	0.8 kA/cm <sup>2</sup>	0.2
6 $\mu\text{m}$ n-ridge laser, mat. B	620 $\mu\text{m}$	3.2 kA/cm <sup>2</sup>	0.04

Table 1. Experimental threshold and efficiency data for n-ridge and p-ridge lasers, with the ridge etch stopped at the SCH.

experimental results can be found in Chapter 5. The degradation in threshold and efficiency observed for the p-ridge sample is not unusual in a narrow ridge laser, as the ridge process introduces excess optical scattering loss that increases the threshold and lowers the differential efficiency.

### 3.6 Etched active regions

The most general conclusion taken from the data and calculations of Figures 4-6 and Table 1 is that the lateral diffusion of the electron current must be restricted to make a good laser. High thresholds and low efficiencies result in excess device heating, low power output, and low photon densities - all properties that prevent the realization of a good high speed, high power laser. Several techniques can be used to restrict or eliminate the lateral diffusion current in an n-ridge device, including etching through the SCH/active region or doing an ion implantation. Implantation to insulate against electron current in InGaAsP is more complicated than etching the active region away, and was not attempted in this work. There have been several reports in the literature of the InGaAsP/InP devices fabricated with phosphorus and gallium ion implantation [10] and it is not an unfeasible process. Etching the ridge through the upper SCH and active region is a simpler way to confine the electron current. The lower SCH does not need to be etched away since the hole diffusion is small. As will be discussed in more detail in Chapter 4, Device Fabrication, a dilute mixture of saturated bromine water and phosphoric acid suffices to etch quaternary InGaAsP, and it etches the SCH, barrier, and quantum well regions at roughly equal rates, so undercut is manageable. The bromine water - phosphoric acid mixture also etches InP, typically cutting through a small fraction of the bottom p-cladding, although careful measurement of the etched surface can ensure that, for the most part, only the upper SCH and the quantum wells and barriers are removed.

The threshold and efficiency calculations of Figure 5 were redone with the etch modified. In one calculation only the upper SCH was etched away, and in the second, the upper SCH and the entire multiple quantum well active region was

removed. The calculation was done assuming a sidewall recombination rate in the SCH and in the active region of  $10^4$  cm/s, which is a realistic value for InGaAsP [16]. This value is low and does not contribute to significant sidewall recombination current as was verified by running the identical simulations with a null value for the surface recombination velocity; virtually identical thresholds were obtained for the two cases. Figure 7 (a) shows the threshold currents versus ridge width for the p-ridge lasers, and Figure 7 (b) shows the same plots for n - ridge lasers. The plots reveal a few things. Comparing the results for the partial etch to those of Figure 5 (a), we see that the threshold behavior is not changed significantly. Below threshold, the recombination lifetimes in the quantum wells are long, on the order of a nanosecond, electrons still diffuse in the lateral direction in the active region, and the thresholds are high, particularly in the n-ridge lasers. When the active region is etched away completely, the thresholds drop, and they show a strong monotonically increasing dependence on ridge width. Most significantly, the n-ridge laser thresholds are reduced to levels equal to the thresholds of complementary p-ridge lasers. For both doping types, the x-intercept is now below 1 mA, and the slope is about  $0.85 \text{ mA}/\mu\text{m}$ . The fact that the intercepts are close to zero and that the slope is the highest value of any calculations done indicate that the leakage currents are best minimized by etching through the active region.

The variation of efficiencies with ridge width for the different conditions are plotted in Figure 8. The results are consistent with the threshold results of Figure 7; the best performance is achieved when the active region is completely etched away. The surprising result from these calculations relates to the efficiency. With the upper

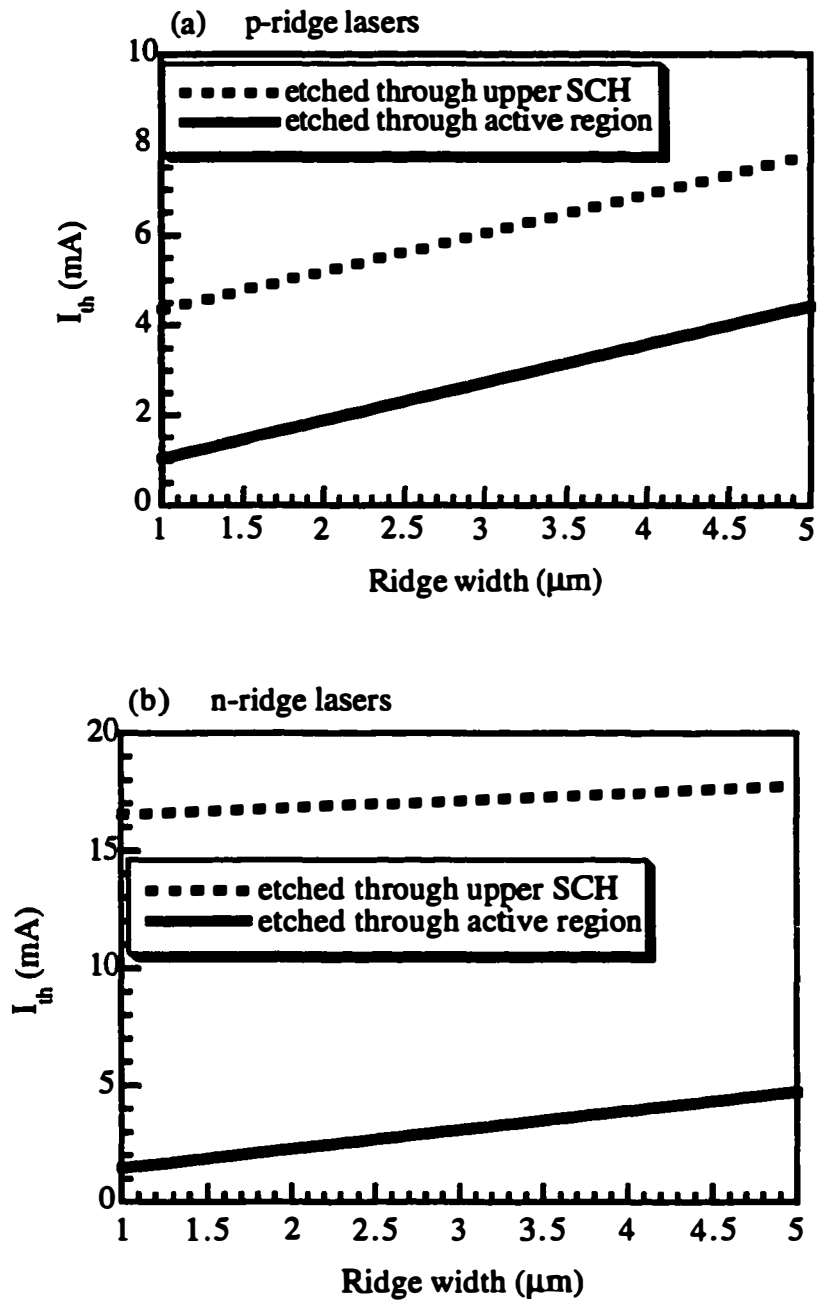


Figure 7. (a) Threshold versus ridge width for p-ridge lasers. (b) Threshold versus ridge width for n-ridge lasers. Both plots show the best threshold performance is obtained when the ridge is etched all the way through the quantum well region.

SCH removed, one would expect the differential efficiency to closely match the efficiency for the case where the active region is totally removed. As discussed earlier, above threshold there should be little current spreading in the active region because the recombination time drops significantly. However, this calculation suggests different behavior and it is not clear why. The problem may be related to the ATLAS simulation program, which models the potential distribution of quantum wells, but does not incorporate quantum well models for gain and density of states.

Table 2 shows some experimental data for 5  $\mu\text{m}$  n-ridge lasers, etched through the upper SCH, and through the active region. The table also includes broad area laser results as a reference. The data support the calculations: the best results are obtained for the completely etched active region, for both threshold and efficiency.

As mentioned earlier, etching through the active region does not degrade the threshold through surface recombination, because in InGaAsP the surface recombination velocity is only  $10^4$  cm/s. On the other hand, if the surface recombination velocity is increased to  $10^5$  or  $10^6$  cm/s, the thresholds noticeably increase. Simulations for a 2  $\mu\text{m}$  n-ridge were done for these higher values of recombination, and the thresholds rose to about 5 mA and 19 mA respectively, compared to the 2.3 mA value obtained for the original calculation. The calculation does suggest that etching through an InGaAs active region with a characteristic surface recombination velocity of  $10^5$  cm/s, for example, will cause the threshold to rise.

Some general statements can be made from the simulations and the experimental data regarding fabrication of p and n ridge lasers. In both cases, under

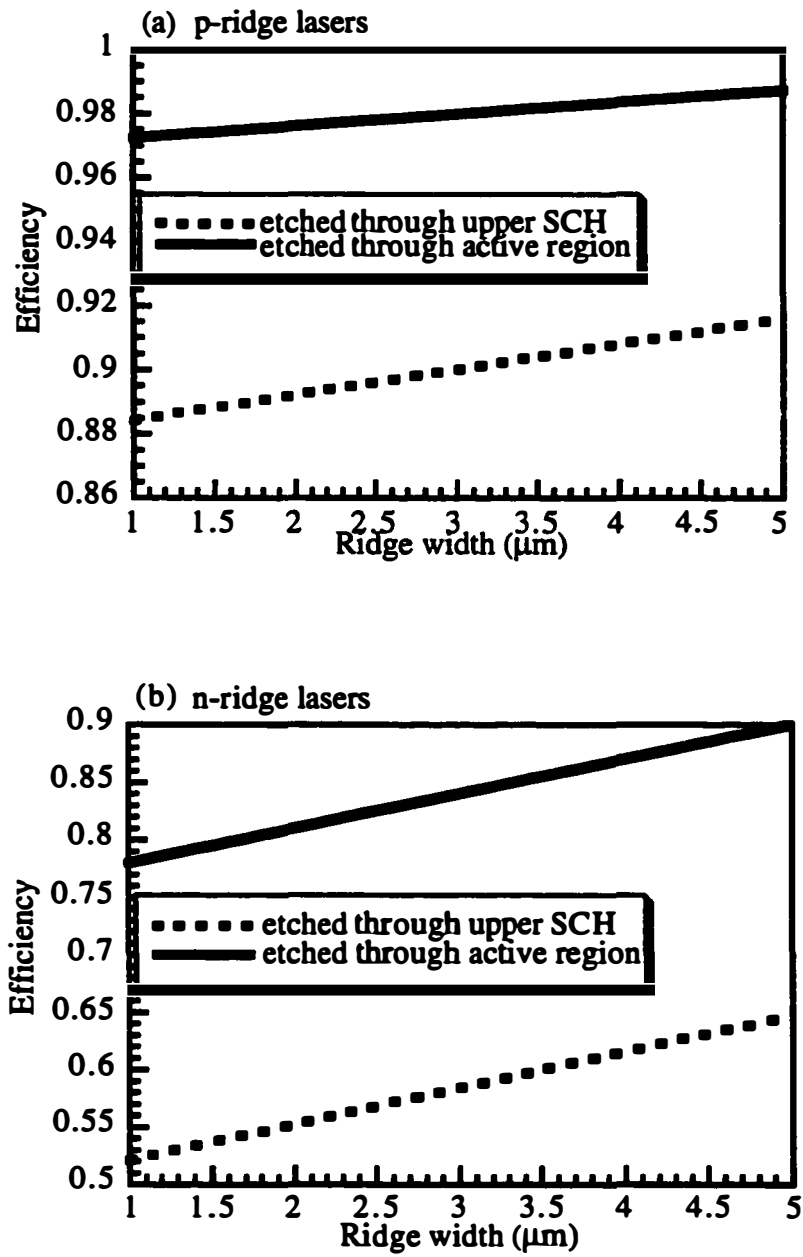


Figure 8. (a) Efficiency versus ridge width for p-ridge lasers. (b) Efficiency versus ridge width for n-ridge lasers.

Sample and material	Bar length	Threshold current density	Differential efficiency
Broad area laser, mat. A	680 $\mu\text{m}$	0.8 kA/cm <sup>2</sup>	0.2
5 $\mu\text{m}$ n-ridge laser, etched through upper SCH, mat. A	600 $\mu\text{m}$	4.3 kA/cm <sup>2</sup>	0.043
Broad area laser, mat. B	500 $\mu\text{m}$	1.2 kA/cm <sup>2</sup>	0.48
5 $\mu\text{m}$ n-ridge laser, etched through active mat. B	460 $\mu\text{m}$	2.3 kA/cm <sup>2</sup>	0.244

Table 2. Experimental threshold and efficiency data for n-ridge lasers etched either through the upper SCH, or through the active region completely. The complete active region etch demonstrates superior performance.

ideal circumstances, leakage currents are reduced by etching through the active region and should improve performance. In the n-ridge laser there is no choice: reasonable threshold and efficiencies will only be achieved if the active region is etched away. For the p-ridge laser, the conclusion is not so clear, and a small improvement in current confinement probably does not compensate, in practice, for additional problems effected by the extra etch, such as reduced lifetime, excess optical loss, and multimode operation. Current confinement by ion implantation is an another alternative since it potentially can minimize the current spreading while avoiding the problems of the etched active region.

### 3.7 Electrical resistance

Differences in electrical resistance between n-ridge and p-ridge lasers, and between microstrip and conventional lasers, have important ramifications for high power and high speed performance. The majority of the total voltage drop, in all

cases, is localized in the p-region, and depending on device type and ridge doping, the resistance will change. In general, p-ridge lasers have higher resistance than n-ridge lasers because the hole current is more narrowly confined in the p-ridge. Conventional lasers have higher resistance than microstrip lasers because there is no current flow through a thick substrate. This last difference is most striking between the n-ridge microstrip laser and the n-ridge conventional laser: the hole current only flows through 1.2  $\mu\text{m}$  of p-cladding in the microstrip laser rather than the entire p-substrate. In the p-ridge lasers, this difference is negligible because of the low resistance of the n - substrate. In Figure 9, the total device resistance is plotted for the p-ridge conventional laser, the n-ridge conventional laser, and the n-ridge microstrip laser, versus ridge width. The simulations only include bulk resistances and do not take into account the contact resistance between metal and semiconductor and the heterojunction resistance at the contact layer- cladding layer interface. As in the earlier simulations the bar length is 50  $\mu\text{m}$ . The resistance of the n-ridge devices is smaller than the p-ridge devices in all cases except the 5  $\mu\text{m}$  wide conventional lasers. In practice, even a 5  $\mu\text{m}$  p-ridge has a larger resistance than the n-ridge because of the contact and heterojunction resistances. The plot shows, as expected, that the best resistance is obtained from the n-ridge microstrip laser. In this particular simulation, the substrate thickness was 10  $\mu\text{m}$ , much smaller than the usual lapped sample thickness of about 100  $\mu\text{m}$ . The simulation still clearly demonstrates the superior resistance of the microstrip laser design.

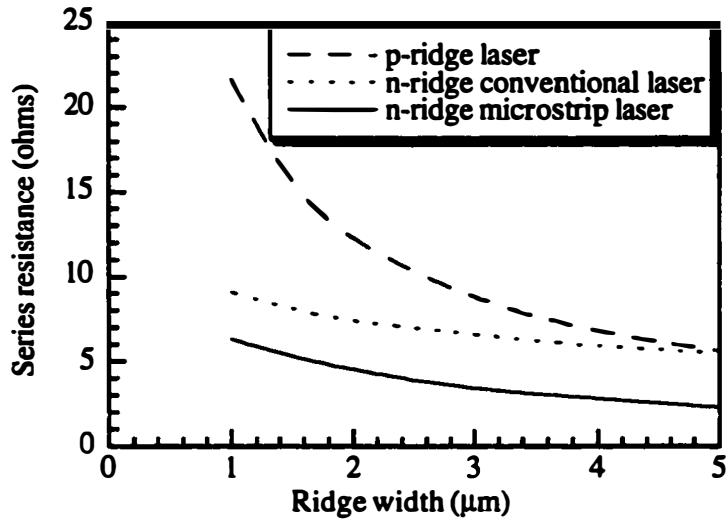


Figure 9. Calculated series resistances for the three different different laser structures. In this plot, the ridge etch is stopped at the upper SCH.

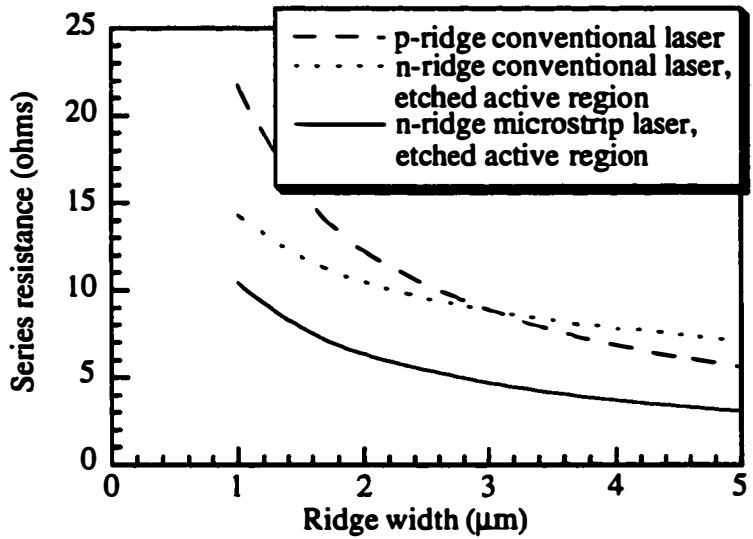


Figure 10. Calculated series resistances for three different laser structures. The n-ridge lasers are etched through the active region, the p-ridge laser is etched to the upper SCH.

Etching through the SCH and the active region introduces excess resistance. Although in principle the carrier density clamps, it does not in practice and so the resistance scales with the width of the diode. The resistance of n-ridge microstrip lasers and n-ridge conventional lasers with the upper SCH and active region etched away are shown in Figure 10 along with the unetched p-ridge laser resistance. This comparison is made because these are the kinds of structures that would most likely be fabricated in practice. The resistance of the n-ridge lasers increases with the removal of the active region, but is still lower than the conventional p-ridge laser resistance for most cases. Above 3  $\mu\text{m}$  width, the n-ridge conventional resistance is higher than the p-ridge resistance, but only slightly, and the microstrip laser resistance remains the lowest of all. The experimental results on electrical resistance are presented in Chapter 5, and show, for the best narrow n-ridge microstrip devices, resistances of 1 ohm or less, which is significantly lower than the typical result for a p-ridge conventional laser.

### **3.8 Heat conduction and thermal resistance**

The thermal properties of a semiconductor laser are connected to its electrical properties because heat generation is caused by the various electrical processes operating. Current flow in doped regions is ohmic, and heat is generated through  $I^2R$  joule heating. In the SCH and active region, drift, diffusion, and recombination make up the current flow; all these processes, except for radiative recombination, generate  $IV$  heat power (primarily through scattering mechanisms that heat the lattice).

Two structural factors linked to thermal performance are the doping of the ridge and, in the microstrip laser, the gold bonded layer. The ridge affects the thermal resistance by its doping type and by its location relative to the heat sink. The most common, and the simplest, mounting technique involves soldering the laser onto a copper stud, with the substrate side of the laser contacting the stud. In this geometry, heat generated in the ridge flows through the active region, down through the substrate and out the heat sink. The heat flow increases the temperature of the active region and because the largest heat source is usually the p-cladding, a p-ridge device mounted this way has a high thermal resistance. In an n-ridge device, heat generation in the ridge is minimal and the heat generated in the p-cladding flows out the heat sink without passing through the active region. This results in only a small increase in the active region temperature and a lower thermal resistance.

A more complicated mounting technique involves mounting the device upside down, so that the top of the ridge, rather than the substrate, makes electrical and thermal contact to the heat sink. This is commonly called p-side down mounting, since it's only advantageous when done with a p-ridge. This method improves the thermal resistance of the p-ridge laser [3] because the joule heat from the ridge now flows out of the heat sink without passing through the active region. An n-ridge laser mounted substrate side down achieves similar thermal performance as p-side down mounting, because the majority heat source is already located close to the heat sink. Since no complicated post fabrication processes are needed to achieve this, the n-ridge laser presents a great advantage as far as processing is concerned.

The gold layer below the lower cladding in the microstrip laser introduces an additional thermal advantage, since the thermal conductivity of gold is higher than that of any semiconductor used for fabricating lasers. The room temperature thermal conductivity of gold is 3.15 W/cm-K; the thermal conductivity of InP is 0.68 W/cm-K [17] and the thermal conductivity of GaAs is W/cm-K [18]. Intuitively, the gold layer acts as a heat spreading layer, and the heat rapidly distributes over a wide lateral region, resulting in an intrinsically lower thermal resistance than a conventional laser. The reduction in thermal resistance is calculated to about 10% for a 10  $\mu\text{m}$  ridge microstrip laser with a 1  $\mu\text{m}$  gold-bonded layer [19]. This is the calculated reduction considering only active region heating, done to isolate the effect of the gold layer from the effect of the ridge, which depends on doping type. The thermal resistance decreases as the gold layer thickness increases. The best thermal resistance would be achieved by eliminating the InP substrate altogether and replacing it with a 50-100  $\mu\text{m}$  gold plated layer as the back plane of the laser. This scheme would also eliminate the bonding step and further simplify the process; a need to cleave the processed wafer into laser bars disallows this (cleaving through 50-100  $\mu\text{m}$  of gold is impossible). A procedure by which high quality facets are etched, rather than cleaved, would permit such a device. Etched facets with reflectivities equivalent to cleaved facets have been reported [20], and a host of different laser possibilities can be envisioned if such a process were utilized. Some examples are the gold plated laser substrate discussed above and a microstrip laser with a high thermal conductivity aluminum nitride substrate.

The heat flow and heat distribution in the various laser structures (n-ridge conventional, p-ridge conventional, n-ridge microstrip, p-ridge microstrip) were

calculated with the same ATLAS program used for the electrical calculations, and are shown in Figure 11 (a) - (d). The plots are done for 1  $\mu\text{m}$  ridge lasers with 50  $\mu\text{m}$  cavity lengths as discussed earlier. Figure 11 (a) shows the temperature contours for the n-ridge conventional laser well above threshold. The temperature increase is 17  $^{\circ}\text{C}$ , the power dissipated at threshold is 130 mW, and the thermal resistance is about 130 K/W.

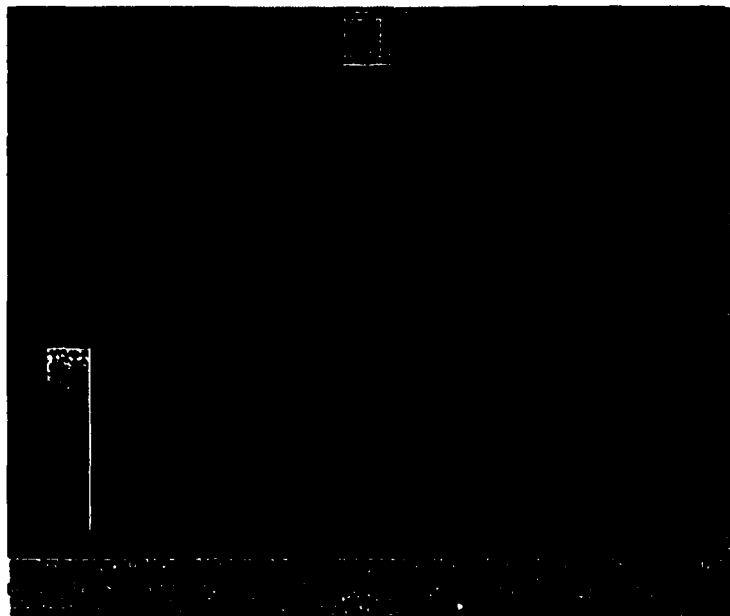


Figure 11 (a). Heat distribution through the semiconductor laser well above threshold, for an n-ridge laser. The active region temperature has risen to 17  $^{\circ}\text{C}$  above the unbiased temperature.

### 3.9 Summary and conclusions

The static operating properties of the microstrip laser were investigated in this chapter. Some basic design and fabrication principles were drawn from the analysis, along with predictions regarding device performance. First, because of the difficulties associated with p-down materials growth in the InP system with

MOCVD, most microstrip lasers end up being n-up lasers (due to the epi inversion intrinsic to our bonding process). The n-ridge laser is much more susceptible to lateral current spreading than is a p-ridge laser, and can result in very high threshold currents and low efficiencies. An active region etch eliminates this problem and is a practical solution. Improvements in both electrical resistance and thermal resistance are predicted in the microstrip laser, and are critical for high speed and high power operation. The electrical resistance improvement is related to the low resistance n-ridge, and the thin 1.2  $\mu\text{m}$  p-layer region intrinsic to the microstrip design. The thin p-layer contributes significantly less resistance than one finds in a n-ridge laser on a p-substrate, where the current must flow through many microns of low mobility p-material. The thermal resistance improvement is related to the proximity of the primary heat source - the p-layer - to the gold fused layer and the heat sink. The gold fused layer near the active region, with a thermal conductivity about 5 times higher than InP, also contributes to a reduced thermal resistance.

These predictions are borne out experimentally in Chapter 5. The next chapter, Chapter 4, presents the fabrication and bonding techniques employed for making microstrip lasers that demonstrate the performance properties that were have been discussed here.

## References

- [1] H. Wada, H. Horikawa, Y. Matsui, Y. Ogawa, and Y. Kawai, "High-power and high-speed 1.3  $\mu\text{m}$  V-grooved inner-stripe lasers with new semi-insulating current confinement structures on p-InP substrates," *Applied Physics Letters*, vol. 55, pp. 723-5, 1989.

- [2] D. Tauber, M. Horita, J. A. L. Holmes, B. I. Miller, and J. E. Bowers, "The microstrip laser," presented at *Integrated Photon. Research Conf.*, Boston, 1996.
- [3] J. Piprek and W. Both, "Thermal resistance of InGaAs/InP laser diodes," *Journal of Thermal Analysis*, vol. 36, pp. 1441-1456, 1990.
- [4] S. Adachi, "Thermal conductivity of InGaAsP," in *Properties of InP*, S. Adachi and J. Brice, Eds. London and New York: INSPEC, the Institution of Electrical Engineers, 1991, pp. 384-386.
- [5] H. Wada and T. Kamijoh, "1.3- $\mu\text{m}$  InP-InGaAsP lasers fabricated on Si substrates by wafer bonding," *IEEE Journal of Selected Topics in Quantum Electronics*, vol. 3, pp. 937-42, 1997.
- [6] Silvaco International, version 4.0, Santa Clara, CA 94054, 1995.
- [7] J. H.S. Sommers and D. O. North, "Experimental and theoretical study of the spatial variation of junction voltage and current distribution in narrow stripe injection lasers," *Journal of Applied Physics*, vol. 48, pp. 4460-4467, 1977.
- [8] W. B. Joyce and S. H. Wemple, "Steady-state junction-current distributions in thin resistive films on semiconductor junctions," *Journal of Applied Physics*, vol. 41, pp. 3818-3830, 1970.
- [9] W. T. Tsang, "The effects of lateral current spreading, carrier out-diffusion, and optical mode losses on the threshold current density of GaAs-Al<sub>x</sub>Ga<sub>1-x</sub>As stripe geometry DH lasers," *Journal of Applied Physics*, vol. 49, pp. 1031-1043, 1978.
- [10] J. E. Zucker, K. L. Jones, B. Tell, K. Brown-Goebeler, C. H. Joyner, B. I. Miller, and M. G. Young, "InGaAsP/InP quantum well buried heterostructure waveguides produced by ion implantation," *Electronics Letters*, vol. 28, pp. 853-5, 1992.
- [11] W. Siegel, B. J. Sealy, R. K. Ahrenkiel, and G. Kuehnel, "Hole mobility, diffusion and lifetime," in *Properties of InP*, S. Adachi and J. Brice, Eds. London and New York: INSPEC, the Institution of Electrical Engineers, 1991, pp. 83-90.
- [12] D. Lancefield, R. K. Ahrenkiel, and B. J. Sealy, "Electron mobility, diffusion and lifetime," in *Properties of InP*, S. Adachi and J. Brice, Eds. London and New York: INSPEC, the Institution of Electrical Engineers, 1991, pp. 63-82.
- [13] N. Tessler and G. Eisenstein, "On carrier injection and gain dynamics in quantum well lasers," *IEEE J. Quantum Electron.*, vol. 29, pp. 1586-1595, 1993.

- [14] S. C. Kan, D. Vassilovski, T. C. Wu, and K. Y. Lau, "Quantum capture and escape in quantum-well lasers - implications on direct modulation bandwidth limitations," *IEEE Photon. Tech. Lett.*, vol. 4, pp. 428-431, 1992.
- [15] B. W. Hakki, "Carrier and gain spatial profiles in GaAs stripe geometry lasers," *Journal of Applied Physics*, vol. 44, pp. 5021-5028, 1973.
- [16] L. A. Coldren and S. W. Corzine, *Diode Lasers and Photonic Integrated Circuits*. New York: John Wiley and Sons, 1995.
- [17] J. C. Brice, "Thermal conductivity of InP," in *Properties of InP*, S. Adachi and J. Brice, Eds. London and New York: INSPEC, The Institution of Electrical Engineers, 1991, pp. 20-21.
- [18] S. Adachi, *GaAs and related materials*. Singapore: World Scientific, 1994.
- [19] D. Tauber, M. Horita, J. Piprek, P. Abraham, J. A. L. Holmes, and J. E. Bowers, "The microstrip laser," to be published *IEEE Photonics Technology Letters*, vol. 10, April 1998.
- [20] J. D. Ralston, S. Weisser, I. Esquivias, E. C. Larkins, J. Rosenzweig, P. J. Tasker, and J. Fleissner, "Control of differential gain, nonlinear gain and damping factor for high-speed application of GaAs-based MQW lasers," *IEEE J. Quantum Electron*, vol. 29, pp. 1648-1658, 1993.



## Chapter 4

### Microstrip laser fabrication

Three main subdivisions constitute the microstrip laser fabrication process. The first is the epitaxial growth, which was all done by metal-organic chemical vapor deposition (MOCVD) for the devices presented in this dissertation. The second subdivision consists of wafer bonding and substrate removal. These two steps produce an epitaxial film of laser material on a 1 micrometer ( $\mu\text{m}$ ) thick gold layer. The final subdivision is the processing of the film into ridge waveguide lasers. This processing is identical to that used for fabricating conventional ridge lasers on standard substrates. Figure 1 schematically demonstrates the steps involved in turning two separate wafers into one microstrip wafer, joined at the bonded gold layer.

#### 4.1 Materials growth

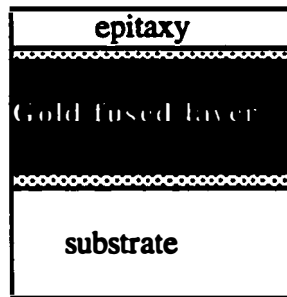
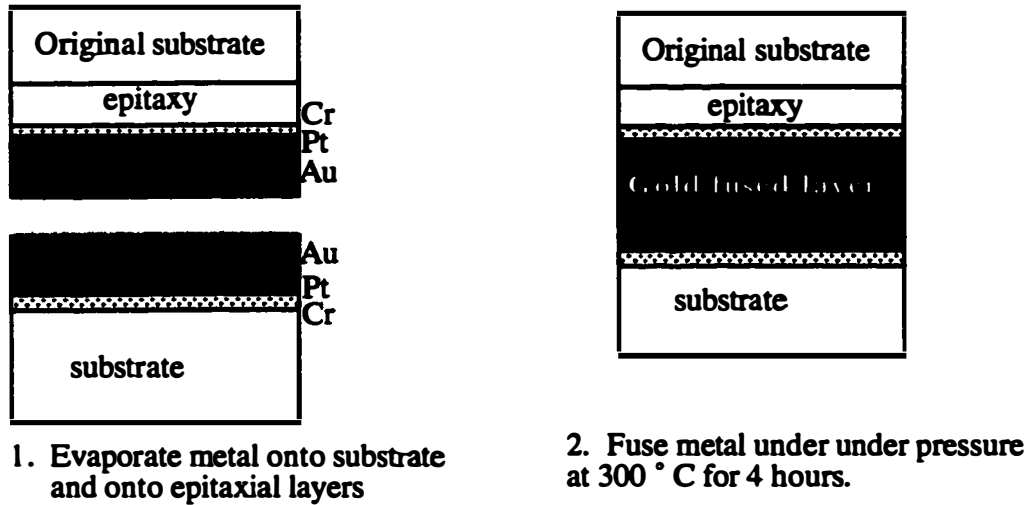
The wafers used for device fabrication are grown by MOCVD, with an active region made up of six strained InGaAsP quantum wells, 8 nm thick. The conduction band diagram is shown in Figure 3, Chapter 3. The wells are compressively strained between 0.4% and 1% (depending on the wafer - the wells in a single wafer have constant strain throughout). The more highly strained structures were used for the later processes used in this work (devices with etched active regions) and incorporated strain compensating barriers. The active emits light at 1.55  $\mu\text{m}$ . There are seven 1.25  $\mu\text{m}$  barriers, 7 nm thick each, and two 75 nm 1.15

$\mu\text{m}$  separate confinement heterostructures (SCH), symmetrically placed about the active and barrier regions. Surrounding the SCH regions are  $1.2 \mu\text{m}$  of InP cladding, doped to  $10^{18} \text{cm}^{-3}$ .  $1.2 \mu\text{m}$  of InP is used for both p and n cladding. Zn is the p-dopant and Si is the n-dopant, with the bottom cladding being n-doped for all growths used in this work. The  $1.2 \mu\text{m}$  bottom cladding is a thicker growth step than usual, as a normal MOCVD wafer is grown with about  $0.5 \mu\text{m}$  of bottom cladding material. The thick bottom cladding is necessary in the microstrip laser because the epi inversion intrinsic to the process transforms the *grown* bottom cladding into the top cladding of the bonded microstrip wafer. The whole epi structure is sandwiched between two highly doped InGaAs cap layers, doped to about  $3 \cdot 10^{19} \text{cm}^{-3}$ . The InGaAs is lattice matched to InP.

A schematic of the epi layer structure is found in Appendix II.

#### 4.2 Surface preparation, metal evaporation, and bonding

The bonding process begins with surface inspection and surface preparation of the two wafers. Smooth surfaces are critical for achieving a uniformly bonded layer, and while the gold is malleable enough to compensate for some imperfections, the yield and reproducibility of the process is affected by the surface roughness - the gold is not a solder capable of filling gaps. The uniformity of the plain substrate is usually superior to that of the epi laser wafer. For our devices, more than  $3 \mu\text{m}$  of epi is grown and it is inevitable that some defects will form and propagate to the surface [1]. The difference is visible in an optical microscope. Optical microscope pictures of the surface of the as-grown epi and a substrate are compared in Figure 2 (a) - (c). The morphology of the wafer center can be quite



3. Remove original substrate by wet chemical etching. Etching stops on stop etch layer.

Figure 1. Gold bonding process for turning two wafers into a microstrip wafer.

good, and only a few defects may be observable. Figure 2 (a) is representative, with the defects boxed in for clarity. Most of the wafer area surrounding the defects is very smooth. Figure 2 (b) shows the wafer edge, which is typically of much poorer quality than the wafer center, as can be seen by the dense distribution of defects. The bonding at the wafer edges is usually not very good, but the poor morphology there does not affect the quality of the bonding in other regions of the

wafer. The substrate on the other hand, usually displays a near-perfect morphology as is demonstrated in Figure 2 (c). Nothing can really be done about surface defects after the wafer is grown. They are not typically large enough to significantly affect the quality of the bonding, although a large defect will result in a poorly bonded area on the wafer that shows up as a bubble on the film surface after substrate removal. Figure 3 shows an example of such a bubble. The affected area is about 1 square millimeter. The only thing that can be done to minimize this problem is to ensure that the surface morphology of the epi is adequate for bonding. Morphologies similar to those in Figure 2 (a) are adequate.



(a) - laser epi surface,  
wafer center  
(400 x mag.)



(b) - laser epi surface  
wafer edge  
(100 x mag.)



(c) - InP substrate  
(400 x mag.)

Figure 2. Optical microscope pictures of wafer surfaces used for bonding. The pictures are of the surfaces before the metal evaporation.



**Figure 3. Bubble on the surface of a bonded wafer caused by a defect on the wafer. (50 x mag.)**

Apart from defects, other surface imperfections can degrade the quality of the gold fusion - small particles, surface oxides, and residue from solvents. These imperfections can be almost completely removed by careful cleaning procedures. A by product of cleaving is small particles on the wafer surface. The area of the epi wafer bonded is usually between 60 to 100 square millimeters - 8 mm to 1 cm on a side - much smaller than the 1 or 2 inch wafers grown in the MOCVD, so dust is scattered across the surface when the wafer is cleaved to the smaller size. Other small particles can end up on the surface as a result of sloppy handling techniques or from dust in the air. Almost all of these particles can be removed with the following cleaning sequence: (1) blow the wafer with high pressure nitrogen from an N<sub>2</sub> gun. This will blow off most of the particles from the surface. (2) Spray the wafer with acetone while moderately rubbing the surface with a cotton swab. The best way to move the swab is linearly across the surface, picking up particles along the way. (3) Spray the wafer with isopropyl alcohol to remove acetone from the previous step. (4) Immediately dry the wafer with the N<sub>2</sub> gun to ensure that all the solvents have been dried off. After these 4 steps have been completed, the surface quality is

inspected under an optical microscope. If there still appears to be some dust or solvent residue, the procedure can be repeated again. It is important to point out, however, that a minimum number of handling steps should be used for preparing a clean surface, because additional steps always increase the chances that the surface will be contaminated more.

The last cleaning step before evaporation of the metal (for bonding) is oxide removal. A concentrated solution of hydrofluoric acid (HF) is used to remove the oxide from both wafers - the surface layer of the laser wafer is highly doped InGaAs, and the other surface is InP. A 20 second dip, followed by an N<sub>2</sub> dry is sufficient for removing the oxide. The wafers are then loaded into the electron beam evaporator as soon as possible (typically within 5 minutes), and the evaporator is pumped down to a base pressure of about  $1 \cdot 10^{-6}$  or lower.

The oxide removal step is critical, because the strength of the gold bond that forms is greater than that of the adhesion of the metal to the semiconductor surface. Stress on the wafer, either from different amounts of thermal expansion between semiconductor and metal during temperature variable processes, or from cleaving, can cause the metal to pull away from the semiconductor, ruining the wafer bond [2]. This will be shown experimentally in this chapter. Bonding tests were done in which large stresses were induced by fast ramp rates or cleaving. These tests show that the stress is more often relieved by the metal separating from the semiconductor than by the breaking of the gold bond. The adhesion of metal to a surface oxide is very poor, and the presence of an oxide layer can prove fatal to the process and the device. Also, since the metal bonded layer serves as an ohmic contact, an oxide layer between the laser epi and the metal can also cause an undesirably high electrical

resistance. Although a thin native oxide is always formed during the pump down cycle, the thickness must be kept to a minimum by appropriate surface preparation.

The metal evaporated is not just a plain layer of gold; a sequence of 7.5 nm of chrome (Cr), 100 nm of platinum (Pt) and 500 nm of gold (Au) was determined to be the optimum combination of metals. Chrome is a sticking layer, and is used for adhesion of the metal to the semiconductor surface. Platinum is a diffusion blocking layer that prevents the gold from diffusing into the semiconductor during the high temperature processes used in the fabrication (the bonding itself, polyimide curing, annealing). The gold is the actual bonding medium; the three metals together compose the bottom device contact. The evaporation is done at a pressure of  $1 \cdot 10^{-6}$  Torr, or below.

Following evaporation, the metal surfaces are inspected under the optical microscope. Any defects, dust, or nonuniformities that were on the wafer surface prior to evaporation will still be visible after the evaporation. When evaporating the metal, contaminants in the metal sources can sputter on the sample and degrade the cleanliness of the metal. For this reason, it's important to clean the metal sources before doing the evaporation. The metals sources are usually contained in graphite crucibles that sputter and dirty the source after an evaporation. Rinsing the metal surface with isopropanol helps the cleanliness, and if done carefully, can remove almost all of the graphite residue. The chrome and the gold are evaporated from pellets placed in a smaller tungsten crucible that sits in the graphite. This kind of container stays cleaner during an evaporation and is also more easily cleaned after evaporation. In our process, the iso clean was not used on the chrome pellets since they are powdery and dirty to begin with.

The only post-evaporation wafer cleaning done is a rinse in 1 165 (cleanser for removing organics) at 75 °C for about 5 minutes, an ISO spray to remove the 1 165, and an N<sub>2</sub> dry. Any dirt that gets on the wafer during evaporation is below the surface layer and can't be removed. For particles on the surface, the cotton swab cleaning technique described earlier is not used because it scratches the gold surface. Especially because gold is soft, handling following evaporation is kept to a minimum since it greatly increases the chances of scratches and contamination.

Following the cleaning, the two wafers are placed in contact in a methanol solution, with the cleavage planes lined up [3]. The orientation of the wafers is done by eye, and is not exact, but is sufficient for our devices. The contacted wafers are removed from the methanol and dried; the surface adhesion of the methanol keeps the two wafers together. They are then placed in a graphite bonding fixture, shown in Figure 4, designed so that a uniform pressure is applied to the wafers. The top part of the fixture is screwed down with a torque wrench set to torque of 0.65 in-lbs, which was experimentally determined to provide enough pressure for good bonding, without cracking the wafer. The pressure from the top is transmitted to the wafers through the dome shown in Figure 4. Since contact between the dome and the fixture occurs at a single point, the force distributes evenly across the flat bottom of the dome and onto the wafers. The fixture is then placed in an oven in which the temperature is ramped up to 300 °C, and kept there for 4 hours. The ramping rate above 100 °C is 1 °C/minute; the rate is low so as to minimize stresses caused by the differing thermal expansion of the wafer and the gold. If the stresses are too large, the wafer could crack. For the same reason, the ramp down rate is 1 °C/minute.

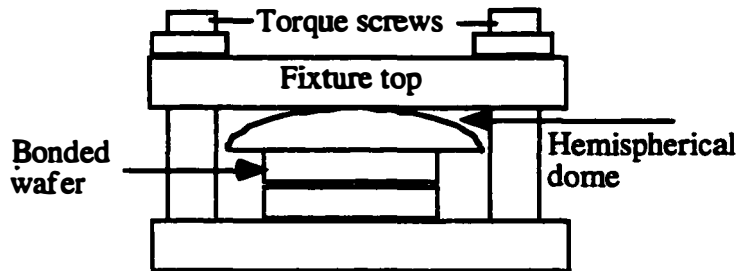


Figure 4. Graphite fixture used for gold bonding. Even pressure is applied to the wafers by using the the hemispherical dome.

The bonding is done in a programmable oven in the clean room under ambient atmospheric conditions. Bonding in a clean nitrogen or forming gas environment is probably more desirable, but no system with this ambient and the required temperature and ramp rate conditions was available. Since the bonding medium is gold, which doesn't oxidize, the atmospheric conditions are not that critical. The cleanliness is of course critical, but the process is flexible enough that good bonding is still achieved despite exposure to other contaminants in the oven atmosphere (photoresist, polyimides).

### 4.3 Optimization of bonding conditions. Summary of bonding techniques

Gold bonds at the relatively low temperature of 300 °C because it a soft metal, and deforms under pressure. Mass transport between the contacted gold surfaces results in a single uniform gold layer. Several other metals have been used for wafer bonding in a variety of applications, and were initially considered for the microstrip laser. These include palladium and indium, a common solder. Palladium fuses with GaAs and InP at a low temperature of about 350 °C, and has been used to

fabricate *pin* diodes [2]. As in the case of gold, the palladium bond with the semiconductor is metallurgical in nature. A microstrip laser could be made by evaporating palladium on a gold covered wafer, and then bonding to an InP substrate. This type of bonding was not attempted however, since the process is very sensitive to surface conditions [4] - palladium is a harder metal than gold - and surface defects or particles much more easily degrade the quality of the palladium bonded wafer than they do for gold bonded wafers. The process latitude for gold bonding is much greater, resulting in higher reliability and reproducibility.

Using indium solder as a bonding medium is impractical, because indium melts at 156 °C [5], precluding any high temperature processes after bonding. The advantage to such a process, if it could be used, is that it compensates for poor surface morphologies by filling the gaps caused by imperfections. However, since the ridge laser process requires a silicon nitride deposition at 250 °C, polyimide curing at 240 °C, and annealing ohmic contacts at temperatures close to 400 °C, indium solder bonding is not a viable method. There are other problems also: the InP ridge is etched in hydrochloric acid (HCl) which also etches indium, and the bonded layer would therefore be attacked during the ridge etch.

Considering the options available, the best possible bonding material is a metal that flows at the temperatures above those used in the fabrication procedures, and that does not get attacked by any of the etches used. While a bonding metal meeting these conditions was not found, gold is a reasonable approximation to it: it is soft and deforms to partially accommodate surface imperfections, and is sufficient for high temperature processing up to about 400 °C.

Several factors other than surface quality and the actual bonding mechanism and metal were necessary to consider in developing the process used for the microstrip laser. Bonding two wafers with an intermediary metal between them is different from directly fusing two semiconductors [3, 6, 7], because adhesive forces between the evaporated metal and the semiconductor can also affect the quality and ultimate durability of the bond. The gold-gold bond is much stronger than the adhesive bond between the metal and the semiconductor. Because of this, opposing stresses in the wafer can cause the metal to pull off the semiconductor, as is shown in the SEM photograph of Figure 5. An excellent gold bond is useless if it fails to connect the two wafers together.

The metal with the best adhesion to semiconductor must therefore be chosen as the first evaporation layer. A few metals are commonly used as sticking layers because of their excellent adhesiveness. These include chrome (Cr), titanium (Ti), and nickel (Ni). Bonding experiments were done with all these metals as sticking layers, and chrome was determined to be the most effective. Ti and Cr are both effective because they actively seek out oxygen and react with any native oxide on the surface. Following that, a low stress metal must be used to avoid peeling. The bond was tested by cleaving a bonded wafer with the substrate removed, as in the real laser process, and then scanning the bonded interface with the SEM. Several cross sectional cleaves representative of the entire wafer were scanned to determine

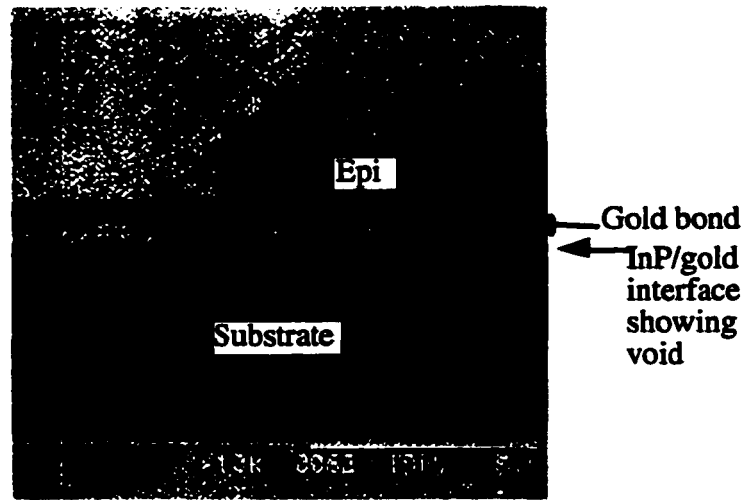


Figure 5. Microstrip laser in which the bonded gold has separated from the lower InP substrate.

the bonding efficiency shown in the table. Titanium and chrome both produced good gold bonds, but chrome proved superior for adhesion to the semiconductor. Using nickel as a sticking layer resulted in poor bonding. This was most likely caused by the absence of a platinum blocking layer. Platinum could not be evaporated after the nickel due to evaporator constraints, and venting the chamber midway through the evaporation to change sources was not attempted, to avoid oxidizing the nickel. Significant amounts of gold diffused into the semiconductor, thus ruining the bond. Since the bond was poor, adhesion to the semiconductor was not a problem, but not of particular relevance either. Table 1 presents several different metal sequences and the bonding efficiency and adhesion of each. All bonding runs listed in the table were performed for 4 hour at 300 °C.

The platinum layer, as discussed above, was chosen for its diffusion blocking properties. As in a metal contact, a gold layer subject to high temperatures

Bonding metals	Thickness sequence (nm)	Bonding efficiency	Adhesion efficiency
Ti/Pt/Au	50/1000/5000	95%	60%
Ni/Au	150/5000	10%	-----
Cr/Pt/Au	75/1000/5000	95%	80%

Table 1. Different bonding metal sequences tested. All tests were done for 4 hours at 300 °C.

will diffuse into the semiconductor. This kind of spiking can degrade the contact and the material quality - in a laser, for example, spiking into the cladding layers can cause very high optical loss due to free carrier absorption. Also, gold spiking through the bottom p layer into the n layer shorts out the diode and ruins the device. In addition to degrading the material, spiking from the bonded layer also can ruin the bond quality - voids are created in the bonding region from where gold has diffused out. Since a rapid increase in gold diffusion occurs around temperatures above 400 °C - the temperature at which contact annealing is done and is necessary for the fabrication process - a good blocking layer is required. Several experiments were done with different platinum thicknesses. While very little can be done to prevent the gold from spiking at temperatures significantly above 410 - 420 °C, 100 nm of platinum does successfully block the diffusion at temperatures below that. With less platinum than this, the maximum temperature is reduced below 400 °C. SEM photographs of a bonded laser annealed at 380 °C for 30 seconds with only a 22.5 nm platinum diffusion block shows significant spiking of gold from the bonded layer. This is shown in Figure 6 (a). 100 nm of platinum, however, works much better, and is sufficient for temperatures up to about 410 °C. A laser with this much platinum that was annealed at 410 °C for 30 seconds is shown in Figure 6 (b).

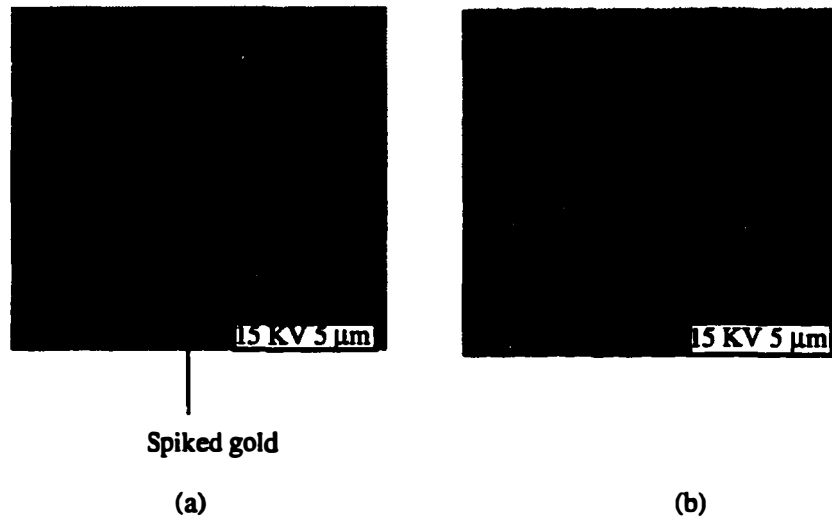


Figure 6. (a) Microstrip laser with 22.5 nm platinum blocking layer annealed at 380 °C for 30 seconds. Note the gold spiking from the bonded layer. (b) Microstrip laser with 100 nm platinum blocking layer annealed at 410 °C. No spiking is seen.

A series of experiments was also done to determine the optimum temperature, pressure, ramp rate, and bonding time. The final conditions decided upon, 300 °C for 4 hours, 1 °C/minute ramp up and ramp down rate, and 0.65 in-lbs setting on the torque wrench, were described previously. Temperatures between 250 °C and 350 °C were tested: 250 was found to be too low for adequate bonding, and 350 °C, while satisfactory, gave the same results as 300 °C. 300 °C was chosen for the process because the ramping time is less. Also, since the bonding cycle is very long, a lower temperature process is less likely to degrade the quality of the laser material by metal, semiconductor or dopant diffusion.

A final temperature test was done to determine whether the long bonding cycle degrades the laser material at all. Two broad area laser samples were fabricated: one sample, prior to fabrication, was cycled through the temperature

process used during bonding, and the other was fabricated without any temperature pre-treatment. The threshold current properties are the same, indicating that the 300 °C temperature cycle does not cause any material degradation.

#### **4.4 Substrate removal**

Following bonding, the original substrate on which the epi wafer is grown must be removed to expose the inverted laser epitaxy used to fabricate microstrip lasers. The InP substrate is etched in a 3:1 hydrochloric acid (HCl): H<sub>2</sub>O solution. To ensure uniform etching, the solution is stirred with a magnetic stirrer bar at 300 rpm. About 350 μm of InP must be etched, making the stirring essential. The etch takes about 40 minutes. Since the semi-insulating InP substrate bonded to the laser epi is also etched by HCl, a silicon wafer is attached to it with wax to protect it. The HCl etch stops on a doped InGaAs layer, leaving a smooth 3 μm film of laser epi on top of the gold. The doped InGaAs layer now is the top contact layer for the wafer.

#### **4.5 Fabrication of ridge waveguide lasers**

Table 2 outlines the steps followed in fabricating ridge waveguide microstrip lasers. The process is either 4 or 5 mask levels, depending on whether the stripe that defines the ridge is dielectric or metal. A metal stripe serves as an etch mask and as an ohmic metal to the ridge, thus eliminating one mask level. An annotated schematic of the ridge waveguide laser is shown in Figure 7. These devices are fabricated with 300 μm separation between ridges, in order to facilitate high speed probing - a ground-signal-ground probe with 150 μm pitch (signal to ground

distance) can be conveniently used with this geometry. High speed probes with narrower pitch can be ordered, but  $150\ \mu\text{m}$  is most common. A metal stripe created by liftoff was initially used as the etch mask; later, the process was changed to one using a silicon nitride ( $\text{SiN}_x$ ) mask, because this process results in smooth, vertical sidewalls on the ridge. The smooth sidewalls are desirable for low waveguide optical loss. The details of the photolithography processes used for transferring patterns from mask to wafer are documented in Appendix A.

Level 1	Level 2	Level 3-skip if level 1 uses metal mask	Level 4	Level 5
Stripe definition ↓ Ridge etch	Polyimide patterning ↓ Polyimide etchback	Evaporate top ohmic ↓ Anneal top contact.	Wide mesa definition ↓ Etch to bonded metal	Evaporate thick metal ↓ Lap & apply back contact

Table 2. Mask level and process sequence for microstrip laser fabrication.

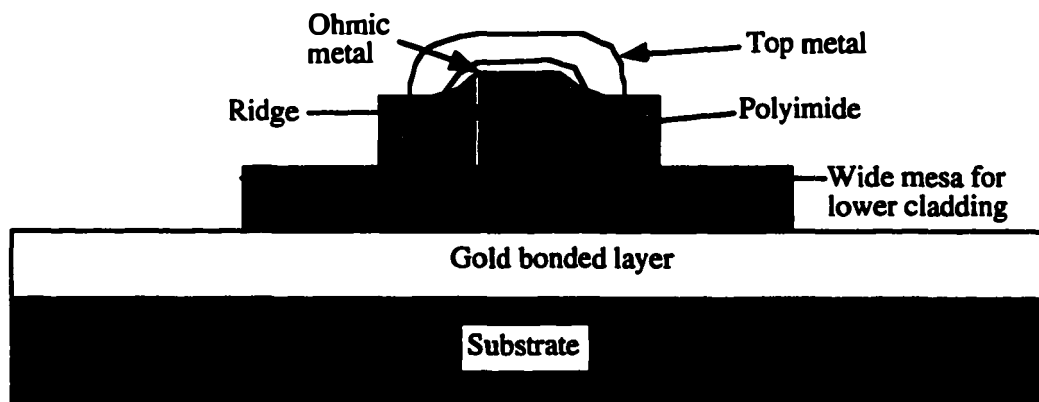


Figure 7. Cross sectional schematic of ridge waveguide microstrip laser.

The ridge can be formed by wet chemical etching or by reactive ion etching (RIE), or a combination of both [8, 9]. For etching the InP cladding, the wet etch is

preferable, since it is simpler to set up and execute, and gives very smooth sidewalls; sidewall roughness in the wet etch is caused solely by edge roughness in the mask that transfers to the ridge. This edge roughness often comes from the initial photoresist lithography and development. A few things can be done to minimize this. These include careful contact lithography, proper development time (underdevelopment can leave photoresist scum at the sides and overdevelopment can undercut the photoresist), and an oxygen plasma descum following development. Poor liftoff, if a metal mask is used, will cause very rough edges on the metal that transfer to the ridge. Careful and patient execution of these steps results in very smooth edges, and smooth sidewalls in the wet-etched ridge.

RIE, on the other hand, will produce some sidewall roughness even if the mask is perfectly smooth. There are two other reasons wet etched ridges are preferable in the InP/InGaAsP system. First, HCl etches InP but it does not etch InGaAsP or InGaAs. Because of this, the wet etch is highly selective and ensures excellent uniformity of etch depth. Also, the InGaAs contact layer is not undercut at all. A second advantage is that HCl etches InP crystallographically and proper orientation of the ridges along the [001] direction produces straight sidewalls. Figure 8 (a) shows an SEM photograph of a wet etched InP ridge in which the mask has been incorrectly oriented. Orienting the ridges along the orthogonal direction causes the sidewalls to slope outwards at an angle of  $60^\circ$ . This is to be avoided when fabricating narrow ridge devices, because the large slope angle generates a wide ridge at the base, undermining the goal of tight carrier and photon confinement. A quick trigonometric calculation shows that a ridge  $1.2\ \mu\text{m}$  high (a typical height for our structures) and  $2\ \mu\text{m}$  wide at the top is  $6\ \mu\text{m}$  wide at its base, as is consistent

with the the photograph in 8 (a). Figure 8 (b) shows a picture of a wet etched ridge for which the wafer orientation was correct.

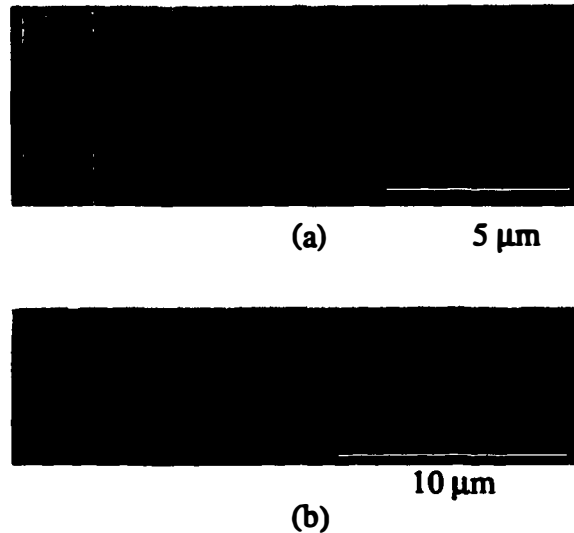


Figure 8. Wet etched InP ridges. (a) Sloping sidewalls caused by incorrect ridge orientation. (b) Straight sidewalls. The ridge is oriented along the [001] direction.

Metal liftoff for stripe definition is appealing, because it incorporates the stripe definition and the evaporation of the ohmic metal in one mask step. The drawback is that because of electrochemical effects, straight sidewalls aren't produced by a wet etch even if the stripes are oriented along the [001] direction. Any oxidizing metal present in the mask provides the necessary electrochemical potential to etch along other crystal planes, besides the [001]. This means that if a metal mask is used and narrow ridges are desired, the etching must be done by RIE.

For wide ridge fabrications, for example, 10 μm and greater, the liftoff process followed by RIE is preferable, because the rougher sidewalls have minimal

effect on the optical loss (the fraction of the mode scattered at the sidewalls is very small relative to a narrow ridge) and one less mask level is required. For narrow ridge fabrications, the preferable process involves the plasma deposition of about 80 nm of  $\text{SiN}_x$  at 250 °C, followed by patterning with standard photolithographic techniques. The  $\text{SiN}_x$  becomes the stripe defining mask, and the wet etch gives the straight sidewalls seen in Figure 8 (b).

#### 4.6 Broad area laser fabrication

The fabrication of wide ridge lasers is a relatively simple process. Broad area lasers with 50  $\mu\text{m}$  ridges are fabricated by metal liftoff and wet etching and are used for material characterization. Threshold current density, internal efficiency, and gain properties of the material can all be determined from broad area laser results. Standard photolithography is used to define 50  $\mu\text{m}$  wide spaces in a photoresist layer. Since almost all the wafers grown are p-up, a p-contact metallization of 20 nm of titanium, 75 nm of platinum and 200 nm of gold is electron-beam evaporated onto the surface. Liftoff is performed in acetone, and 50  $\mu\text{m}$  wide metal lines with 150  $\mu\text{m}$  center separation are left on the wafer. Prior to evaporation a 20 second  $\text{O}_2$  plasma descum is done (see Appendix A for details) to remove resist scum and to better define the sides of the resist pattern. A 20 second dip in 1:15  $\text{NH}_4\text{OH}:\text{H}_2\text{O}$  solution is also done to remove the surface oxide on the InGaAs. The 100 nm InGaAs cap layer is wet etched in a 1:1:50  $\text{H}_2\text{O}_2:\text{H}_2\text{SO}_4:\text{H}_2\text{O}$  solution. This etch takes about 1 minute. The InP cladding is then etched in a 3:1  $\text{HCl}:\text{H}_2\text{O}$  solution for about 30 seconds to a minute, until all the InP is removed.

The finished etch is confirmed by surface inspection and DEKTAK measurement of the ridge heights.

The substrate is lapped to a thickness of 80-100  $\mu\text{m}$ , and a backside metal contact of 5 nm of Nickel and 200 nm of gold is evaporated in a thermal evaporator. The sample is now ready for cleaving and testing.

The broad area laser fabrication process is purposely made as short and simple as possible, with steps such as the contact anneal skipped. The annealing is skipped because it is not really necessary - the ridges are very wide already, contributing to a low resistance, and further, broad area lasers are only operated in pulsed mode, with duty cycles on the order of 0.1%. Because of the low duty cycle, a slightly higher resistance does not cause heating of the active layer. Also, the backside n-contact of Ni/Au is not the best n-contact; typically, germanium (Ge) is included for an n-contact since it dopes the semiconductor. The Ge is usually evaporated from a Au-Ge source at the eutectic composition. Because the backside contact is very large, typically several hundred microns by a few millimeters, and because just about any metal makes an acceptable ohmic contact to n-InP, the simple Ni/Au metallization is chosen for expedience. The Au-Ge contacts must be done in the e-beam evaporator, which has a significantly longer pump down time than the thermal evaporator, and much heavier usage that often requires a wait of several days.

#### **4.7 Microstrip broad area lasers**

One process run was done in which the 50  $\mu\text{m}$  broad area lasers were fabricated on microstrip wafer. This was done to determine whether any material

degradation was occurring as a result of the gold bonding process. The results from this experiment are presented in Chapter 5. The microstrip broad area process is similar to the conventional broad area laser process described above, with a few differences. First, the ridge metallization is changed to a sequence of 5 nm Ni, 100 nm AuGe eutectic, 15 nm Ni, and 200 nm gold. This is done because the epi inversion intrinsic to the bonding and substrate removal process results in an n-contact layer. Second, the wafers are bonded to semi-insulating InP, so a backside contact could not be made. Instead, a second mask step was performed in which 50  $\mu\text{m}$  wide spaces were opened symmetrically around the ridges; the pitch of the laser mask was 150  $\mu\text{m}$ , leaving an 100  $\mu\text{m}$  space between the sides of adjacent ridges. The structure is similar to that of Figure 7, except there is no polyimide surrounding the ridge and no overlay metal evaporated above the ohmic metal. Using photoresist as the etch mask to protect the ridges, the InGaAsP SCH and active region, the p-InP bottom cladding, and the p<sup>+</sup> InGaAs contact layer are all removed. The InGaAsP is etched in a hydrogen peroxide - sulfuric acid solution mixed in a 8:1:1 H<sub>2</sub>O<sub>2</sub>:H<sub>2</sub>SO<sub>4</sub>:H<sub>2</sub>O ratio. Because of the high peroxide concentration, the solution etches any quaternary composition very quickly. The etch takes about a minute. The InP bottom cladding is etched in 3:1 H<sub>3</sub>PO<sub>4</sub>:HCl. This etches InP relatively slowly, about 500 nm/minute when agitated, and is used because it is a less aggressive, more controlled etch than a concentrated HCl: H<sub>2</sub>O solution used for substrate removal or ridge etching. HCl attacks the photoresist etch mask; a very strong solution can completely destroy the mask quickly, so it is better to use the slower etch and monitor the mask integrity at time intervals of 1 or 2 minutes. Typically about 10  $\mu\text{m}$  of the mask is attacked from the side during the etch, a

tolerable amount that does not degrade device performance. The total etch time is about 3-4 minutes. The etch is strongly diffusion limited, because of the high viscosity of the phosphoric acid, and therefore strong agitation is needed to ensure continuous etching. Bubbles also form at the surface of the wafer as part of the reaction between the HCl and the InP, and these can further block etchant from getting to the surface. It therefore helps to remove the wafer from solution and rinse with water when it appears that the surface is blocked by the bubbles. Agitation and rinsing are critical because of the limited lifetime of the photoresist mask in HCl. If the etch comes to a stop while the sample is still in solution, the photoresist still can degrade - the fact that the semiconductor isn't etching, or is etching very slowly, does not also mean that the photoresist is not being attacked - and if the degradation goes too far, the device will be ruined, as shown in the extreme case of Figure 9. Note that the wavy lines that come very close to intersecting the narrower ridge that should be centered between the broader mask. This particular device was a 10  $\mu\text{m}$  ridge laser, not a broad area laser, and almost 50  $\mu\text{m}$  of the photoresist mask was attacked from the side during the etch.

The InGaAs  $p^+$  contact layer is removed in 1:1:50  $\text{H}_2\text{O}_2:\text{H}_2\text{SO}_4:\text{H}_2\text{O}$  solution. This etch takes about a minute. The surface changes colors during the process, and when no more color changes are observed, the etch is finished. The chrome layer is now exposed and can be probed as the p-side contact. The wafer is thinned to 80-100  $\mu\text{m}$  in order to facilitate cleaving, and a backside metallization is done. Although the backside metallization serves no electrical purpose because the substrate is semi-insulating, a Ni/Au backside metal is useful if the device is to be mounted on a stud. The typical mounting solder is lead (Pb)/ tin (Sn)/ silver (Ag)

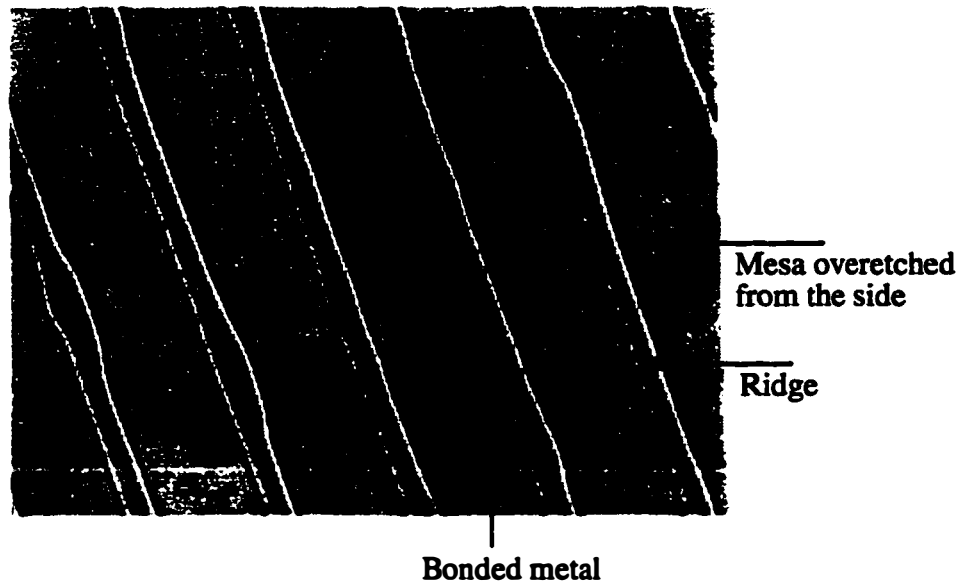


Figure 9. A process run in which the broad photoresist mask for protecting the ridges was badly attacked during the etch to the bonded metal layer.

which dissolves in gold above the melting point. The gold layer is therefore necessary for good solder mounting.

The chrome from the bonded metal can also be removed in a chrome etchant or in a 8:1:1  $\text{H}_2\text{O}_2:\text{H}_2\text{SO}_4:\text{H}_2\text{O}$  solution, although it is not necessary, particularly for broad area lasers. If an extremely low resistance is needed, removal of the chrome layer is recommended, since it strongly oxidizes in air. Removal of the chrome layer exposes the platinum layer below it, which does not oxidize. A gold layer is then evaporated above the platinum for probing. Evaporating the extra gold layer is important because high frequency probes should ideally contact a soft metal like gold, rather than a hard metal like platinum. For good contact, the probes are driven forward slightly into the contact, and this is better done with the soft metal.

#### **4.8 10 $\mu\text{m}$ ridge laser fabrication. RIE etching conditions**

10  $\mu\text{m}$  wide ridge lasers were also fabricated. The 10  $\mu\text{m}$  ridge lasers offer a compromise between the simplicity of the broad area laser process and the usefulness of the narrow ridge lasers, described in the next section. The simple 50  $\mu\text{m}$  ridges described above are too wide to operate continuous wave (cw), or at reasonable current levels. Thus their usefulness is restricted to materials characterization as discussed above. The narrow ridge laser process described below is very involved, and can take up to two weeks to fully complete. 10  $\mu\text{m}$  ridges can be quickly processed and probed directly, and can run cw at reasonable threshold currents. They therefore proved to be a useful intermediary device for characterization of the microstrip laser.

The process differs from the broad area microstrip laser process only in the ridge etching. As in the broad area lasers, the stripe is defined by metal liftoff, but the etch is done by RIE rather than by wet etching. An additional 30 nm layer of Ni is evaporated above the gold and serves as the RIE etch mask. Gold should not be used as a mask because it sputters during the plasma etch. RIE is performed because the 10  $\mu\text{m}$  stripes are narrow enough so that undercut of the contact layer can be significant, affecting the electrical resistance and the final ridge width. The outwardly sloping sidewalls that result from the wet etch of the InP also can have a small, but noticeable effect on the laser operating characteristics. At the same time, the somewhat greater sidewall roughness one obtains from RIE only has a minimal effect on optical loss in the wide ridge.

The RIE etch is done with a mixture of methane, hydrogen and argon (MHA) gas. The methane and the hydrogen are the necessary etch reactants, while the argon continuously sputter cleans the surface to minimize an accumulation of the reaction products there. The gases are mixed at flow rates of 4, 20, and 10 sccm respectively at a pressure of 75 mTorr. Before being filled with the gas mixture, the chamber is pumped down to a pressure of approximately  $2 \cdot 10^{-5}$  Torr. The gases are ionized and the plasma is formed by applying 500 volts between the cathode and anode. The electric field accelerates the charged ions towards the wafer, etching the InGaAs at approximately 30 nm/minute, and the InP at about 90 nm/minute. The etch is stopped about 200 nm above the active region, and the final 200 nm of InP is removed in the 3:1 HCl: water solution. The etch is stopped before the active region to prevent accidental overetching into the active region, and to minimize RIE radiation damage to the active region caused by bombardment of the high energy ions. For an 100 nm InGaAs cap and a 1.2  $\mu\text{m}$  InP cladding layer, the total etch time is about 15 minutes. The sample is removed from the chamber at 6 minute intervals and the ridge heights are measured in the DEKTAK. This is done to monitor the etch progress and to calibrate the etch rate.

The methane-hydrogen RIE is equipped with a Helium - Neon laser, a photodetector, and a computer program that monitors the photodetector signal versus time. An unpatterned piece of epi (from the same wafer used for the fabrication) can be placed in the etch chamber with the real sample, and the laser can be reflected off it. As the InGaAs layer is etched and becomes thinner, the interference between the two reflected beams - one from the InGaAs and one from the InP cladding - shows up as an oscillation in the signal versus time. When all the InGaAs has been

removed, a flat signal is observed, until the etch approaches the InGaAsP active region, at which time the etch can be stopped. Figure 10 shows the photodetector signal versus time for a long etch which goes all the way through the InP cladding and the active region.



Figure 10. Reflected He-Ne signal versus time from an InP laser wafer. Interference between the different semiconductor layers are clear.

The laser monitor isn't used because the microstrip laser epi is inverted, and a sample piece of inverted epi is not readily available. The timed etch, checked at regular intervals is very reliable by itself.

Following the ridge etch, the bottom p-contact must be exposed so that the devices can be probed and tested. The bonded layer p-contact is exposed by masking the ridges with a 50  $\mu\text{m}$  wide pattern of photoresist, and wet etching to the chrome layer, using the same process as for the microstrip broad area lasers. The

device is then thinned and backside metal is evaporated. These devices are ready for testing.

#### 4.9 Narrow ridge fabrication

As discussed above, if wet etching can be used to make narrow ridges, it is the preferable process, resulting in smoother sidewalls and lower optical loss. Because of the problems associated with fabricating wet etched straight sidewalls with a metal mask, silicon nitride ( $\text{SiN}_x$ ) is used as the etch mask. 80 nm of  $\text{SiN}_x$  is deposited on the wafer by plasma enhanced chemical vapor deposition (PECVD) at 250 °C. A piece of silicon is included in the chamber during deposition. This is done because the index and thickness of the deposited film on silicon can be easily measured with an ellipsometer, while an accurate measurement on a wafer consisting of several layers of different materials is virtually impossible. As long as the index of the  $\text{SiN}_x$  is above 1.9, the process is continued. If it is below this, the nitride is stripped and redeposited, since the lower index most likely indicates contamination with silicon oxide ( $\text{SiO}_2$ ), for which the PECVD chamber is also used.  $\text{SiO}_2$  etches in HCl, ruining the mask and the device during the wet etch. Prior to the  $\text{SiN}_x$  deposition, the chamber must be cleaned for about 60 minutes by the standard  $\text{SiN}_x$  cleaning program loaded into the computer.

Following the successful  $\text{SiN}_x$  deposition, a photoresist mask is patterned above the wafer (appendix A) with narrow photoresist stripes covering the layer of  $\text{SiN}_x$ . Carbon tetrafluoride ( $\text{CF}_4$ ) plasma etches  $\text{SiN}_x$  but does not etch photoresist, and is therefore used to etch away the  $\text{SiN}_x$  not protected by the photoresist. Prior to etching the  $\text{SiN}_x$ , a 20 second oxygen descum (300 mTorr, 100 watts) is

performed to clean up the photoresist edges. The  $\text{CF}_4$  etch is done in the PEIIA plasma etcher in the cleanroom under conditions of 300 mTorr pressure and 200 watts incident power. 1 minute is sufficient to remove all the unmasked  $\text{SiN}_x$ . The photoresist is then washed off in acetone and narrow stripes of  $\text{SiN}_x$  are left on the wafer as the etch mask.

Before etching the InP cladding, the 100 nm InGaAs contact layer must be removed. This etch is done in the RIE to prevent a large InGaAs undercut that happens in a wet etch. The RIE etch is done for 6 minutes with the same flow rate and pressure conditions that are used for the 10  $\mu\text{m}$  ridge lasers described previously. 6 minutes is enough time to remove all the InGaAs in the unmasked region. In addition, about 100 nm of InP is etched during this time. The overetching is done to ensure that all the InGaAs is etched away; the small amount of InP removed does not have a major impact on the quality of the ridge waveguide compared to a fully wet etched InP ridge.

On surfaces where the methane - hydrogen mixture does not etch, it forms polymer. Most dielectrics, such as  $\text{SiN}_x$ , are not etched by this plasma chemistry. The mask selectivity for the etch is for all practical purposes infinite and polymer therefore deposits on the mask during the etch. These deposits are easily removed in an oxygen plasma generated in the same chamber following the semiconductor etch. The conditions for the  $\text{O}_2$  plasma are a gas flow rate of 50 sccm, 125 mTorr pressure, and 200 volts between the plates. 2 minutes  $\text{O}_2$  plasma under these conditions is sufficient to remove all the polymer deposited.

The InP cladding is then wet etched in a 3:1 HCl:  $\text{H}_2\text{O}$  solution. This etch is very fast, finishing in 30 seconds. While the etch stops abruptly on the InGaAsP

SCH layer, it is important not to leave the sample in the solution much longer than that, because some etching does occur in the lateral direction, albeit at a much slower rate than the vertical, and this is undesirable. Figure 11 (a) shows an SEM of a ridge sidewall from the wet etch described above; 11 (b) shows an SEM from an RIE etched ridge. The wet etched ridge clearly has much smoother sidewalls, showing that the wet etch ridge process is preferable.



Figure 11. (a) Wet etched ridge. The ridge sidewall is very smooth. (b) RIE etched ridge. The sidewall is rough.

Following each etch step (the RIE etch and the wet etch), the ridge heights are scanned with the DEKTAK to ensure that the etch is completely finished. A mirror smooth surface layer is also a good indicator of a finished etch. This is because the HCl etch tends to be nonuniform and leaves a rough surface if stopped before completion. In contrast, the completed etch exposes the perfectly smooth top monolayer of InGaAsP.

As discussed in Chapter 3, it is imperative that n-ridges be etched at least through the upper SCH and the active region to avoid large lateral leakage currents that cause high thresholds and low efficiencies. Some difficulties are associated with the active region etch, and an ideal etchant does not exist. A mixture of sulfuric acid ( $\text{H}_2\text{SO}_4$ ), hydrogen peroxide ( $\text{H}_2\text{O}_2$ ), and water ( $\text{H}_2\text{O}$ ) can be used to etch the

quaternary without etching InP, and would thus seem appropriate for etching the quaternary and stopping on the p InP cladding (the active region and the upper and lower SCH would be etched). However, the etch rate of this solution strongly depends on phosphorus composition, increasing as the amount of phosphorus decreases. This creates two problems. First, InGaAs etches much faster than the quaternary, and the cap layer will be completely undercut in the time required to etch through the quaternary. Second, even if the InGaAs cap could be sacrificed, which is not unfeasible because good ohmic contacts can be made to n-InP, the phosphorus content of the quantum wells is significantly smaller than that of the barriers and the SCH. As a result, the quantum wells are completely undercut and lifted off during the etch, rendering it useless.

Reactive ion etching with the methane - hydrogen chemistry discussed above would seem to be promising, because RIE allows for accurate control of the etch depth, straight sidewalls and no undercut, excellent reproducibility, and excellent uniformity - characteristics usually not associated with wet chemical etching. However, the bombardment of the wafer with high energy ions may damage the material, causing increased sidewall recombination and higher thresholds. On the other hand there is also some evidence that the  $H_2$  in the  $CH_4/H_2$  mixture may passivate defects also.

Because of the potential problems with RIE etching of the active region, a wet etch for quaternary that does not severely undercut the ridge can be used. Since some undercut is unavoidable, the etch rates for varying compositions of InGaAsP, InP, and InGaAs should be comparable so that the undercut is fairly uniform. Saturated bromine water (SBW) mixed with Phosphoric acid ( $H_3PO_4$ ) and  $H_2O$  is a

good mixture for this purpose. The SBW, as the name indicates, is bromine that is saturated in an aqueous solution at room temperature. Another point to note is that the etch is diffusion limited. Because of this, the etch rate varies with ridge width, being slower near the narrower ridges. Etchant spills off the top of the ridge mask, and etches the surrounding region; replenishing the etchant is a slower for narrow ridges thus the etch rate is lower there. Agitating the etch solution helps, but 10  $\mu\text{m}$  wide ridges tend to etch 50% - 100% faster than narrow 2  $\mu\text{m}$  ridges.

A 2:1:15 SBW:H<sub>3</sub>PO<sub>4</sub>:H<sub>2</sub>O solution is used for etching through the quaternary. Because bromine has a very high vapor pressure the solution depletes very quickly and the etch rate drops. To avoid this, a large amount of the etchant is mixed and kept in a sealed flask. For every minute of etching, the solution in the open beaker where the etch is done is disposed of and replaced with fresh solution from the sealed flask. The etch rate is very sensitive to temperature and concentration conditions, and so after each minute of etching, the wafer surface is thoroughly examined under the DEKTAK to determine an approximate etch rate. The etch rate observed for all ridges has been seen to vary from anywhere between 30 nm/minute (for narrow ridges) to 150 nm/minute (for wide ridges), with the maximum etch rate for narrow ridges being about 100 nm/minute, and the minimum etch rate for wide ridges being about 70 nm/minute. Such a large variation does not typically occur within the same run however; the etch time ranged from 3 to 8 minutes depending on the conditions. There is always some nonuniformity across the wafer after the etch is stopped, the maximum being about 100-150 nm.

The SBW etch does undercut the wafer, about the same amount that it etches vertically. Since about 300 nm of material is being etched, the 1  $\mu\text{m}$  ridges are

pretty much ruined in the process, but those wider than that still remain intact, albeit slightly narrower than were originally planned. An SEM photograph of a  $2\ \mu\text{m}$  ridge with a stained active region is shown in Figure 12 (a); it is clear the ridge is etched past the active region. The sample was stain etched in  $1:1:50\ \text{H}_2\text{O}_2:\text{H}_2\text{SO}_4:\text{H}_2\text{O}$ . Figure 12 (b) shows what had been a  $1\ \mu\text{m}$  ridge - the ridge is still intact at the base, but is impractically narrow at the top.

After the etch is finished, the  $\text{SiN}_x$  mask is removed in a carbon tetrafluoride ( $\text{CF}_4$ ) plasma and the bare ridges are exposed.

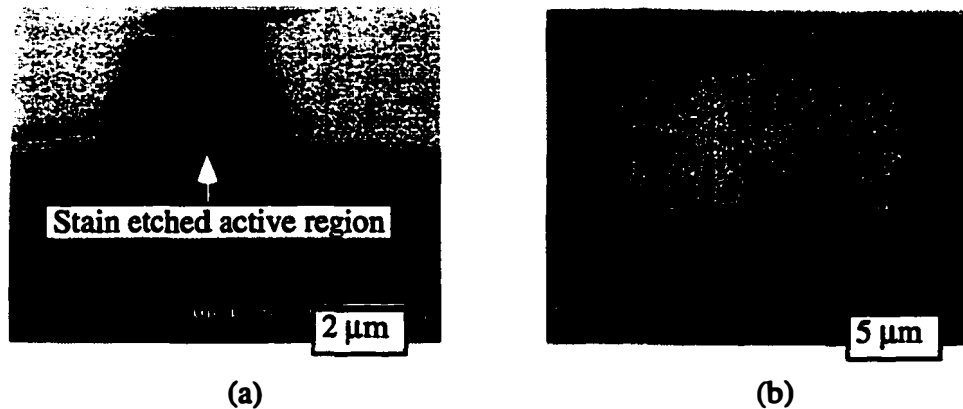


Figure 12. SEM photographs of ridges etched through the active region with saturated bromine water. (a) is a  $2\ \mu\text{m}$  ridge with the active region stained, showing a complete etch. (b) is a  $1\ \mu\text{m}$  ridge, almost completely undercut by the etch.

#### 4.10 Polyimide planarization

The narrow ridges must be surrounded with solid material to facilitate device probing and testing: a  $2\ \mu\text{m}$  ridge, for example, cannot be conveniently probed without destroying the ridge. Further, in the narrow ridge process described above, the ridge is initially formed without any ohmic metal above it, and a practical procedure for putting down metal on the ridge without shorting it to the active region

or bottom cladding is needed. This can be accomplished by spinning and curing polyimide on the ridge, patterning it, and etching it back to a height that just exposes the ridge surface. A metal layer can then be evaporated that covers the ridge and has bondpads on the polyimide to facilitate probing and testing. Other dielectrics can be used - for example,  $\text{SiN}_x$  or silicon oxide. The dielectric constant of polyimide is lower and results in a lower capacitance, which is advantageous for high speed devices. Also, it is difficult to deposit the thick layers required for low capacitance if  $\text{SiN}_x$  or  $\text{SiO}_2$  is used, and these films tend to crack and break at thicknesses on the order of  $1 \mu\text{m}$ .

The other option is to do a regrowth that buries the ridge with semi-insulating InP or with doped blocking layers [10-13]. Unfortunately, regrowth is not a viable option for the microstrip laser because of the high growth temperatures ( $>600 \text{ }^\circ\text{C}$ ) required that cause diffusion of the gold from the bonded layer. The diffusion at these temperatures degrades the structural integrity of the bond and can destroy the device by shorting out the diode. A different bonding process could be developed for the microstrip laser in which regrowth is done first, and bonding after.

The polyimide used for the dielectric is Probimide 284. At a rate of 5000 revolutions per minute (RPM), a layer approximately  $1 \mu\text{m}$  thick spins on the wafer. The ridges, including the active region etch, can be up to  $2 \mu\text{m}$  in height; therefore 2 layers of polyimide are really needed for adequate coverage. The polyimide does not perfectly planarize but rather slopes downwardly away from the ridge. Using two layers ensures that the polyimide connects to the top of the ridge at the interface,

rather than breaking off and producing a gap between the ridge and the surrounding polyimide.

The spin-on polyimide is highly viscous, and care must be taken to apply it on the wafer surface uniformly and without air bubbles. Typically it is dripped on from a medicine dropper, although it can be applied with a syringe and a 1  $\mu\text{m}$  filter to better guarantee uniformity and absence of contaminants. The viscous polyimide solidifies at elevated temperatures, as the polymer chains cross link and form a hard glassy substance. Complete cross linking occurs in the vicinity of 300 °C, but if necessary, sufficient solidification can be achieved at lower temperatures.

Before application of the second layer, the first layer is partially cured so as to prevent intermixing. The partial curing is done as follows: 90 °C for 30 minutes, ramp at 5 °C/minute to 170 °C, and hold for 40 minutes. The second layer is then spun on at 5 K RPM, and a higher temperature cure, up to 240 °C is performed. Although the temperature is lower than that recommended for complete cross linking of the chains, the polyimide cures well enough that no practical difference are observed. This process was chosen to minimize high temperature effects in the process that could affect the bond integrity.

The planarization with the two layers is not perfect; deviation from planarity is easily measured on the DEKTAK. The surface profile of the polyimide is dependent on surface topography, and a slightly thicker layer forms over wider regions. Because of this, in our devices, a hillock of polyimide about 800 nm thick forms above the 10  $\mu\text{m}$  ridges, whereas the narrower ridges (5  $\mu\text{m}$  and less) show hillocks of only about 500 nm.

Since the polyimide does not perfectly planarize, two additional layers of photoresist are spun on to improve the planarization. First, approximately 3  $\mu\text{m}$  of AZ4330 resist is spun at 6 K. The wafer is heated on a hot plate for 10 minutes at 50 °C, after which the temperature is increased to 100 °C and held there for about 3 minutes. This bake is done because a second layer of photoresist, 2  $\mu\text{m}$  of AZ4210, is spun on after the first to further improve the planarization. The 4330 must be hardened enough to prevent intermixing. With two coats of resist, the planarization is almost perfect, with less than 200 nm deviation for the wide ridges and less than 100 nm for the narrow ridges.

The excellent planarization is required for the etch back process, in which the photoresist and the polyimide are etched back just enough to expose the top of the ridge. Without good planarization, a significant step height results between the ridge top and the surrounding polyimide. This is detrimental to the process, since a large step can cause the metal evaporated onto the ridge and the polyimide to break at the ridge-polyimide interface, resulting in open circuits (the bond pad region is over the polyimide, and should connect to metal on the ridge) or high resistance. A few thousand angstroms, to a maximum of about 500 nm, is acceptable, and a thick metal layer can accommodate a step of that height. But bigger steps will damage the metallization.

Prior to the etch back, the photoresist is patterned. Too much polyimide on the surface interferes with high cleave yield, so a patterned surface that minimizes the total polyimide is preferable. The resist covering the polyimide to be removed is exposed and developed out; all of this exposed polyimide is etched away during the etch back. The dimensions of the patterned polyimide are 50  $\mu\text{m}$  wide around the

ridge, with pads 65 by 65  $\mu\text{m}$  on a side onto which metal bondpads will be evaporated.

The etch back is done in an  $\text{O}_2$  plasma in the load locked RIE #1. The  $\text{O}_2$  plasma etches photoresist and polyimide at almost the same rate. This machine is used only for chlorine and oxygen and is one of the cleaner plasma systems available for use. The background pressure of the chamber is low - about  $10^{-6}$  Torr - and with oxygen flowing, a pressure of 10 mTorr and a flow rate of 7.5 sccm is maintained. The low pressure helps to maintain uniform plasma conditions in the chamber, thus increasing the uniformity of the etch across the wafer. The lit plasma is maintained with a voltage of 350 volts across the plates and an incident power of about 60 watts. The etch is calibrated, and takes 73 minutes to expose ridges about 1.9  $\mu\text{m}$  high. A Helium-Neon laser monitor is also used to monitor the etch. The He-Ne beam reflects from an unpatterned silicon wafer coated with the same 2 layers of polyimide and 2 layers of photoresist used on the laser sample. The reflected signal is measured with a photodetector, and 31 oscillations of the reflected signal indicate that the etch should be ended.

The plasma etch in the RIE usually stops slightly before the ridges have been completely exposed. This is to make sure that the sample is not etched too much. To completely clear the ridge surfaces, additional etching is done in the PEII-A plasma etcher. An oxygen plasma with conditions of 300 mTorr and 200 watts is used to remove the excess. This etches the polyimide at about 100 nm/minute; progress on the etch is checked every minute, until it appears that the ridges are very clear, at which time the etch is checked every 15 or 30 seconds. The progress of the etch is monitored by optical inspection under the microscope. When a thin layer of

polyimide is present above the ridges, multi-colored interference fringes are visible; when the polyimide is all gone, the clear smooth surface of the ridge is apparent. A schematic of the way the polyimide buries the ridge after an etch back in  $O_2$  plasma is shown in Figure 13. DEKTAK is also used to sample various parts of the wafer; whereas a covered ridge still shows a smooth hillock shape, as in Figure 14 (a), the exposed ridge shows an abrupt transition between ridge and polyimide, as in Figure 14 (b), and is a decisive indicator. A successful process run of this kind clears all ridges  $5\ \mu\text{m}$  wide and less. Step heights between ridge and polyimide less than  $50\ \text{nm}$  are obtained. Some of the  $10\ \mu\text{m}$  ridges are not cleared completely of polyimide, and those are sacrificed in the process to preserve the quality of the narrower ridge devices. For those  $10\ \mu\text{m}$  ridges cleared the step heights are less than  $200\ \text{nm}$ .

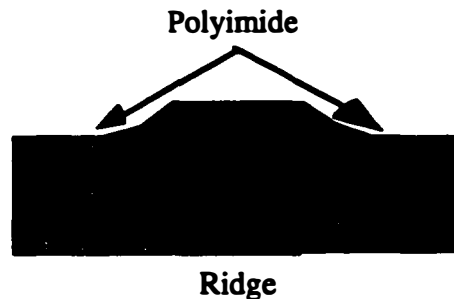


Figure 13. Schematic of how the polyimide buries the ridge after the etch back in  $O_2$  plasma- the polyimide slopes away from the top of the ridge by several hundred nanometers before leveling off.

More details and graphs characterizing the polyimide process are included in Appendix A, Fabrication procedure.

#### 4.11 Ridge metallization

Following the polyimide etch back, the ridge is ready to be metallized. This is completed with a 2 layer liftoff process described in Appendix A. An oxygen

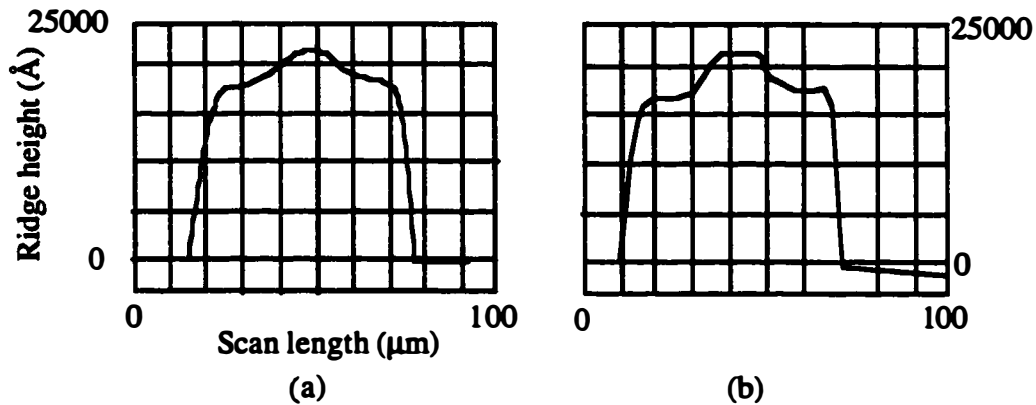


Figure 14. (a) DEKTAK scan of ridge still covered with polyimide. Note the rounded shape of the hillock. (b) DEKTAK scan of ridge clear of polyimide. The hillock shape is not square at the top.

descum is done, and an oxide removal dip in, first, HF:water 1:10, and then  $\text{NH}_4\text{OH}$ :water 1:15. A Ni/AuGe/Ni/Au (5 nm/100 nm/ 15 nm/150 nm) metallization is evaporated in the thermal evaporator, and lifted off to define the metal over the ridge. Following the metallization, the sample is annealed in a strip annealer. The procedure followed involves ramping the temperature up to 300 °C, and holding it there for 30 seconds. Then the temperature is ramped to 380 °C and held there for 20 seconds. As was described in an earlier section, the bonded metal layer can handle this temperature for the short period of time involved. Care must be taken to not allow the temperature to rise too much above 400 °C, as the diffusion is an activation energy process with a characteristic activation temperature in the vicinity of 410 °C.

#### 4.12 Etch to metal layer

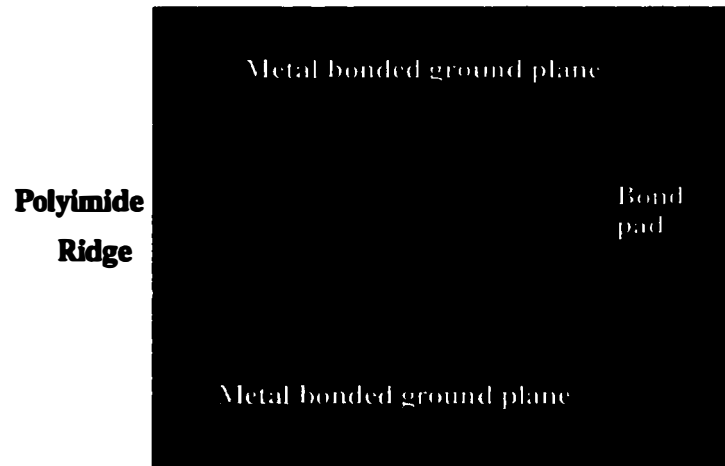
Following the ridge metallization, the bottom contacts must be exposed in order to allow probing of the device. The method for doing this was described

earlier in the broad area microstrip laser section. The ridge and polyimide region is masked with photoresist, and a wet etch is done to get down to the metal layer. The photoresist mask is rectangular, extending 10  $\mu\text{m}$  beyond the boundaries of the patterned polyimide. The strong 8:1:1  $\text{H}_2\text{O}_2 : \text{H}_2\text{SO}_4 : \text{H}_2\text{O}$  etch is still used, to ensure that all the quaternary has been removed, even though the SBW etch had been used to get through the active region. The 3:1  $\text{HCl} : \text{H}_3\text{PO}_4$  is then used to remove the p-InP. A 1:1:50  $\text{H}_2\text{O}_2 : \text{H}_2\text{SO}_4 : \text{H}_2\text{O}$  solution follows to remove the InGaAs, and the HCl is again used to remove the chrome layer. The wafer is checked under the microscope and with the DEKTAK to guarantee that all the semiconductor in the unmasked region has been removed. Typically, a brownish-yellow color indicates exposure of the chrome metal layer.

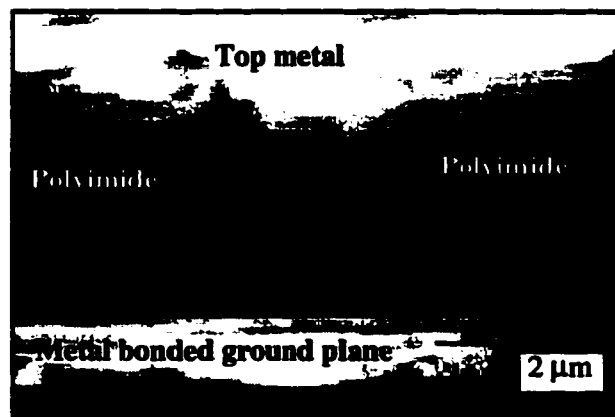
#### 4.13 Final metallization

The final metallization is done with the same 2 layer resist process as was used for the first metallization. The pattern this time also includes 160  $\mu\text{m}$  openings in the p-contact, so a gold layer can be evaporated above it for better probing than would be possible onto chrome or platinum. The metal layer put down is Ti/Au, 20 nm/1000 nm and is lifted off in acetone. Following this, the sample is lapped, the Ni/Au backside metal for mounting is evaporated, and the sample is cleaved for testing. A finished device is shown in top view and in cross section in Figure 15. The top metal is hanging over the top of the ridge somewhat in Figure 15 (b); the cleaving is not as ideal as in an as-grown wafer, and the epi film and the thick top metal does not break as evenly in the microstrip laser as it does in the conventional

laser. Still, good cleaves are obtained as is evidenced by the threshold and efficiency performance to be presented in Chapter 5, Results.



(a)



(b)

Figure 15. (a) Top view of a fabricated microstrip laser. (b) SEM cross section of a fabricated microstrip laser.

## References

- [1] K. Streubel, J. Wallin, G. Landgren, U. Ohlander, S. Lourdudoss, and O. Kjebon, "Importance of metalorganic vapor phase epitaxy growth conditions for the fabrication of GaInAsP strained quantum well lasers," *Journal of Crystal Growth*, vol. 143, pp. 7-14, 1994.
- [2] I. H. Tan, C. Reaves, A. L. Holmes, Jr., E. L. Hu, J. E. Bowers, and S. DenBaars, "Low-temperature Pd bonding of III-V semiconductors," *Electronics Letters*, vol. 31, pp. 588-9, 1995.
- [3] Y. Okuno, K. Uomi, M. Aoki, and T. Tsuchiya, "Direct wafer bonding technique aiming for free-material and free-orientation integration of semiconductor materials," *IEICE Transactions on Electronics*, vol. E80-C, pp. 682-8, 1997.
- [4] I. H. Tan, Hewlett Packard Corporation., San Jose, CA , personal communications, 1995.
- [5] G. L. E. Turner, "CRC Handbook Of Chemistry and Physics - A Ready-Reference Book Of Chemical and Physical Data, 70th Edition - Weast,R.C , Lide,D. R. ," *Annals Of Science*, vol. 48, pp. 496-497, 1991.
- [6] Y. H. Lo, R. Bhat, D. M. Hwang, M. A. Koza, and T. P. Lee, "Bonding by atomic rearrangement of InP/InGaAsP 1.5  $\mu$ m wavelength lasers on GaAs substrates," *Applied Physics Letters*, vol. 58, pp. 1961-3, 1991.
- [7] A. Black, A. R. Hawkins, N. M. Margalit, D. I. Babic, A. L. Holmes, Jr., Y. L. Chang, P. Abraham, J. E. Bowers, and E. L. Hu, "Wafer fusion: materials issues and device results," *IEEE Journal of Selected Topics in Quantum Electronics*, vol. 3, pp. 943-51, 1997.
- [8] Y. Feurprier, C. Cardinaud, and G. Turban, "Influence of the gas mixture on the reactive ion etching of InP in CH<sub>4</sub>-H<sub>2</sub> plasmas," *Journal of Vacuum Science & Technology B (Microelectronics and Nanometer Structures)*, vol. 15, pp. 1733-40, 1997.
- [9] M. Kappelt and D. Bimberg, "Wet chemical etching of high quality V-grooves with {111} A sidewalls on (001) InP," *Journal of the Electrochemical Society*, vol. 143, pp. 3271-3, 1996.
- [10] P. A. Morton, R. A. Logan, T. T.-. Ek, J. P. F. Sciortino, A. M. Sergent, R. K. Montgomery, and B. T. Lee, "25 GHz bandwidth 1.55  $\mu$ m GaInAsP p-doped strained multiquantum well lasers," *Electron. Lett*, vol. 28, pp. 2156-2157, 1992.

- [11] R. Olshansky, W. Powazinik, P. Hill, V. Lanzisera, and R. B. Lauer, "InGaAsP buried heterostructure laser with 22 GHz bandwidth and high modulation efficiency," *Electron. Lett.*, vol. 23, pp. 839-841, 1987.
- [12] H. Wada, H. Horikawa, Y. Matsui, Y. Ogawa, and Y. Kawai, "High-power and high-speed 1.3  $\mu\text{m}$  V-grooved inner-stripe lasers with new semi-insulating current confinement structures on p-InP substrates," *Applied Physics Letters*, vol. 55, pp. 723-5, 1989.
- [13] D. Z. Tsang and Z. L. Liao, "Sinusoidal and digital high-speed modulation of p-substrate mass-transported diode lasers," *IEEE J. Lightwave Technol.*, vol. 5, pp. 300-304, 1987.

## **Chapter 5**

### **Device Results**

The laser results presented in this chapter are best classified according to device type and measurement type. The different devices fabricated and characterized for this work include the following: (1) conventional broad area lasers; (2) microstrip broad area lasers; (3) conventional ridge lasers, 10  $\mu\text{m}$  wide ridge, no surrounding dielectric; (4) microstrip ridge lasers, 10  $\mu\text{m}$  wide ridge, no surrounding dielectric; (5) conventional narrow ridge waveguide lasers, surrounded with polyimide; (6) microstrip narrow ridge waveguide lasers, surrounded by polyimide. The different measurements are: (1) DC threshold, efficiency, output power, and spectral characteristics; (2) DC thermal resistance; (3) microwave propagation properties, including attenuation per unit length and phase velocity.

#### **5.1 Broad area laser results**

In Figure 1, the threshold properties of conventional and microstrip broad area lasers are compared. The threshold current density versus length for both structures are plotted in the figure. The data are for pulsed operation of the lasers (pulse width  $\sim 500$  ns, repetition frequency = 5 kHz) at 20  $^{\circ}\text{C}$ . These characteristics are critical and are the first indicator of the material and the facet quality. The broad area laser measurements are necessary because, for the most part, the wide 50  $\mu\text{m}$  ridge eliminates the excess optical loss often present in a narrow ridge structure, and thus gives a reliable characterization of the base material [1].

Photoluminescence (PL) measurements can also be done to characterize the base material; since broad area lasers are easily fabricated and provide more quantitative laser information than PL does, this kind of characterization is essential.

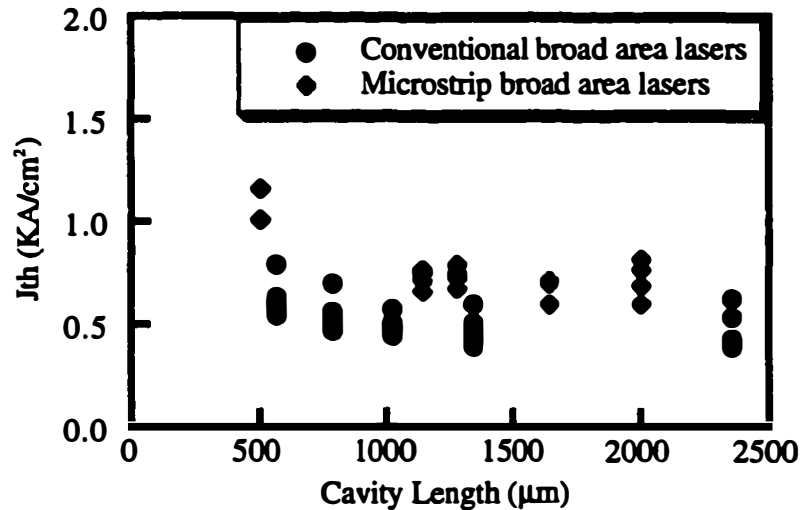


Figure 1. Threshold current density of conventional broad area lasers and microstrip broad area lasers. The microstrip laser thresholds are about 50% higher than the conventional thresholds.

The microstrip broad area laser fabrication was done to determine the degree of material degradation, if any, caused by the gold bonding process. During bonding the epi is stressed by differential thermal expansion forces. It is well known that a crystal relieves large amounts of stress or strain by generating line defects. Since the line defects are non-radiative recombination centers, significant numbers of them in the microstrip wafer will translate into increased laser thresholds. As Figure 1 shows, the thresholds of the microstrip broad area lasers are about 50% higher than those of the best conventional broad area lasers; some of the microstrip laser thresholds are roughly equal to some of the conventional laser

thresholds. These results indicate that while the bonding process may introduce some degradation, it is not excessive to a point that renders the microstrip laser an unfeasible design. The higher thresholds may be partially due to nonuniformities across the wafer, and not a result of material degradation at all; results to be presented later in this chapter show that 10  $\mu\text{m}$  ridge microstrip lasers exhibited only a 20-30% increase in the threshold current density. Since the threshold degradation appears to be greater at shorter cavity lengths, the problem may be caused by cleaving, where the threshold is more sensitive to facet reflectivity. Since the cleaving process in the microstrip laser really involves the breaking of the thin epi film over the gold. The breaking is caused by the stress initiated from the cleaving of the substrate below, but the epi crystal planes are not attached to those of the substrate.

Measuring the output spectrum of the laser is another way to determine if the epi film has been significantly stressed [2, 3]. Strained layer quantum wells, as discussed in the introduction, are commonly grown for lasers because they exhibit superior performance relative to lattice matched quantum wells [4]. The crystal deformation brought about by the strained layers changes the electronic properties of the material, namely, the bandgap and the operating wavelength shifts [5]. Similarly, a crystal strained by the bonding process (but not to the point of lattice relaxation) should show a wavelength shift.

Drawing a believable conclusion by comparing spectra of bonded and conventional wafers requires that the two pieces come from a highly uniform source wafer. This is not the case for the broad area lasers presented here, which show a spectral variation as large as 100 nm in the peak emission wavelength.

Results from more uniform material will be presented later, in the narrow ridge laser section, and the spectral comparison is presented there.

The dependence of the laser differential efficiency on length is as important as the threshold current density versus length characteristics. This dependence is important because from it the optical loss and the internal efficiency of the laser (fraction of injected carriers that recombine in the active region) can be determined. Differential efficiency is determined from the slope of the L-I curve, which represents the total power emitted by the laser per current injected (watts/amperes). With the appropriate conversion factor, the differential efficiency, representing photons emitted per electrons injected, is determined. The relation between the slope efficiency and the differential efficiency is simply expressed as  $W/A$  (watts/amp) =  $N_p h \nu / N_e e$  where  $N_p$  is the number of photons,  $N_e$  is the number of electrons,  $h$  is Planck's constant,  $\nu$  is the frequency of the light emitted and  $e$  is the electron charge. The differential efficiency is  $N_p/N_e$ . For the 1.55  $\mu\text{m}$  wavelength of these lasers, multiplying the slope of the above threshold L-I curve by 1.25 provides the correct conversion. It should be noted that the L-I curve slope must first be multiplied by a factor of two because light is emitted from both facets. If the reflectivity of each facet is identical, and the internal optical loss and the gain is uniform along the length, equal power will be emitted from each facet, thus the factor of two multiplication. Alternatively, the light from both facets can be measured.

Before using the efficiency data to calculate the loss and the internal efficiency, a phenomenological comparison of conventional and microstrip lasers is useful, to get an idea of how the performance differs. In this treatment, one directly compares L-I curves for the two sets of devices and notes the distribution of the

thresholds and efficiencies. Some of the better L-I curves for conventional and microstrip devices for 2 device lengths are shown in Figures 2 (a) - (b).

The measurements of Figures 1 and 2 were taken from the same set of devices, but at different dates; the original threshold performance of the microstrip lasers was actually better at the earlier date, but the efficiency data from those measurements were not presently available. Some degradation occurred in the microstrip lasers over that time and the best threshold data for the second set of measurements is shown in Figure 3. In these plots, the threshold current densities of the microstrip laser are about twice as high as the conventional lasers, in contrast to the data of Figure 1, where only a 50% increase was observed between the best devices at comparable lengths. The higher thresholds suggest a lifetime problem in the microstrip lasers. The differential efficiencies,  $\eta_d$ , of the microstrip lasers are also lower, which is consistent with the increase in threshold. Differential efficiency data versus length for both devices are shown in Figure 4. The best microstrip efficiencies are about half the best conventional efficiencies, similar to the threshold results.

The efficiency measurement is important, because the reciprocal of the total differential efficiency (both facets) plotted versus length provides information about the internal device efficiency,  $\eta_i$ , representing the fraction of injected carriers that

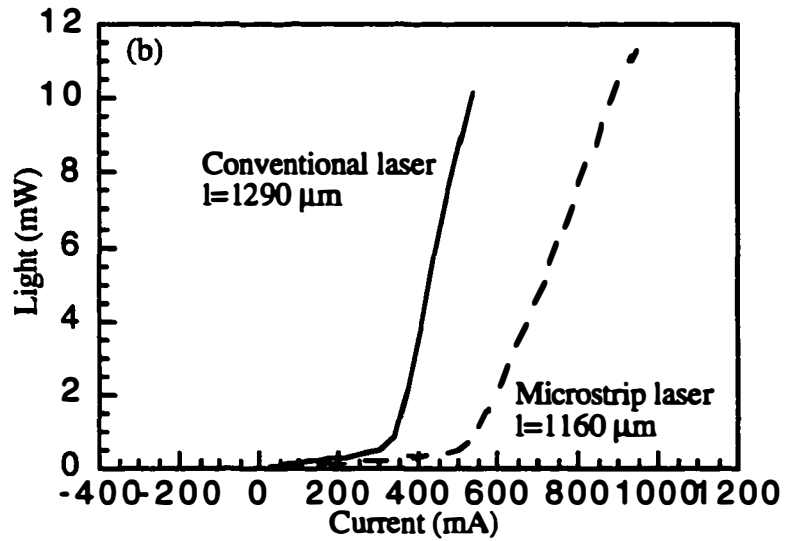
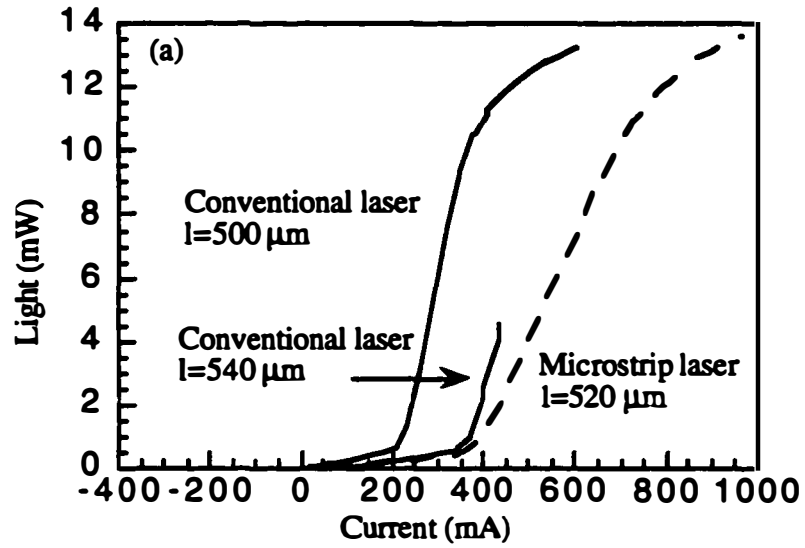


Figure 2. Comparison of L-I curves for conventional broad area lasers and microstrip broad area lasers.

recombine in the active region, and the internal optical loss  $\langle\alpha_i\rangle$  [5]. Analysis following Coldren and Corzine [5] shows that the inverse efficiency plot versus length is characterized by the following equation:

$$\frac{1}{\eta_d} = \frac{\langle\alpha_i\rangle}{\eta_i \ln(1/R)} L + \frac{1}{\eta_i}$$

where  $R$  is equal to  $r_1 r_2$ , the product of the field reflectivity of each facet, equal to about 0.32 for the InP lasers we are working with. The equation indicates that the y-intercept of the inverse differential efficiency plots versus length gives the inverse

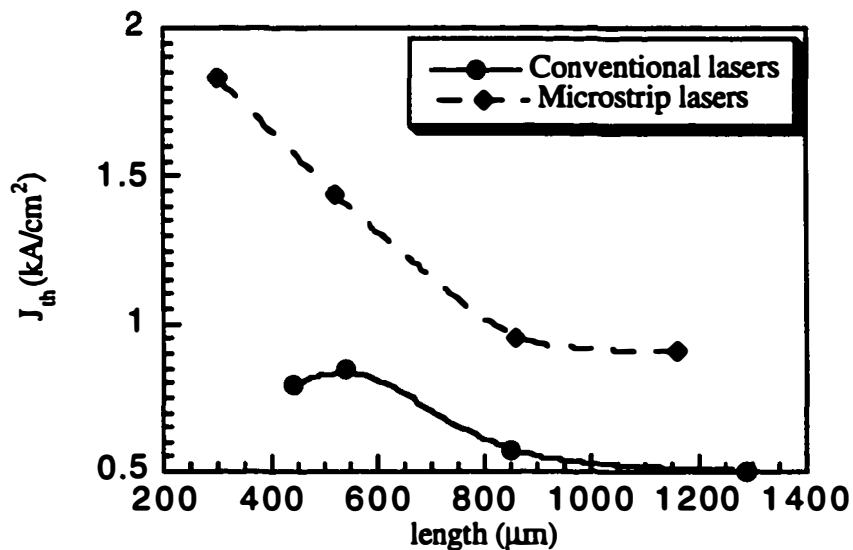


Figure 3. Threshold performance of microstrip broad area lasers and conventional broad area lasers. This data were taken after multiple measurements of the lasers and there was some degradation in the threshold performance of the microstrip lasers in particular.

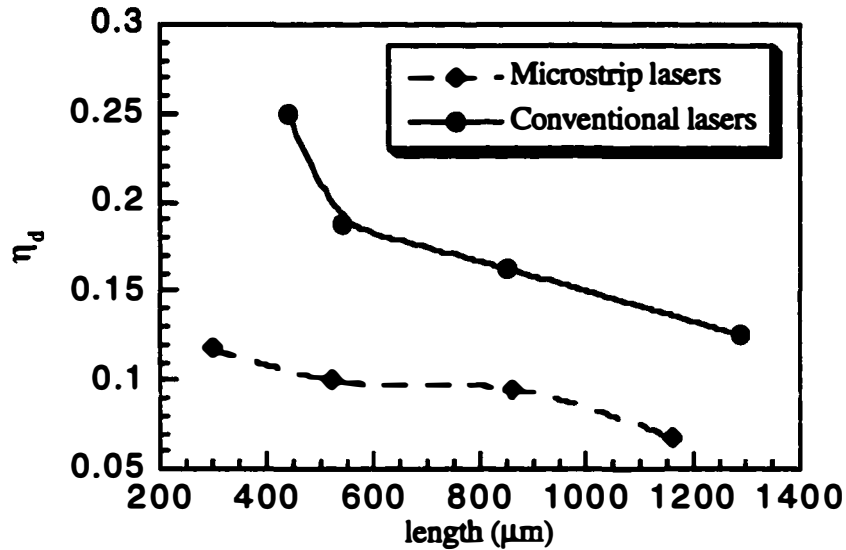


Figure 4. Differential efficiencies versus length for microstrip and conventional broad area lasers.

internal efficiency of the laser. Once this is known, along with the facet reflectivities, the slope of the curve gives the internal loss. Plots of this for the best broad area microstrip lasers and the best conventional broad area lasers are shown in Figure 5, and Table 1 lists the internal efficiencies and optical losses generated from the data. Table 1 shows the optical loss of the conventional lasers is about 40% higher than the microstrip laser loss, and that the internal efficiency of the conventional lasers are more than twice as high. Although the slope of the conventional laser data is lower than that of the microstrip lasers, the loss calculated from the data is still higher because the slope is proportional to  $\langle \alpha_i \rangle / \eta_i$ , and the conventional laser efficiency is higher. The numbers in Table 1 are calculated assuming equal reflectivity facets, since no facet coating was applied.

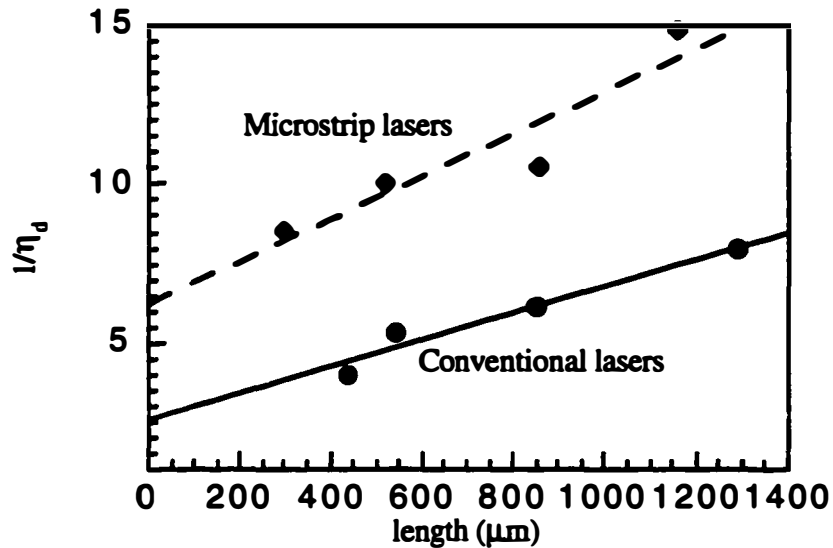


Figure 5. Inverse differential efficiency versus device length for microstrip broad area lasers and conventional broad area lasers.

Laser	Internal efficiency, $\eta_i$	Optical loss, $\langle\alpha_i\rangle$
Conventional broad area	0.40	17 cm <sup>-1</sup>
Microstrip broad area	0.16	12 cm <sup>-1</sup>

Table 1. Internal efficiency and optical loss for conventional and microstrip broad area lasers.

Understanding the differences in internal efficiency and optical loss requires understanding how those numbers are calculated from the efficiency versus length data. Uncertainty in this intercept value, due to scatter in the data, can cause a significant uncertainty in the value of the intercept value. Note also, that when the differential efficiencies are much smaller than 1, the reciprocals are much larger than 1, and even a small amount of scatter can be converted into a large uncertainty in the

internal efficiency. Further, according to the equation above, any uncertainty in the internal efficiency converts into uncertainty in the value of the internal loss. Since the inverse efficiencies in the plots are significantly greater than 1, and there is scatter in the data, the values quoted for  $\eta_i$  and  $\alpha_i$  need to be considered in that light.

While the exact numbers quoted above need to be considered in light of this discussion, they do suggest that the internal efficiencies of the particular microstrip lasers measured at the later time are significantly lower than the conventional lasers. The lower internal efficiency suggests that the microstrip laser is more susceptible to the opening up of leakage paths in the device with repeated operation. This also explains the phenomena observed in the threshold data taken at different times, that show a more rapid degradation mechanism in the microstrip lasers than in conventional lasers. This subject will be returned to later on in this chapter when discussing the performance of narrow ridge microstrip lasers.

## 5.2 10 $\mu\text{m}$ ridge lasers

The next level of complexity in the laser fabrication was to reduce the ridge width to 10  $\mu\text{m}$  from the broad area width of 50  $\mu\text{m}$ . The purpose of this was to determine whether decent lasers of a more practical size could be made, and could be operated cw. As in the broad area case, both conventional and microstrip lasers were fabricated for purposes of comparison. The 10  $\mu\text{m}$  ridges are wide enough that they could be probed directly, like the broad area lasers, and therefore no polyimide planarization and bondpad metal patterning is necessary.

The first set of devices successfully tested were from p-doped material. The threshold current density vs. length for conventional broad area lasers, 10  $\mu\text{m}$  wide conventional p-ridge lasers and 10  $\mu\text{m}$  microstrip ridge lasers are shown in Figure 6. The p-doping of the material contributes to a high base threshold current density, greater than 2  $\text{kA}/\text{cm}^2$  as can be seen in the plot. The thresholds of the microstrip n-ridge lasers are about the same as the broad area lasers and the 10  $\mu\text{m}$  p-ridge laser - indicating that the narrower ridge process does not introduce excess loss or additional leakage paths, and the quality of the bonded laser material is equivalent to the as-grown material. Because the base material was so poor in these devices, the threshold currents were very high, even for the 10  $\mu\text{m}$  ridge lasers - greater than 100 mA, and for all practical purposes, these devices are of little use.

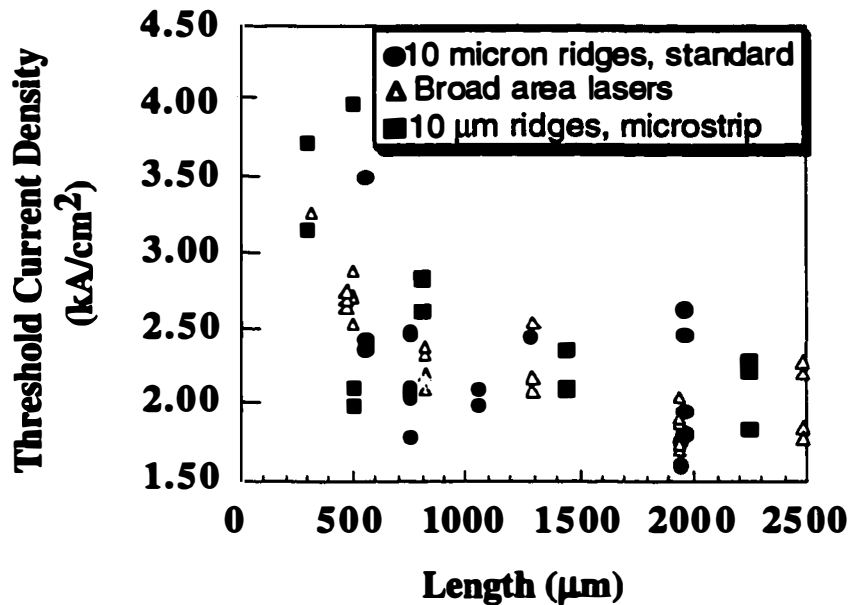


Figure 6. Comparison of threshold for 50  $\mu\text{m}$  conventional broad area lasers, 10  $\mu\text{m}$  conventional lasers, and 10  $\mu\text{m}$  microstrip lasers, showing largely equivalent threshold performance.

A second set of 10  $\mu\text{m}$  ridge lasers was subsequently fabricated from undoped material of better quality than that of the first run. The threshold current density versus length characteristics are shown in Figure 7, and we can see, that as in the previous plot, the device performance is not that different from the broad area lasers. The thresholds of the bonded devices are about 20-30% higher than the broad area lasers in this case. This is probably caused by a combination of minor lateral current spreading, as discussed in Chapter 3, and by slightly higher optical loss in the narrower ridge. In any case, if there is degradation due to the bonding process it is not that severe.

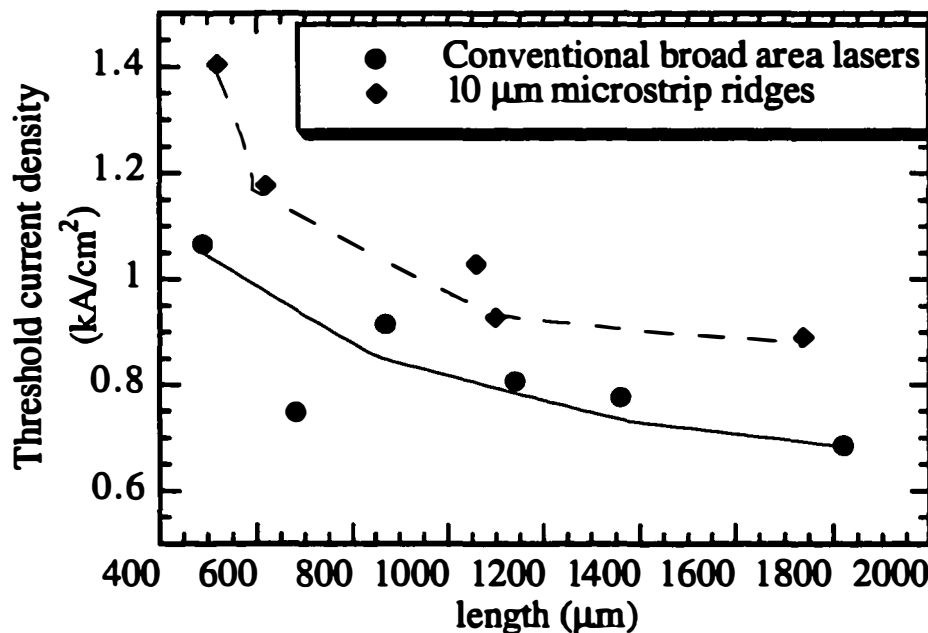


Figure 7. Threshold comparison of 10  $\mu\text{m}$  ridge microstrip lasers and conventional broad area lasers. The microstrip laser thresholds are about 20-30% higher than the broad area lasers.

The efficiencies of these devices were somewhat scattered, despite good consistency on the thresholds. The absolute value of the thresholds were also relatively high, because of the 10  $\mu\text{m}$  ridge width. The best value was about 75 mA. This, along with the fact that the ridges tended to be damaged by the direct probing led us to pursue the narrow, polyimide buried ridge structures rather than these devices.

### 5.3 Narrow ridge devices

The narrow ridge devices are of widths 1, 1.5, 2, 2.5, 3, 5, and 10  $\mu\text{m}$ . The 10  $\mu\text{m}$  ridges are test devices for the wafer and for the process run, and are not of practical use beyond the purpose of the devices described in the previous section.

Before delving into the details of the laser results, a spectral comparison of bonded devices and conventional devices, from the material used for the devices, is presented. Spectra can be compared by measuring the photoluminescence from a bare piece of the as grown wafer and from a piece of the bonded material. Alternately, the below threshold spontaneous emission spectra from two laser structures, grown from a uniform wafer, provides similar information. The above threshold lasing emission can also be used; care must be taken however to ensure that the conventional and the microstrip lasers function at similar gain levels. If they do not, the measurement is not valid because the peak of the gain spectrum shifts as the peak gain changes.

The spectral comparison was done between two sets of ridge lasers that were fabricated from uniform material, grown on a 2 inch wafer in a rotating chamber (instead of a quarter wafer, non-rotating chamber, as was the case for the

broad area laser measurements above). Figure 8 shows the lasing spectra of both conventional and microstrip 10  $\mu\text{m}$  ridge lasers. The lasing wavelength is 1540 nm in both cases. Figure 9 shows the below threshold spontaneous emission, for both cases, also peaks between 1535 and 1540 nm. This data suggests that the bonding process is not causing any significant wavelength shift in the material. The one noticeable difference that suggests that there may be an effect is that the spectral width of the spontaneous emission spectra appears to be smaller, by more than a factor of two, in the microstrip lasers than in the conventional devices. This may be caused by reflection of spontaneous emission from the fused gold layer back into the mode region, narrowing the spectrum. It is less likely that it is caused by a strain effect, since the gold is malleable and should absorb any strain induced during the bonding process. Further, drawing a definitive conclusion from this data is difficult: the spontaneous emission spectrum narrows as the pumping level increases, and a one to one comparison of pumping levels for two lasers below threshold is difficult. Other measurements on microstrip lasers showed spontaneous emission bandwidths up to about 30 nm.

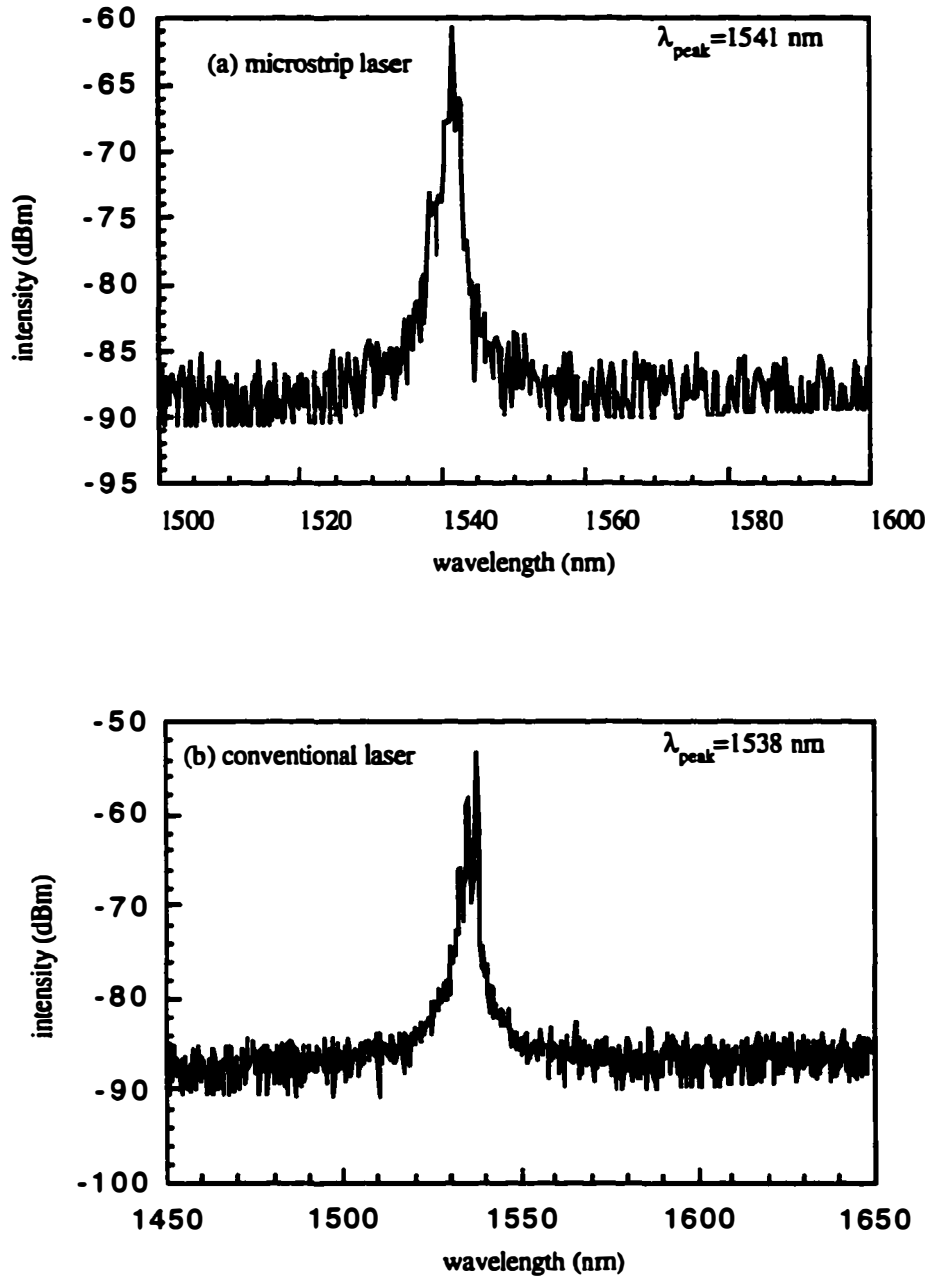


Figure 8. (a) Lasing spectrum of a  $10 \mu\text{m}$  wide,  $390 \mu\text{m}$  long microstrip laser. (b) Lasing spectrum of a  $10 \mu\text{m}$  wide,  $500 \mu\text{m}$  long conventional laser. Both devices are from the same base material, and lase at a similar wavelength.

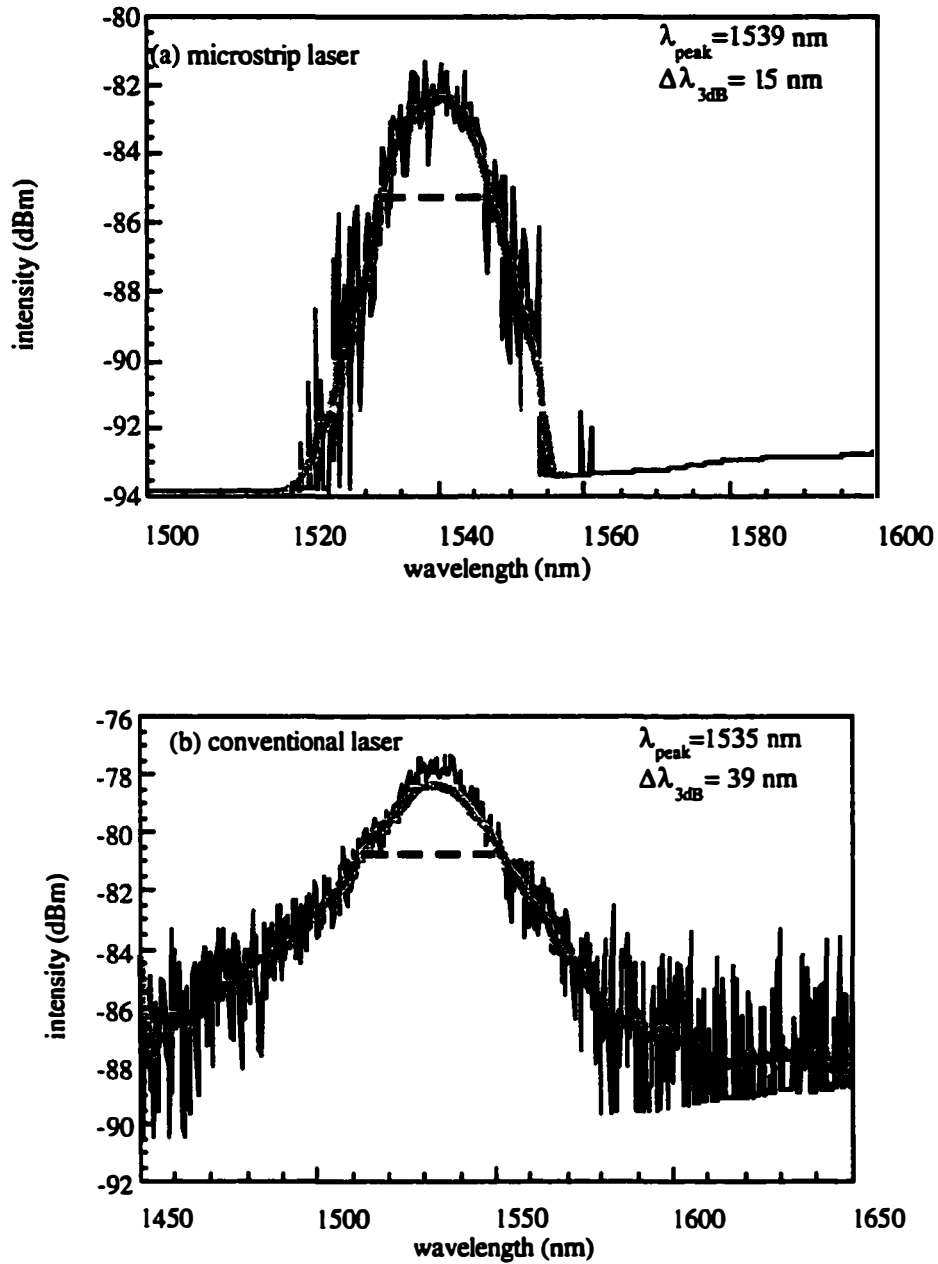


Figure 9. (a) Spontaneous emission spectrum of 10  $\mu\text{m}$  wide, 390  $\mu\text{m}$  long microstrip laser. (b) Spontaneous emission spectrum of 10  $\mu\text{m}$  wide, 500  $\mu\text{m}$  long conventional laser. Both devices are from the same base material.

The above threshold gain, however, for the two devices, is known to be about the same, because the devices are not that different in length and the optical loss is comparable, as will be demonstrated in a later section.

The actual device widths deviate from the widths specified by the stripes. The amount and nature of the deviation depends on the particular process run and is a consequence of wet etching, which can produce sloping sidewalls and/or undercut. As an example, Figure 10 (a) shows a narrow ridge microstrip device etched to the SCH layer in HCl. Since the stripe masked used for etching this particular device was metal, the InP slopes, and the ridge width at the bottom is about 6  $\mu\text{m}$ , whereas at the top it is about 2  $\mu\text{m}$ . Figure 10 (b) shows a process run in which the ridge was wet etched, but for which a SiN stripe mask was used instead of metal. The stripes were oriented along the [001] direction so the InP etched vertically in HCl, but the subsequent SBW active region etch undercut the ridge nonuniformly. The undercut below the mask is apparent in the SEM, with the dark region above the ridge being the SiN stripe. The rounded edge at the base of the ridge is characteristic of the SBW etch. Figure 10 (c) shows a device in which the InP ridges slope outward, but for which the InGaAsP quaternary in the active region is undercut. In this particular run, the stripe was oriented in the wrong direction, causing the sloping ridge; nonetheless reasonable threshold currents were still obtained since the undercut of the active region compensates somewhat for the widened ridge.

The first set of narrow ridge devices tested resemble those of Figure 10 (a), with the ohmic metal used for stripe definition, and the InP ridge etched in HCl. The ridge extended down to the SCH layer - neither the SCH nor the active region

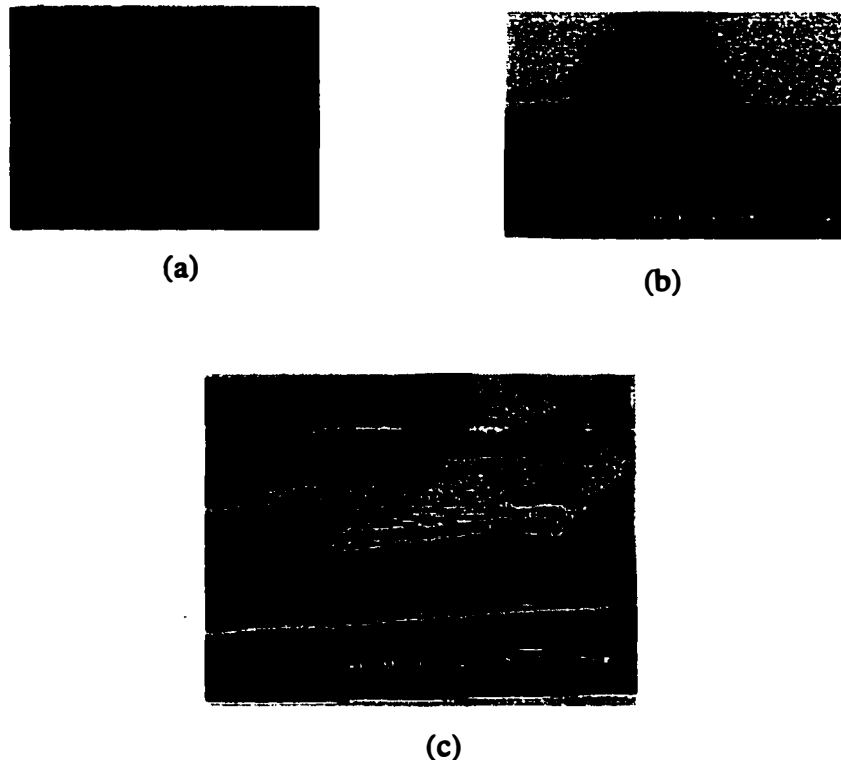


Figure 10. (a) Ridge in which metal mask was used to wet etch the ridge. The narrow  $2\ \mu\text{m}$  ridge at the top widens at the base to about  $6\ \mu\text{m}$ . (b) Wet etched ridge in which a dielectric mask was used and for which the active region was etched away. Note the undercut at the top of the ridge caused by the active region etch. (c) Wet etched ridge oriented incorrectly, causing sloping sidewalls. The active region is also undercut, restoring the desired width.

were etched. Some cw L-I curves of one of these devices,  $620\ \mu\text{m}$  long,  $2\ \mu\text{m}$  wide at the top, and  $6\ \mu\text{m}$  wide at the base are shown in Figure 11 for temperatures ranging from  $10^\circ\ \text{C}$  to  $50^\circ\ \text{C}$ . Two properties of these curves stand out as important. The first is that the thresholds are quite high - at room temperature, the threshold current is about  $90\ \text{mA}$ , impractically high for useful operation. The second is that despite the high thresholds, the lasers still run cw - at  $50^\circ\ \text{C}$  with a threshold current close to  $300\ \text{mA}$ . Conventional lasers with thresholds this high

will not lase cw because the active region heating reduces the material gain so much that the threshold condition (gain = loss) cannot be met. Continuous wave laser operation at such high thresholds strongly suggests that the active region heating is minimal, despite the high current passing through it. In other words, the thermal resistance is much lower in this microstrip laser than it is in conventional lasers of the same dimensions. Both the gold layer and the n-doped ridge contribute to this improvement in thermal performance. We also note that the low power output observed in the plot was primarily caused by the measurement setup at the time, which made it very difficult to get good coupling between laser facet and detector. The coupling loss is estimated to be about a factor of 10.

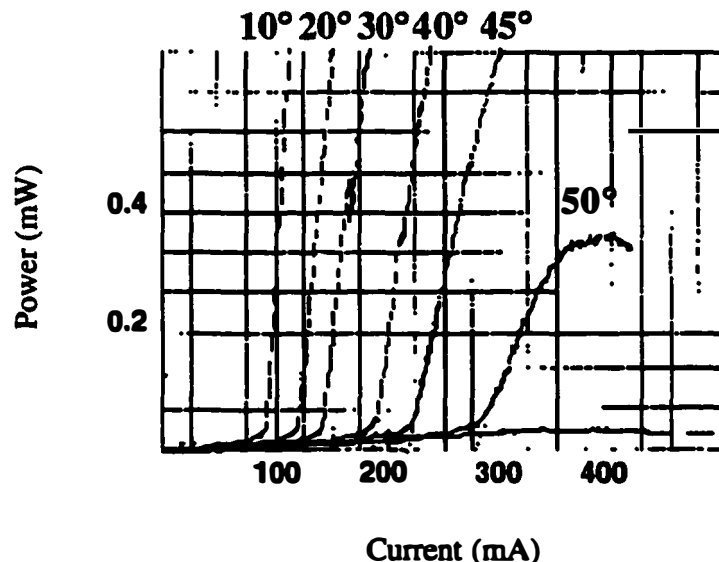


Figure 11. CW operation of the microstrip laser,  $6 \mu\text{m}$  wide at the base, as in Figure 10 (a). The etch in this device was stopped at the upper SCH, thus causing the very high thresholds.

The extremely high thresholds of the device unfortunately preclude high power operation, which in turn precludes high speed operation. The high thresholds, as discussed in Chapter 3, are caused by the lateral spreading of the

electron current injected from the n-ridge into the SCH and active region [6, 7]. Figure 12 plots the pulsed threshold current density versus length for these microstrip lasers and for conventional broad area lasers fabricated from the same material. The threshold current densities of the microstrip lasers are up to 6 times higher than the broad area lasers. The differential efficiencies of the pulsed devices are also poor, about 0.04 for the 620  $\mu\text{m}$  long laser of Figure 11. Shorter lasers around 350  $\mu\text{m}$  in length had somewhat better efficiencies of about 0.08, but nothing higher than this was measured. The narrow ridge efficiencies suffer from the current spreading problem, and the leakage path through the upper SCH robs the active region of the total current injected from the contact. Because of the effect of the current spreading on both the threshold and the efficiency, these devices are not practical and do not demonstrate high speed or high power performance.

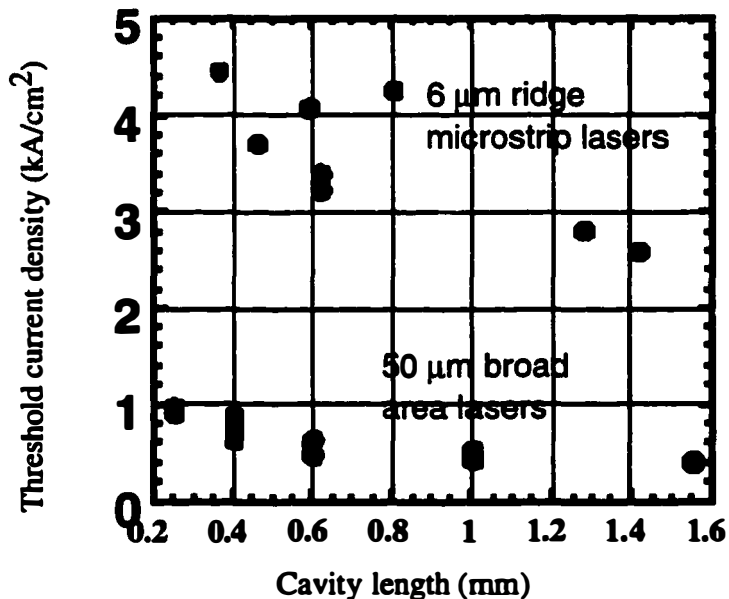


Figure 12. Threshold current density versus length for narrow ridge microstrip lasers etched to the upper SCH, compared to broad area lasers fabricated from the same wafer. The thresholds of the microstrip lasers are about 6 times higher than the broad area lasers.

In general, confining the electron current should reduce the thresholds while still maintaining the superior thermal properties. This can be done in a variety of ways, the simplest being an etch through the SCH and the active region, as has been discussed in previous chapters. In all other respects, the device is structurally the same as those presented above.

Devices with etched SCH and active regions showed significantly improved thresholds and differential efficiencies. The yield of the samples was low however, and a significant number of lasers on the wafer exhibited the high thresholds seen in the earlier generation of devices. The reason for this is not clear, except to assume that the active region etch was accompanied by defect formation or excess optical loss in some cases, or additional leakage paths. Since the wet etch is inherently non-uniform, as discussed in Chapter 4, it is not unreasonable that the device performance across the wafer might vary greatly. The fact that some of the devices showed good performance indicates that in principle and to a certain degree in practice, the active region wet etch works well for solving the current spreading problem.

Figure 13 compares the threshold current densities of the ridge lasers relative to the optimal broad area threshold current densities. The data are shown for 5  $\mu\text{m}$  wide ridge lasers.

To further illustrate the superiority in threshold of the etched devices, Figure 14 shows the ratio of the microstrip laser thresholds to the broad area lasers for both cases: etch stopped at the upper SCH, and fully etched through the active region. The threshold current densities are only twice as high as the broad area

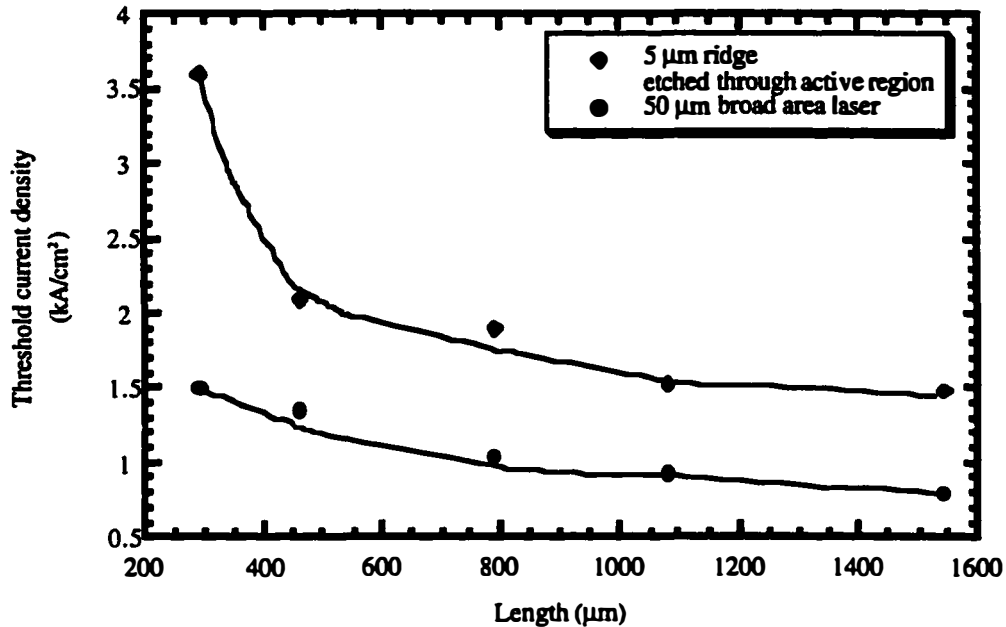


Figure 13. Threshold current densities of n-ridge microstrip lasers with the active region etched away.

lasers for the etched active region case, in contrast to the six-fold increase in the unetched devices. More important, the actual thresholds of the devices, are low enough for practical device operation. Figure 14 shows the relative threshold current densities for narrower ridge lasers 2.5 and 3 μm wide, also indicative of reasonable performance. The absolute thresholds of some of the devices without the active region etch are listed in Table 2, and in Table 3, the thresholds of 2.5 μm ridge devices with the active region etched are listed. The unetched devices have unrealistically high thresholds in the vicinity of 100 mA or much higher, whereas the lowest threshold current for the unetched device is about 32 mA. This is a very reasonable number for practical device operation.

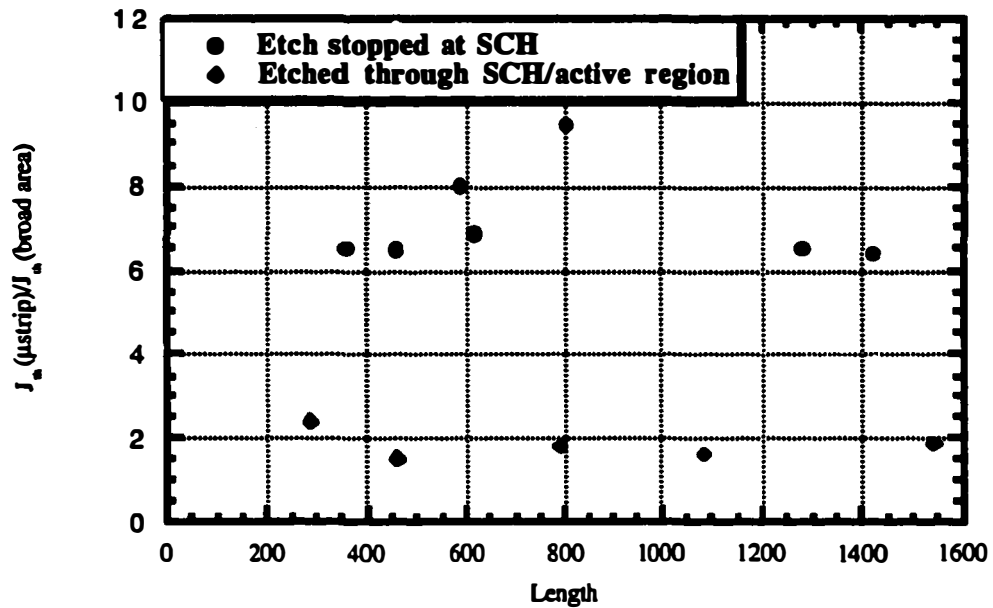


Figure 14. Threshold current density of the the microstrip lasers, normalized to their respective broad area laser thresholds. The lasers with the etched active region demonstrate much improved performance.

The efficiencies of the etched ridge devices are reasonable. As with the thresholds, the efficiencies exhibited significant variation across the wafer. However, the best devices show reasonable performance in this respect, that are consistent with the broad area laser characterization. Figure 16 plots the total differential efficiencies versus length for the broad area lasers. There is so much scatter in the data that it is difficult to determine specific numbers for optical loss and internal efficiency. The differential efficiencies of the conventional lasers for

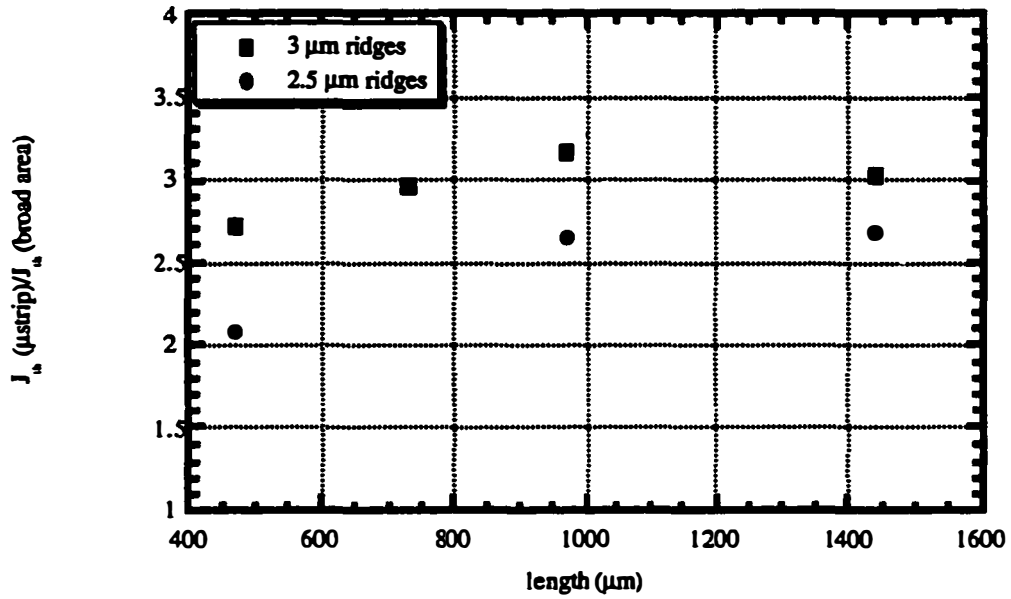


Figure 15. Threshold current densities normalized to broad area results for 2.5 μm and 3 μm wide ridges.

Length (μm)	Threshold current (mA)
460	85
620	100
800	170
1420	185

Table 2. Threshold currents for 6 μm wide ridge lasers with the etch stopped at the upper SCH.

Length (μm)	Threshold current (mA)
470	32
730	59
970	62
1440	83

Table 3. Threshold currents for 2.5 μm ridge lasers with etched through active regions.

shorter devices ( $<500 \mu\text{m}$ ) are about 50%. To compare, for the microstrip lasers, the best efficiencies for similar length devices are about 25%. Given that the thresholds are also higher in the microstrip lasers by about a factor of two, the two-fold reduction in differential efficiency is not unexpected. Figure 17 shows the inverse total differential efficiency versus length for  $2 \mu\text{m}$  microstrip ridge lasers. The fit to the data indicates that internal efficiency is 0.27 and the optical loss is  $10 \text{ cm}^{-1}$ ; one of the points appears to lie off the general trend of the data - excluding that point from the fit gives  $\eta_i = 0.35$  and  $\langle\alpha_i\rangle = 16 \text{ cm}^{-1}$ . The differential efficiencies for the  $5 \mu\text{m}$  ridge resulted in an estimated internal efficiency of about 0.46, and an optical loss is  $21 \text{ cm}^{-1}$ .

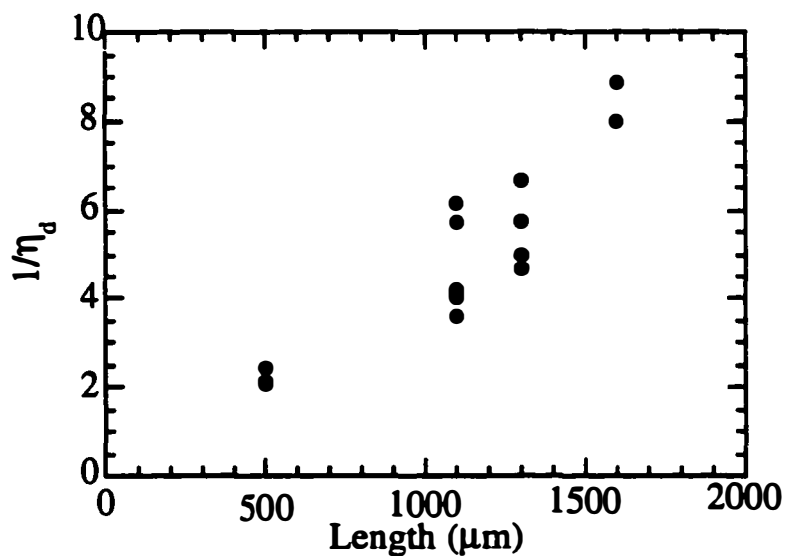


Figure 16. Inverse differential efficiencies versus length for broad area lasers.

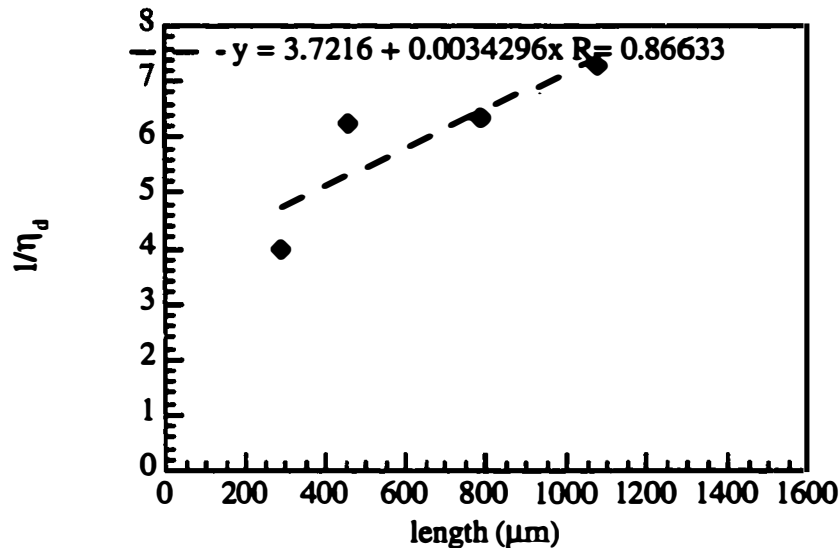


Figure 17. Inverse differential efficiencies versus length for 2  $\mu\text{m}$  wide ridge lasers, etched through the active region.

These lasers should be good candidates for high power performance, since both the thresholds and the efficiencies are reasonable. However, this set of devices had severe problems with the electrical resistances, which were much higher than had been expected. For example, the I-V curves of 2.5  $\mu\text{m}$  ridge lasers are plotted in Figures 18. The resistances are very high, ranging from 13-17 ohms, depending on device length. Some other devices, such as the 5  $\mu\text{m}$  ridge lasers of Figures 13-14 exhibited resistances as high as 35 ohms. The cause of this appears to be related to the bottom side p-contact, rather than the n-contact, as devices of different width do not exhibit the expected trends in the resistance, as can be seen in Figure 19. While the contacts were annealed in the process at 380  $^{\circ}\text{C}$ , this may not

have been high enough to reduce the p-contact resistance despite the wide bottom contact. It is unlikely that the large resistances measured were caused by the etched active region: while the etched active region may contribute some additional resistance, as was discussed in Chapter 3, the values measured here appear to be too high, and further, a trend with ridge width would be seen as well if the problem was related to the etched active region.

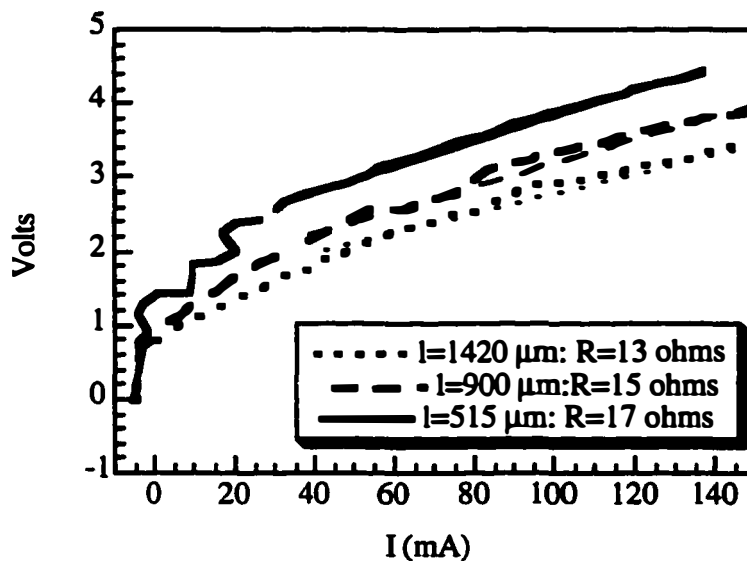


Figure 18. I-V curves for  $2.5 \mu\text{m}$  ridge lasers of various length. The resistances are higher than expected.

On the other hand, IV curves of the microstrip lasers in which the SCH and active region were not etched away are shown in Figure 20 and display excellent resistance for a  $620 \mu\text{m}$  long device. The resistance of the probe station is about 4 ohms, so the device resistance is very low, on the order of 1 ohm or less.

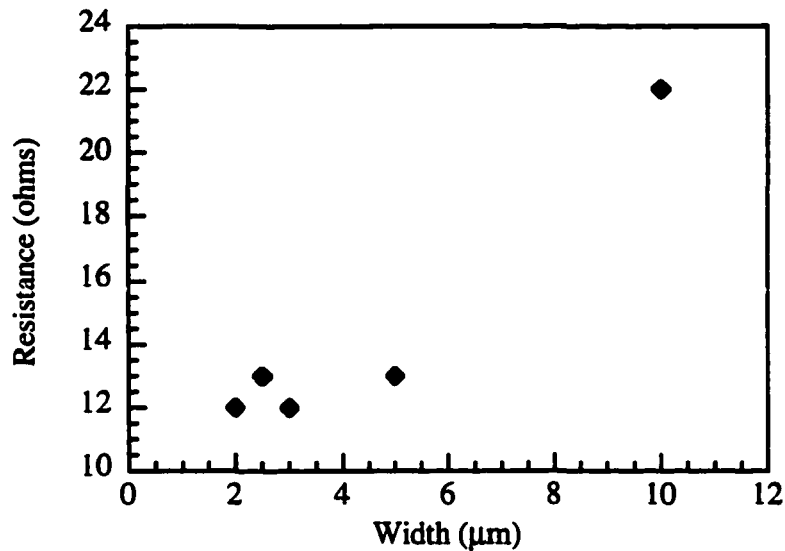


Figure 19. Resistance of the etched active region microstrip lasers for different widths, for lasers 1420  $\mu\text{m}$  long.

To reduce the resistance of the low threshold devices, further contact annealing was done. Contact annealing at 400 °C, 410 °C, and 420 °C was done. The I-V curves of a 960  $\mu\text{m}$  long, 5  $\mu\text{m}$  wide ridge is shown in Figure 21; it is clear that the annealing reduces the turn on voltage down to the desired 0.7 volts and also reduces the resistance to reasonable levels. None of the annealed devices exhibit resistances as low as that of the unetched devices, yet the resistances of about 4 ohms (subtracting out the probe resistance of 4 ohms) shown are fair. It is possible that the slightly higher resistance in the etched devices is in fact due to the active region etch.

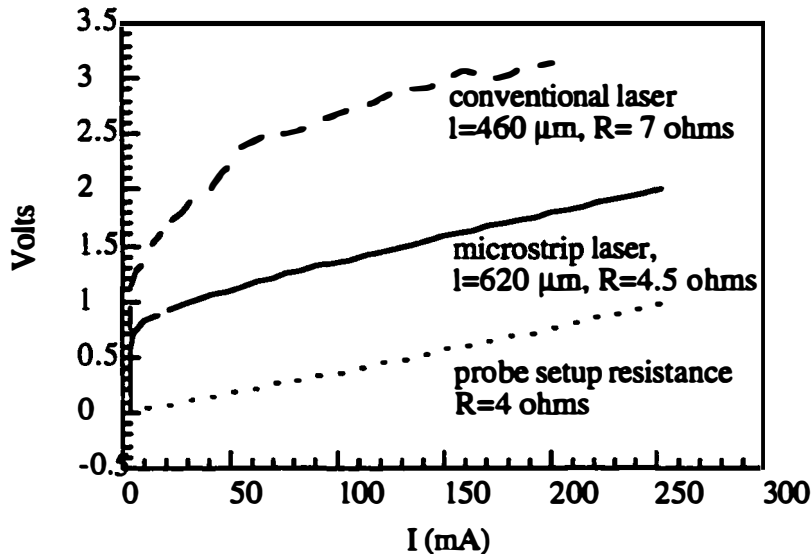


Figure 20. Resistances of a conventional p-ridge laser, an n-ridge microstrip laser, and the measurement setup, showing extraordinarily low resistance of the microstrip laser.

In Figure 22, the L-I curves of the devices after each anneal step is shown. Apparently, the annealing process, while reducing the device resistance also damages the active region enough to raise the threshold, and at the higher temperatures even makes the laser not even work at all. The problem may be due to the fact that the active region was exposed during this high temperature anneal, with the temperature treatment opening up leakage paths. It is possible that some carbon was left on the ridge surface during the  $\text{CF}_4$  removal of the  $\text{SiN}_x$  during the process, although an oxygen plasma was done following the  $\text{CF}_4$  etch. If there was carbon residue, it could have diffused in during the anneal and damaged the active region. Since the contact problem here appears to be at least partially caused by the

p-contact, the best way to solve this would be to perform the anneal immediately after wafer bonding, and prior to device processing.

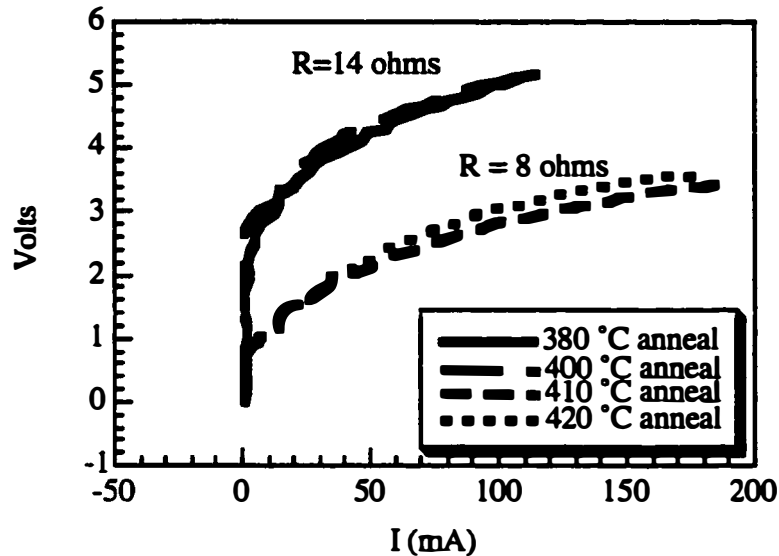


Figure 21. IV curves for an etched active region device, 960  $\mu\text{m}$  long, 5  $\mu\text{m}$  wide, after several annealing steps.

As discussed in Chapter 4, above 400  $^{\circ}\text{C}$  the possibility of gold spiking from the bonded layer increases. The annealing tests presented in Figures 21 above indicate that the samples used here are able to tolerate slightly higher temperatures - at 420  $^{\circ}\text{C}$ , spiking could be seen in SEM pictures of some of the devices spike but not all. Since, as discussed in Chapter 4, the spiking process is an activation energy process characterized by an exponential increase in diffusion length with temperature, slight temperature variations across the sample are probably responsible for the fact that not all devices showed spiking. The 410  $^{\circ}\text{C}$  anneal seems to sufficiently reduce the resistance of most of the devices on the wafer without causing spiking.

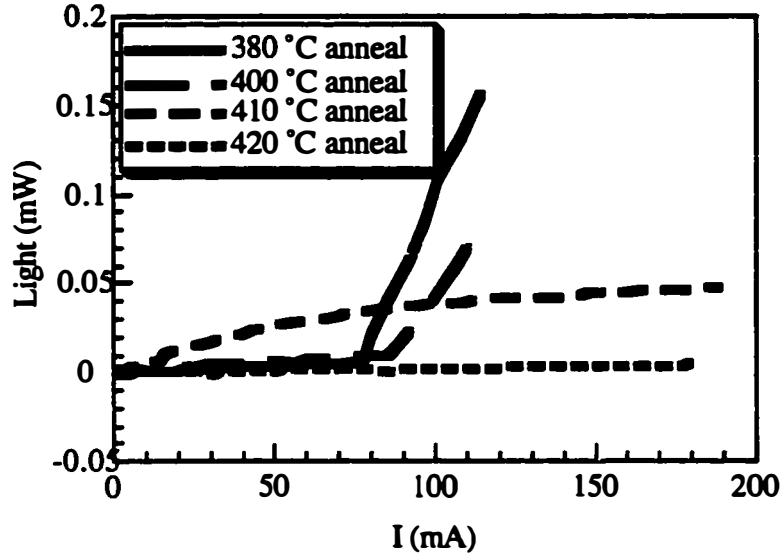


Figure 22. L-I curves of etched active region microstrip lasers, for various annealing conditions. The laser threshold degrades significantly as the anneal temperature increases, when the active region is exposed during the anneal.

These particular lasers had trouble operating cw also. Above a certain cw current, the diodes would short out. As discussed in the section on microstrip broad area lasers, the microstrip lasers appear to be more susceptible to the opening of parasitic leakage paths, and it is possible that in these low threshold devices, the problem was severe enough to render cw operation impractical.

It is not clear why the unetched devices did not show this kind of problem with contact resistance, or such a catastrophic reaction for cw operation. The annealing of the unetched device was performed at 380 °C and the resistance was excellent. The exposed active region of the later set of devices surely is not advantageous for lifetime, but is necessary for decent thresholds. The resistance

problem may have been caused by poor doping levels in the contact layers also; i.e. the material may not have been as good in terms of electrical properties.

#### **5.4 Thermal resistance**

Despite the high thresholds in devices with an unetched SCH/active region, these lasers still operate cw, indicative of superior thermal performance. Referring to Figure 11, at 50 °C cw operation was achieved with a threshold near 300 mA. A conventional device will not lase at such a high threshold. The rise in the active region temperature of the microstrip laser and a conventional p-ridge laser of similar dimensions were measured, and the results for several different mount temperatures are shown in Figure 23. The thermal resistance is defined as the active region temperature rise divided by the power dissipated, so the plot provides thermal resistance data. A couple of things are clear from Figure 23. First of all, the microstrip laser shows an active region temperature rise equivalent to that of the conventional laser, but at much higher levels of dissipated powers [8]. This translates into a much reduced thermal resistance. The second thing noticed is that the microstrip laser data does not linearly intersect the origin, suggesting a thermal nonlinearity at the high dissipated power levels where those measurements were taken. Tables 4 (a) summarizes the room temperature power dissipated at threshold for the two devices under the different operating conditions, and the thermal resistance for each case.

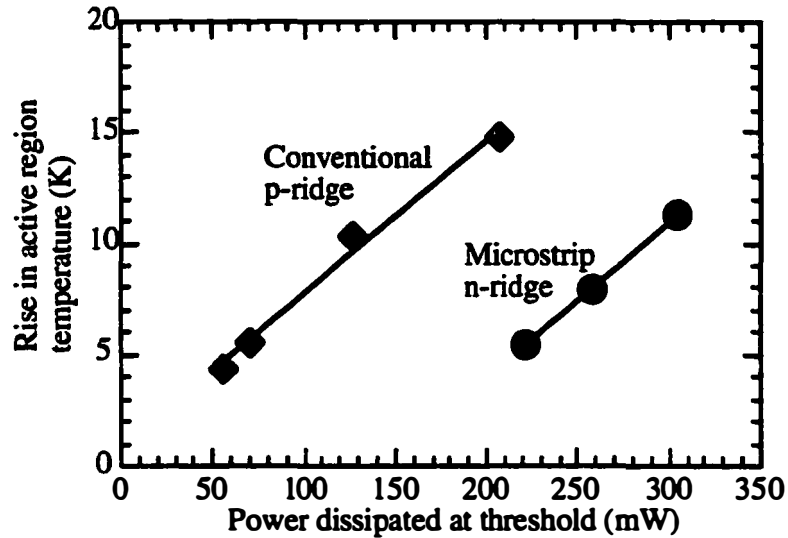


Figure 23. Rise in active region temperature versus power dissipated at threshold for an n - ridge microstrip laser and a conventional laser.

	Power dissipated at threshold (mW)	Rise in active region temperature (K)	Thermal resistance (K/W)
Microstrip laser	221	5.4	24.4
Conventional laser	56	4.4	78.6

Table 4. Relevant thermal resistance data for the microstrip laser and the conventional laser at a temperature of 20 °C. The thermal resistance of the microstrip laser is smaller by about a factor of 3.

The thermal resistance of the microstrip laser is much smaller, suggesting extremely high power operation if the laser threshold were to be reduced while still maintaining the low electrical resistance of these microstrip lasers. The data in Figure 23 and table 4 were obtained by measuring both the pulsed thresholds of the lasers at different mount temperatures, and then measuring the cw thresholds at

different mount temperatures as well, to obtain several data points for the plot. Negligible heating was assumed in the pulsed case (300 ns pulses, 0.1% duty cycle). The active region temperature in the cw case was determined by mapping a cw threshold to a temperature on the pulsed threshold - temperature curve. The heat power generated at threshold is determined from the voltage-current product at threshold, with the spontaneous emission power subtracted out.

As described earlier, the reduction in thermal resistance results from the heat spreading properties of the gold layer and, even more significantly, from the fact that most of the heat power in this microstrip laser is generated in the lower (p) cladding where it does not significantly heat the active region. The n-ridge microstrip laser therefore provides a similar function as does p-side down mounting in a conventional laser, but the function is incorporated into the fabrication process rather than in a complicated post-processing technique.

Given the thermal resistance of the microstrip laser is superior to that of the conventional laser, it is worthwhile to investigate the kind of output power improvement one might expect to achieve from a laser operating at a reasonable threshold, rather than the elevated threshold of the devices used for the measurement. Here we investigate the improvements expected from the etched active region microstrip lasers with good thresholds, assuming they did not suffer from the leakage current problem, and could be operated cw.

The thermal nonlinearity in the plot is fitted for purposes of this calculation. Figure 24 shows an exponential fit to the microstrip laser data; at low values of dissipated power the exponential fit approximates a straight line, as expected, but at higher values correctly fits the measured data. The exponential fit is used to model

a nonlinear thermal runaway effect. The conventional laser data is also fitted with an exponential, which for the range of measured data well approximates a straight line.

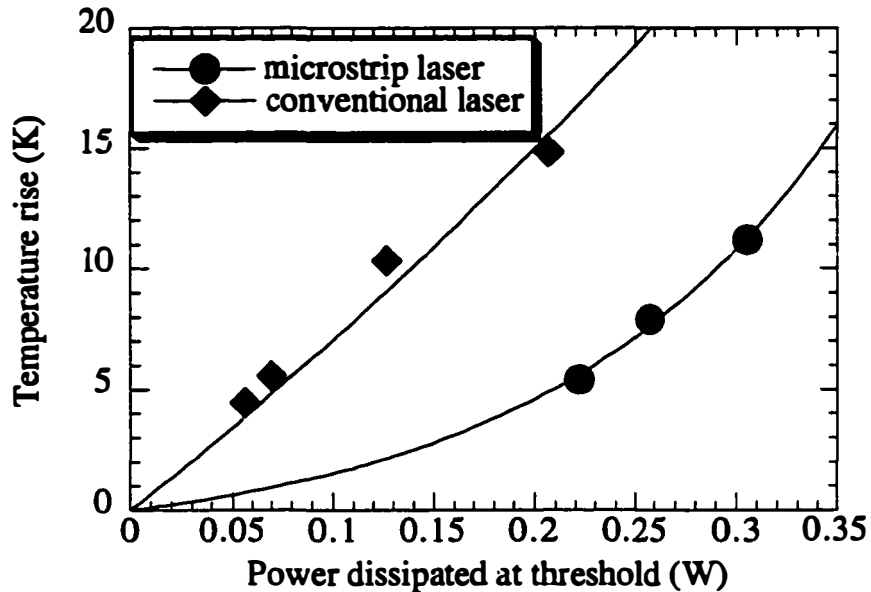


Figure 24. Thermal resistance data, fitted for purposes of calculation.

The expected L-I curves can be calculated using the thermal resistance fits in Figure 24, and the temperature dependent threshold, which follows the usual exponential relation  $I_{th} = I_0 e^{T/T_0}$ , with  $T_0 = 50$  K, as determined from pulsed L-I curves, taken at different mount temperatures. The calculation uses the thresholds and efficiencies measured from the etched active region microstrip laser devices. The L-I curves are compared in Figure 25 and shows the microstrip laser output power to be 70% greater than the conventional laser power.

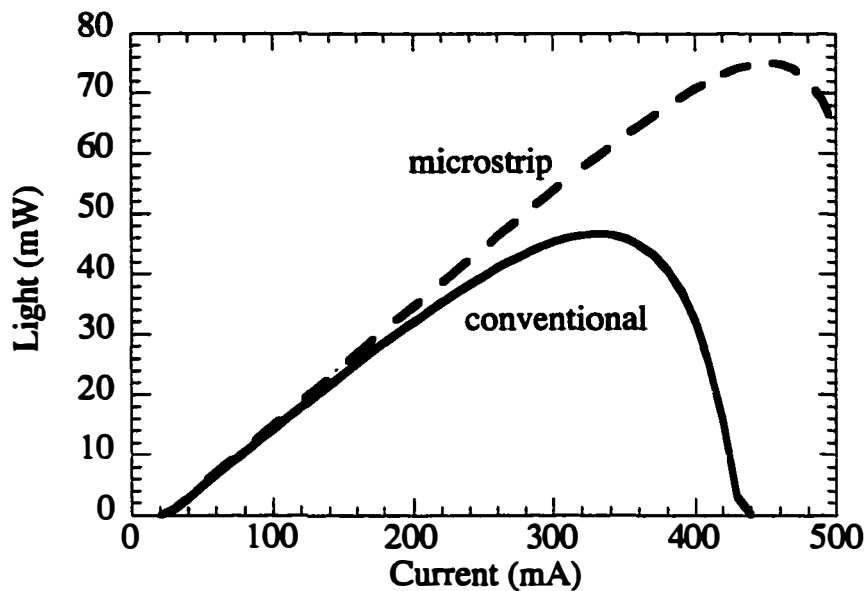


Figure 5.25. Calculated L-I curves using the thermal resistance data collected for the microstrip laser and the conventional laser.

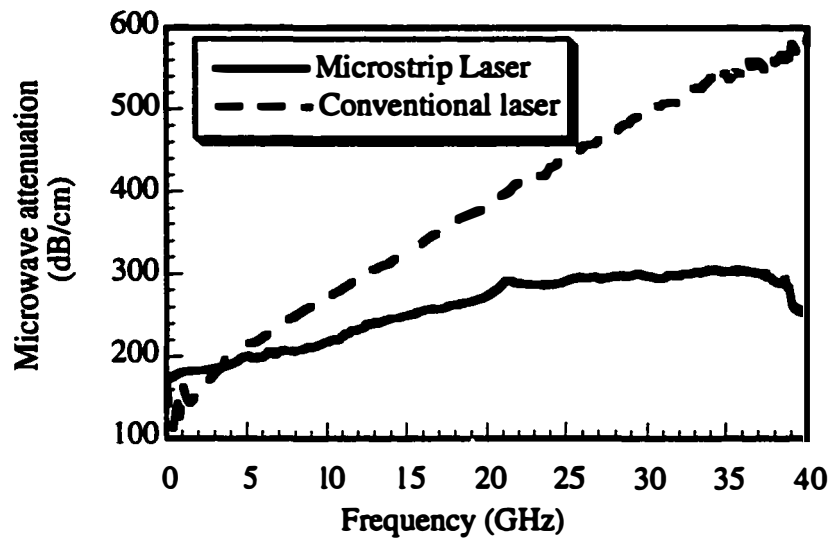
### 5.5 Microwave performance

The microwave propagation properties of the microstrip laser were also measured, and compared to the conventional p-ridge laser on a doped substrate. The microwave propagation parameters for both lasers were determined from a calibrated, .045 - 40 GHz two port s-parameter extraction on an HP8510 network analyzer. The microwave signal was launched and received with two coplanar microwave probes (ground-signal-ground) that were separated by  $600 \mu\text{m}$  along the laser stripes. One of the probes was also used as the DC bias connection. For the conventional laser, the coplanar probing geometry was accomplished by grounding the two unbiased laser stripes which surrounded the biased stripe to the backside contact. This probing method was used since an accurate calibration could not be

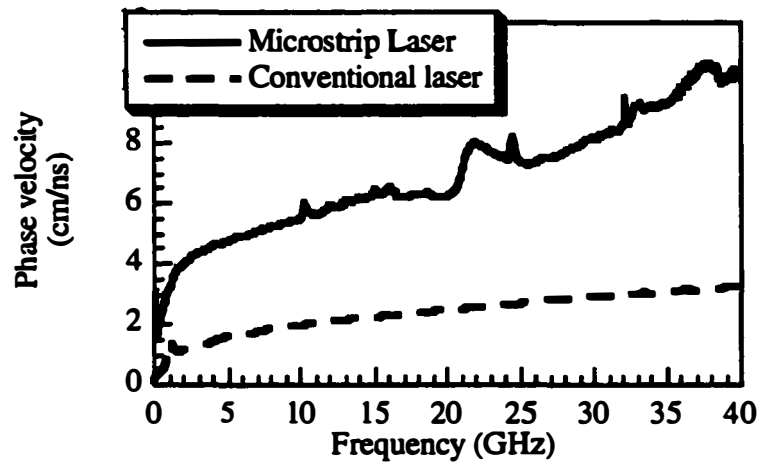
performed using the standard coaxial to microstrip transition which terminates with a ribbon bond on the laser bondpad.

The microstrip laser exhibits much improved performance in terms of both phase velocity and attenuation, compared to the conventional laser, because the loss is much lower, and the confinement of the magnetic field relative to the electric field is tighter. Figure 25 compares the measured loss and phase velocity of each device, demonstrating that the microstrip laser is superior in both respects, as expected. Also shown in the plots are the calculated results, derived from the model presented in Chapter 2. There is good agreement between theory and experiment. At the high frequency end of the microstrip laser measurements, there is some deviation between the model and the experiments which is likely due to loss of microwave calibration. As expected from the calculations, the experiments still show the microstrip laser to be a much better transmission line than the conventional doped substrate laser. As discussed and calculated in Chapter 2, the microstrip laser also shows better performance than the coplanar electrode laser.

A few points about the graphs can be made. First of all, the attenuation in the microstrip laser is smaller by more than a factor of two at high frequency. This extends the bandwidth limit due to distributed effects to much higher frequencies, beyond 50 GHz. One should also note that the frequency dependence of the attenuation is much less pronounced in the microstrip laser than in the conventional laser. This is because the primary source of loss in the microstrip laser is the forward biased conduction loss, which has a much weaker frequency dependence, that the skin loss that dominates the conventional laser, due to the microwave



(a)



(b)

Figure 25. (a) Comparison of forward biased microwave attenuation for conventional laser and microstrip laser. (b) Comparison of forward biased phase velocity.

propagation in the doped substrate. For the microstrip laser, there appears to be a resonance in the data around 20 GHz, or so, most likely arising from a reflection in the device. The data in that frequency range needs to be understood with that knowledge. Up at the higher frequencies, near 40 GHz, the noise in the phase velocity plots suggests that the calibration was beginning to fail as well. Nonetheless, the overall result is definitive: the microwave propagation properties of the microstrip laser are much better than that of the conventional laser, and should contribute to better high frequency performance.

The particular lasers for which the propagation was measured did not exhibit excellent bandwidth, because they were the devices with unetched active regions and showed high thresholds, low efficiencies, and low power output - thus implying the photon density was also low. Since high photon density is a requirement for high bandwidth, the bandwidth in these devices was limited to about 6 or 7 GHz. The microstrip lasers with etched active regions suffered from high resistance and shorting out during cw operation, and they too, therefore, were not practical for large bandwidth performance. The data strongly suggest however, that the principle is correct and that an etched microstrip laser with good resistance and stable cw performance would exhibit high bandwidth if the basic active region material was high speed.

Theoretical rolloff and bandwidth plots can be generated to show the improvement in going from the conventional laser to the microstrip laser. This is shown in Figures 26-27; the calculation is similar to that presented in Chapter 2, except the experimental data rather than the calculated propagation properties are used for the bandwidth determination. Since the experimental data and the theory

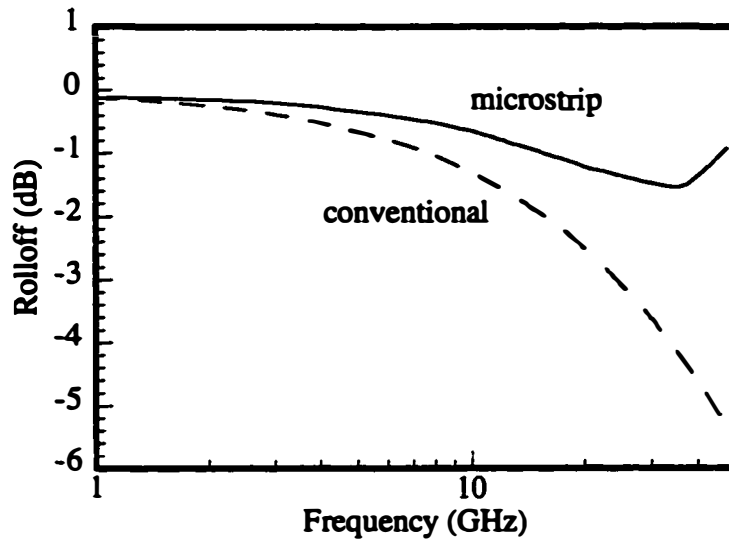


Figure 26 Experimentally determined rolloffs in the square of the injection current to the active region for a conventional laser and a laser on a doped substrate.

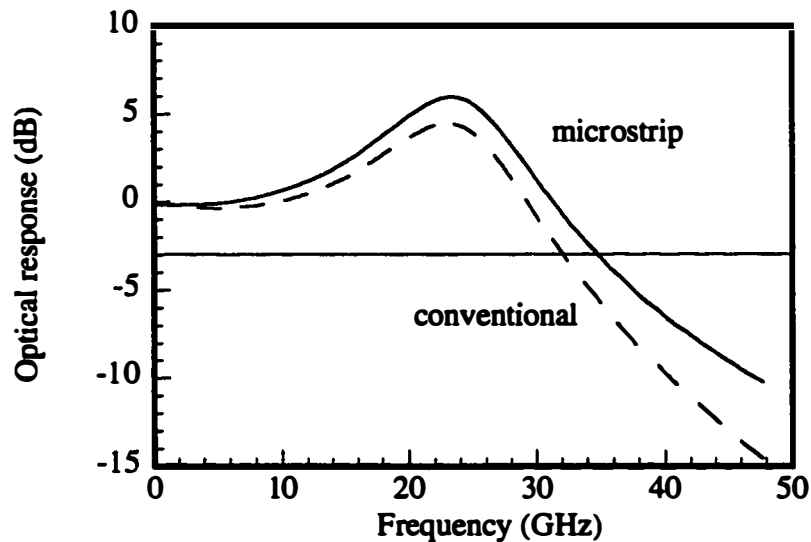


Figure 27 Modulation responses extracted from the rolloff plots of Figure 26 for the microstrip laser and the conventional laser on the doped substrate.

matches quite well, the difference between these calculations and those in Chapter 2 is not very large. It is clear from the figure that the rolloff of the microstrip laser happens at much higher frequencies than it does for the conventional doped

substrate laser, and that the effective bandwidth is pushed out to higher frequencies, for this particular case, a device with an intrinsic bandwidth of 37 GHz has a 36 GHz bandwidth in the microstrip design and 31 GHz in the conventional design.

## 5.6 Summary and conclusions

In this chapter, we demonstrated that the DC properties of microstrip lasers were comparable that of conventional in plane lasers with regard to threshold and efficiency. The bonding process does not cause excess material degradation, as was verified by threshold and spectral measurements. A small increase in threshold was observed for broad area microstrip lasers; this increase could have been due to a slight degradation in facet quality, because facets are formed by breaking the thin laser film above the bonded gold layer, and a true cleaving process is not really used. For narrow ridge devices, lateral current spreading from an n-ridge into a wide SCH region was shown to cause high thresholds and poor efficiencies, and this problem was solved by etching through the SCH and active region. When this was done, very good performance was measured.

The thermal resistance of the n-ridge microstrip laser was shown to be more than 3 times smaller than the conventional p-ridge laser. From this, output power performance more than 70% greater was predicted by using the temperature dependent threshold data. Excellent electrical resistances for narrow ridge lasers were also obtained, on the order of 1 ohm or less.

Some problems were encountered with regard to leakage currents and degradation. After repeated use, the thresholds of microstrip broad area lasers

increased more than did the thresholds of conventional lasers. When subject to moderate temperatures of about 400 °C, microstrip lasers with exposed active region suffered from increases in thresholds. The opening up of leakage paths, or the possibility of in-diffusion of carbon left on the sample during CF<sub>4</sub> etches may have caused this. The good threshold and efficiency performance of the narrow ridge etched active region devices was countered by high resistances in those devices. The resistance was lowered by annealing, but the threshold degradation discussed above prevented the realization of a good low resistance, low threshold microstrip laser. CW operation was also problematic, and the devices would short out when operated cw. This could be due to the leakage current problem discussed above. These problems, more likely than not, are not insoluble, as the devices that were not etched through the SCH/active region showed very low resistance and worked cw over extended periods of operation (though degradation was observed in them as well). It may be that material/doping problems led to the high resistances in the devices with low thresholds, and annealing the devices at about 400 - 410 °C immediately after gold bonding, rather than at a later point in the process after the active region was exposed would avoid the threshold degradation seen in those devices.

The microwave propagation properties were also superior, with phase velocities 2-3 times greater than the conventional laser and microwave attenuation about a factor of 2 smaller. Incorporating the microwave propagation models presented in Chapter 2 to predict bandwidth, it was shown that the rolloff frequency of the microstrip laser was beyond 50 GHz. A high frequency laser with a 37 GHz intrinsic bandwidth [9] is predicted to be limited to 31 GHz if fabricated in the

conventional doped substrate mode and 36 GHz in the microstrip design. The data clearly indicate that significant advantages to the microstrip laser compared to a conventional laser for both high power and high frequency.

## References

- [1] B. W. Hakki, "Carrier and gain spatial profiles in GaAs stripe geometry lasers," *Journal of Applied Physics*, vol. 44, pp. 5021-5028, 1973.
- [2] D. Gershoni and H. Temkin, "Optical properties of III-V strained-layer quantum wells," *Journal of Luminescence*, vol. 44, pp. 381-98, 1989.
- [3] K. F. Huang, K. Tai, S. N. G. Chu, and A. Y. Cho, "Optical studies of In/sub  $x$ /Ga/sub  $1-x$ /As/GaAs strained-layer quantum wells," *Applied Physics Letters*, vol. 54, pp. 2026-8, 1989.
- [4] P. J. A. Thijs, L. F. Tiemeijer, J. J. M. Binsma, and T. v. Dongen, "Progress in long wavelength strained-layer InGaAs(P) quantum-well semiconductor lasers and amplifiers," *IEEE Journal of Quantum Electronics*, vol. 30, pp. 477-499, 1994.
- [5] L. A. Coldren and S. W. Corzine, *Diode Lasers and Photonic Integrated Circuits*. New York: John Wiley and Sons, 1995.
- [6] J. H.S. Sommers and D. O. North, "Experimental and theoretical study of the spatial variation of junction voltage and current distribution in narrow stripe injection lasers," *Journal of Applied Physics*, vol. 48, pp. 4460-4467, 1977.
- [7] W. T. Tsang, "The effects of lateral current spreading, carrier out-diffusion, and optical mode losses on the threshold current density of GaAs-Al $_x$ Ga $_{1-x}$ As stripe geometry DH lasers," *Journal of Applied Physics*, vol. 49, pp. 1031-1043, 1978.
- [8] D. Tauber, M. Horita, J. Piprek, P. Abraham, J. A. L. Holmes, and J. E. Bowers, "The microstrip laser," *IEEE Photonics Technology Letters*, vol. 10, to be published April, 1998.
- [9] J. D. Ralston, S. Weisser, I. Esquivias, E. C. Larkins, J. Rosenzweig, P. J. Tasker, and J. Fleissner, "Control of differential gain, nonlinear gain and damping factor for high-speed application of GaAs-based MQW lasers," *IEEE J. Quantum Electron*, vol. 29, pp. 1648-1658, 1993.



## **Chapter 6**

### **Summary and future prospects**

This dissertation has investigated a novel semiconductor laser, the microstrip laser. A gold bonding process was developed by which a laser film is transferred from the original substrate on which it was grown to an independent substrate. The gold bonding creates a microstrip wafer in which the laser film sits above a 1  $\mu\text{m}$  thick gold ground plane above an independent substrate. The microstrip laser addresses several important issues in high frequency and high power laser design, and further, offers some device possibilities not normally attainable by conventional growth and fabrication procedures.

The high frequency issues addressed by the microstrip laser are primarily related to microwave propagation effects in high speed lasers. The microstrip laser electrode structure resembles the microstrip line of high frequency circuits, in that a dielectric material (the laser epi film) is sandwiched between a top metal strip contact and a continuous gold ground plane on the bottom. This kind of design forces microwave currents to flow in the high conductivity gold contact layers primarily, as opposed to doped semiconductor regions, thus minimizing the microwave loss and ensuring greater high frequency signal uniformity across the electrodes. Phase velocities are also higher in the microstrip laser because the skin losses are lower, and skin loss always contributes to wave slowing. Experiments and calculations both show that the microwave phase velocities are higher by at least a factor of two and that the attenuation is lower by a factor of two. Calculations show that bandwidth limits for lasers on doped substrates are set at about 30 GHz for devices

around 300  $\mu\text{m}$  long, whereas the microstrip laser limits due to the distributed microwave effects are greater than 50 GHz.

It should be emphasized that at a fundamental level, the reevaluation of the semiconductor laser as a distributed element rather than a lumped element, is a key conceptual shift. It is not uncommon for high frequency laser to have phase shifts of more than 90 ° from the feed point to the far end of the device, and this has important implications for device design and applications. The development of the microstrip laser is only one example of this. Another device investigated and discussed in this thesis is the coplanar electrode laser, which shows improved transmission line performance relative to the doped substrate laser also. The point is that when high frequency lasers are understood to be distributed electrical elements, the high frequency design rules applied in microwave circuits become applicable to lasers as well. Thus, the best high speed diode lasers need to be fabricated in a coplanar stripline or microstrip geometry, as microwave circuits are, and on doped substrates where the substrate acts as a lossy ground plane.

This dissertation studied how distributed effects modified the small signal response of a high speed laser. The effects go beyond the small signal domain and clearly influence the large signal response also. In fact, the effects may even be more severe in the large signal domain, since the impedance properties of the laser diode change depending on bias level, particularly on the low bias scale. Several large signal effects that have been reported include mode locking in a single contact geometry, due to the localization of the high frequency current [1] and harmonic generation limitations in gain switched devices due to the nonuniform frequency attenuation of signals composing the electrically injected pulse used for gain

switching [2]. Because the laser diode is inherently a nonlinear transmission line in the large signal domain, a host of other nonlinear pulse propagation effects may exist and are worthy of further investigation [3]. One example might be the study of electrical soliton formation in high frequency lasers, and how this could effect pulse formation.

The dissertation also showed that a distributed equivalent circuit model incorporating a longitudinal resistance to model skin losses, a longitudinal inductance to model the magnetic field of the propagating wave, a series resistance, a parasitic capacitance, and the laser diode active region, consisting of the diode resistance and capacitance, can sufficiently model the propagation properties of the semiconductor laser. For accurate fitting, frequency dependence in the diffusion capacitance needs to be included. This is physically reasonable, as the diffusion capacitance decreases at frequencies above the reciprocal of the carrier lifetime.

Alternate methods do exist for dealing with the problems of microwave propagation. For example, one might decide to feed the device at multiple points along the electrode length rather than with a single probe or a single wire bond. In this formation, the problem of distributed effects could be eliminated altogether; however, when doing this, one would have to be sure that in the transition from 50 ohm transmission line to laser, excess capacitance is not introduced by the bar length long connection.

The low thermal resistance demonstrated for the microstrip laser in this dissertation points towards potential high power operation also. As well as being important on its own, the high power potential is very critical for high frequency, and for this reason, suggests that dealing with distributed effects with a structure

such as the microstrip laser may be a better overall solution than simply bonding continuously along the device length. For example, p-doped lasers show the highest intrinsic bandwidths of all semiconductor lasers, but often the bandwidth cannot be realized because the high thresholds cause heating induced saturation of the output power [4]. The low thermal resistance microstrip laser is advantageous in this regard.

Room temperature measurements show the thermal resistance of the n-ridge microstrip laser to be more than 3 times smaller than a conventional laser of similar dimensions, and simulations indicate that output powers up to xx% greater can be achieved because of this.

Actual realization of high bandwidth and high power was not achieved in this work, despite the fact that different devices showed properties suggesting this to be possible in the microstrip laser. The effects of current spreading in n-ridge lasers caused the excellent thermal resistance lasers to have very high thresholds and low efficiency, precluding high power and high speed operation. However, the excellent thermal resistance was confirmed by the fact that the lasers operated cw at currents above 400 mA, with no special mounting technique employed. Even at elevated temperatures, cw operation was still achieved even when the threshold was nearly 300 mA. The problem of current spreading in n-ridge lasers was analyzed in depth, and it was determined that one good solution to this was to etch through the active region. Experimentally this was verified, as the narrow ridge laser thresholds were reduced from over 90 mA to below 30 mA. However, this set of devices was plagued by high electrical resistance, which prevented both high speed and high

power operation. CW operation was also problematic, with the devices typically shorting out very shortly after the initiation of cw current above threshold.

The high resistance problem in the low threshold devices was most likely processing or material related, and is not intrinsic to the active region etch. While the active region etch may increase the resistance somewhat, it is only several thousand angstroms deep and should not increase it to the extent that was measured - resistances for the etched devices were 10 ohms or higher, whereas the unetched active region devices showed resistances on the order of 1 ohm.

Aside from the resistance issue in that set of devices, the primary obstacle to high frequency and high power operation in the microstrip laser appears to have been problems with leakage currents. Further annealing of the high resistance devices was done, but while the resistances dropped, the thresholds went up and it was not possible to get a good low resistance, low threshold microstrip laser at once. The shorting of the devices under cw operation, discussed above, is also likely related to opening of leakage paths. Microstrip broad area laser thresholds increased with use more than did conventional broad area laser thresholds.

While the leakage current problem was catastrophic in the devices with etched SCH and active regions, it was not catastrophic in the devices in which the ridge was not etched through the active region. Lifetime is often a greater problem in etched active region devices, but there are many reports of devices like this that have lifetimes long enough to show their ultimate capability [5, 6]. Work still needs to be done on the leakage current problem, but it is likely that a good low threshold, low resistance, cw operational microstrip laser could be made. From this, the ultimate high power and high speed capability could be demonstrated.

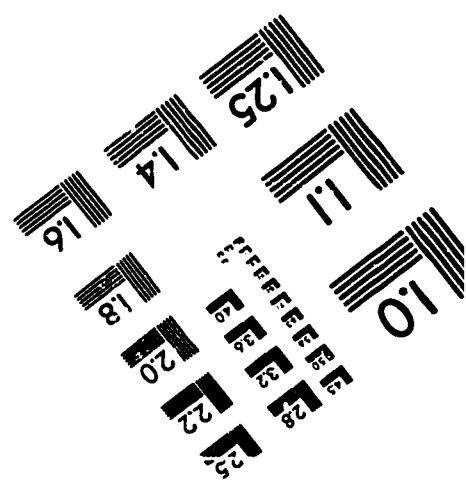
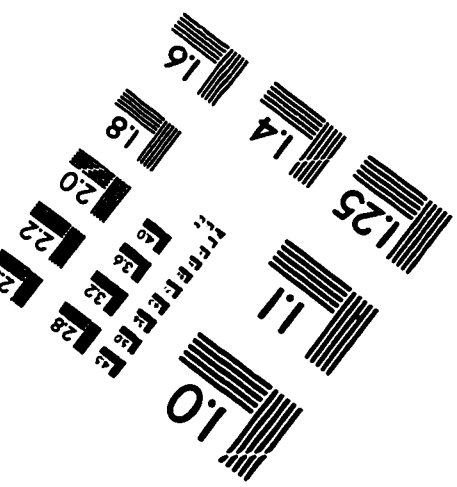
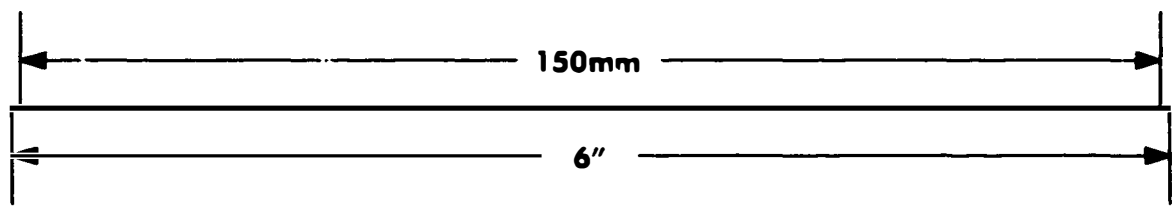
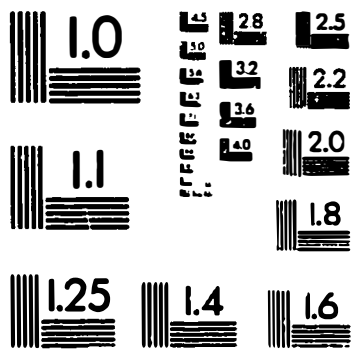
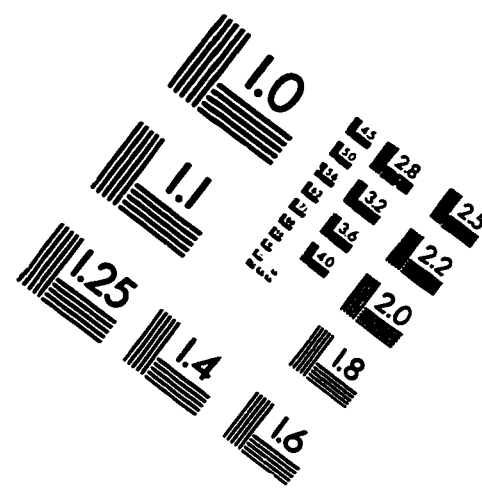
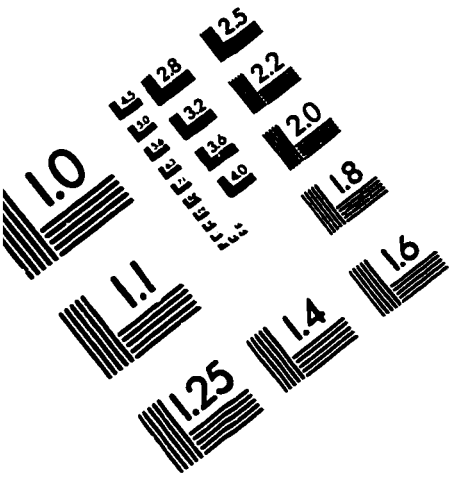
As a recap, this dissertation, and the general development of the microstrip laser, encompasses several different issues related to the physics of semiconductor lasers, in both the DC and AC domain. Effects due to the DC and AC conductivity and diffusivity of semiconductor material leads to a variety of effects, for example, the large skin losses in doped substrate devices, or the high electron mobility that leads to current spreading, high thresholds, and low efficiencies in n-ridge devices. Low electrical resistance in a ridge can lead to low thermal resistance and higher power operation. Lossy AC structures lead to low microwave phase velocities and lower the frequencies at which distributed effects become important. The microstrip laser was invented and developed with all these physical ideas in mind, and with the aim of meeting the technological challenges posed with the purpose developing a higher performance device. The issues addressed by the microstrip laser are fundamental. Therefore, the microstrip laser, and this dissertation, may also be viewed as a very good way of understanding what factors, apart from the active region design, are important in making an excellent semiconductor laser.

## References

- [1] D. M. Cutrer, J. B. Georges, T. C. Wu, B. Wu, and K. Y. Lau, "Resonant modulation of *single* contact monolithic semiconductor lasers at millimeter wave frequencies," *Appl. Phys. Lett.*, vol. 66, pp. 2153-2155, 1995.
- [2] K. C. Sum and N. J. Gomes, "Harmonic generation limitations in gain-switched semiconductor lasers due to distributed microwave effects," *Applied Physics Letters*, vol. 71, pp. 1154-5, 1997.
- [3] D. Jäger, R. Kremer, and A. Stohr, "Travelling-wave optoelectronic devices for microwave applications," presented at *IEEE Int. Microwave Symposium*, Orlando, Fl., 1995.

- [4] S. Weisser, E. C. Larkins, K. Czotscher, W. Benz, J. Daleiden, I. Esquivias, J. Fleissner, J. D. Ralston, B. Romero, R. E. Sah, A. Schönfelder, and J. Rosensweig, "Damping - limited modulation bandwidths up to 40 GHz in undoped short - cavity  $\text{In}_{0.35}\text{Ga}_{0.65}\text{As}$  - GaAs multiple quantum well lasers," *IEEE Photon. Tech. Lett.*, vol. 8, pp. 608-610, 1996.
- [5] H. Wada, Y. Ogawa, and T. Kamijoh, "Novel current-blocking structures in semiconductor lasers using directly bonded  $\text{InP-SiO}_2\text{-InP}$ ," *IEEE Photonics Technology Letters*, vol. 6, pp. 1403-5, 1994.
- [6] J. D. Ralston, S. Weisser, I. Esquivias, E. C. Larkins, J. Rosenzweig, P. J. Tasker, and J. Fleissner, "Control of differential gain, nonlinear gain and damping factor for high-speed application of GaAs-based MQW lasers," *IEEE J. Quantum Electron.*, vol. 29, pp. 1648-1658, 1993.

# IMAGE EVALUATION TEST TARGET (QA-3)



**APPLIED IMAGE, Inc**  
 1653 East Main Street  
 Rochester, NY 14609 USA  
 Phone: 716/482-0300  
 Fax: 716/288-5989

© 1993, Applied Image, Inc., All Rights Reserved